

Institut für Ionenstrahlphysik und Materialforschung  
Helmholtz-Zentrum Dresden-Rossendorf

# Microwave-assisted spectroscopy of spin defect centers in silicon carbide

Zur Erlangung des akademischen Grades  
Doctor rerum naturalium (Dr. rer. nat.)

Vorgelegt der Fakultät Mathematik und Naturwissenschaften  
der Technischen Universität Dresden

DISSERTATION

von

Zhen Shang

geboren am 02. 07. 1990 in China

Eingereicht am 21.07.2021

Verteidigt am 30.09.202, Dresden

Gutachter:

1. Prof. Dr. Manfred Helm (TU-Dresden and HZDR)
2. Prof. Dr. Vladimir Dyakonov (University of Würzburg)

# Abstract

Silicon vacancy ( $V_{Si}$ ) and divacancy ( $VV$ ) centers in silicon carbide (SiC) are promising candidates for quantum applications because of their unique optical and spin properties as well as their stability in extreme environments. These spin defect centers exhibit optically addressable spin states on a single defect level with long quantum coherence times along with infrared light emission, which allows for minimizing scattering losses. These defect centers benefit from existing technology for the production of commercial semiconductor devices based on SiC. Despite various significant works, there are still open questions about their basic properties including the unknown local vibration structure of spin centers and the polarization of the emitted infrared photons. The spectrally overlapped contributions from different defects in the photoluminescence (PL) spectra make the investigation of a specific defect challenging.

In this thesis, I propose to apply a microwave-assisted spectroscopy to address the aforementioned open questions. First, I explain its working principle and describe the experimental setup. Then, I apply microwave-assisted spectroscopy to investigate the local vibrational structure of Si vacancies and divacancies in 4H- and 6H-SiC. Particularly, I obtain the phonon energy and the Debye-Waller factor of all measured spin defect centers. Next, I use microwave-assisted spectroscopy to study the emission of photons and subsequently obtain the polarization properties of Si vacancies in 6H-SiC. The success of microwave-assisted spectroscopy in the investigation of Si vacancies and divacancies in SiC indicates that this approach is a powerful tool for the characterization of spin defects and can be applied to a large variety of spin centers in other wide-bandgap semiconductors and two-dimensional materials.

# Abstrakt

Silizium-Fehlstellen ( $V_{Si}$ ) und Divakanzen (VV) Zentren in Siliziumkarbid (SiC) sind aufgrund ihrer einzigartigen optischen und Spineigenschaften sowie ihrer Stabilität in extremen Umgebungen vielversprechende Kandidaten für Quantenanwendungen. Diese Spin-Defektzentren weisen optisch adressierbare Spinzustände auf einem einzelnen Defektniveau mit langen Quantenkohärenzzeiten zusammen mit einer Infrarotlichtemission auf, was eine Minimierung von Streuverlusten ermöglicht. Diese Defektzentren profitieren von der bestehenden Technologie zur Herstellung kommerzieller Halbleiterbauelemente auf Basis von SiC. Trotz verschiedener bedeutender Arbeiten sind noch Fragen zu ihren grundlegenden Eigenschaften offen, darunter die unbekannte lokale Schwingungsstruktur von Spinzentren und die Polarisation der emittierten Infrarotphotonen. Die spektral überlagerten Beiträge verschiedener Defekte in den Photolumineszenz(PL)-Spektren erschweren die Untersuchung eines bestimmten Defekts.

In dieser Arbeit schlage ich es vor, eine Mikrowellen-unterstützte Spektroskopie anzuwenden, um die oben genannten offenen Fragen zu klären. Zunächst erkläre ich das Funktionsprinzip und beschreibe den Versuchsaufbau. Dann wende ich Mikrowellen-unterstützte Spektroskopie an, um die lokale Schwingungsstruktur von Si-Leerstellen und -Doppelstellen in 4H- und 6H-SiC zu untersuchen. Insbesondere erhalte ich die Phononenenergie und den Debye-Waller-Faktor aller gemessenen Spin-Defektzentren. Als nächstes verwende ich Mikrowellen-unterstützte Spektroskopie, um die Emission von Photonen zu untersuchen und anschließend die Polarisationseigenschaften von Si-Leerstellen in 6H-SiC zu erhalten. Der Erfolg der Mikrowellen-unterstützten Spektroskopie bei der Untersuchung von Silizium-Fehlstellen und Divakanzen in SiC zeigt, dass dieser Ansatz ein leistungsfähiges Werkzeug zur Charakterisierung von Spindefekten ist und auf eine Vielzahl von Spinzentren in anderen Halbleitern mit großer Bandlücke sowie in zwei-dimensionalen Materialien angewandt werden kann.

# Contents

Abstract.....	1
Chapter 1 Introduction .....	4
1.1 Motivation .....	4
1.2 Thesis outline .....	7
1.3 Silicon carbide.....	8
1.4 Spin defect centers in silicon carbide.....	15
1.5 Defect fabrication .....	21
1.6 Local vibrational structure of spin defects in SiC .....	26
Chapter 2 Microwave-assisted spectroscopy .....	30
2.1 Fundamentals of MW-assisted spectroscopy .....	31
2.2 Home-built setup .....	36
Chapter 3 Local vibrational modes of Si vacancy spin qubits in 4H-SiC.....	46
3.1 Introduction .....	47
3.2 Experiment.....	48
3.3 Theory .....	53
3.4 Discussion and conclusions .....	58
Chapter 4 Microwave-assisted spectroscopy of vacancy-related spin centers in hexagonal SiC .	60
4.1 Introduction .....	61
4.2 Experiment.....	63
4.3 Experimental results .....	66
4.4 Conclusion.....	72
Chapter 5 Characterization of the polarization properties of $V_{Si}$ in 6H-SiC by PL and MW- assisted spectroscopy.....	73
5.1 Introduction .....	74
5.2 Experiment.....	75
5.3 Experimental results .....	78
5.4 Conclusion.....	81
Chapter 6 Summary and outlook.....	82
Summary .....	82
Outlook.....	82
Bibliography .....	84
Acknowledgements .....	97
Publication list .....	98
Curriculum Vitae .....	99

# Chapter 1 Introduction

## 1.1 Motivation

Recently, two novel works about quantum computers have been published and attracted global interest. The first one reports the use of a 53-qubit processor (named Sycamore) to solve a task in 200 seconds, while for a classical computer it would take  $10^4$  years [1]. About one year later, another group has reported on the use of indistinguishable photons to implement Gaussian boson sampling, which is  $\sim 10^{14}$  times faster than classical supercomputers [2]. These two works are considered as a demonstration of the so-called quantum supremacy or quantum computational advantage showing the potential of quantum technology as well as its magnificent future. Since Richard Feynman proposed the idea of using a quantum computer to solve the many-body quantum problems in the 1980s [3], the progress to realize a universal quantum computer has never been slowed down. As some decades passed, the mission of realization of quantum computer has been divided into two more specific tasks, a universal quantum algorithm [4] and a realistic physical system to run quantum algorithms. Requirements for both tasks focus on finding the feasible quantum bits (qubits) [5-10]. In recent years, a number of competitive candidate of qubits has been uncovered such as photons [2,6], superconducting circuit [1,9], natural atoms [7,8], or artificial atoms like quantum dots [10], spin defect centers [11-13], etc. Among these candidates, artificial atoms show more advantages in the fabrication, device design and integration, and have further possibility to achieve long-distance quantum communication interfaced with photons [14].

Since the first demonstration of the single spin control associated with the nitrogen vacancy (NV) center in diamond [15], spin defects in solids (such as silicon, silicon carbide and diamond) unveil their power in quantum applications [11-17]. The NV centers provide the fundament condition for functioning as spin qubits. Their states can be polarized or initialized by laser pumping, manipulated by microwave absorption, and read out from luminescence [11]. Despite these promising properties, the NV center in diamond is not yet a perfect candidate for quantum technologies. The first drawback

comes from its host material, the diamond. Diamond is not a material that can be produced on an industrial scale. The material fabrication and machining process is relatively difficult, especially at the nanoscale. Besides that, the light emission from the NV centers is in the visible range [15] (not the standard telecom window), which means that it is not compatible with the existing telecommunication infrastructure. Therefore, the search for ideal spin qubits in a more industrially compatible material remains attractive.

There is a list of certain criteria, which spin qubits must possess [18,19]:

- Spin centers must be highly localized to make a robust qubit and isolated from the decoherence source.
- Spin coherent lifetime must be long enough for quantum operations.
- Energy levels of spin centers must be internally excited to initialize the ground state.
- Energy levels of spin centers must be separated far enough from each other to avoid thermal coupling, which could destroy spin information.
- The host material must have a bandgap wide enough to avoid the energy transition between the valence and the conduction band of the host and the energy levels of spin centers.
- The host material must have weak spin-orbit coupling to avoid unwanted spin flips.
- The host material must be of high crystalline quality with negligible contribution from other optically active defect centers to allow for the isolation and measurement of a particular single defect.
- In addition, measurement techniques must be available to distinguish between the individual sublevels that make up the qubit states.

Besides these criteria, it is also expected that the light emission occurs in the infrared spectral range and the host material is commercially available.

Most recently, a variety of point defects in silicon carbide (SiC) [17,20-22], such as silicon vacancies and divacancies, were exposed to the public as the new generation of spin qubits, which satisfy all criteria above and exhibit optically addressable spin states

on the single defect level with long quantum coherence times. Besides, they also possess other advantages. For example, the light emission from the VV and  $V_{Si}$  centers occurs in the infrared range, which reduces the scattering losses along with its compatibility with the existing fiber-optic telecommunication infrastructure.

Among these defects,  $V_{Si}$  and VV in 4H- and 6H-SiC are the most attractive because of their specific optical and spin properties [23,24]. In spite of many significant works published, there are still open questions for these spin defect centers in SiC, even in the very basic properties of the PL and the local vibrational structure. The spectrally overlapped contribution from different spin centers in defect ensembles prevents the experimental study of each specific defect by PL measurements. Consequently, the investigation of the defect local vibrational structure, or polarization properties of a specific defect becomes difficult. Therefore, a reliable optical tool, which can spectrally isolate a specific spin defect species from defect ensembles, is required.

In this thesis, I propose a new approach, the microwave-assisted spectroscopy, which ingeniously combines the optical and spin properties of spin defects, to spectrally isolate a specific defect species with defect ensembles. With this new technique, I successfully separate the PL spectra of  $V_{Si}$  and VV defects in 4H- and 6H-SiC, and then investigate their local vibrational modes and polarization properties for the first time. I believe that these results will have a considerable interest for the experimental investigation of defect-related spin-vibrational properties, while the developed technique should become an important tool to study a large variety of defects in wide-band-gap semiconducting bulk and two-dimensional materials.



## 1.2 Thesis outline

In Chapter 1, the physical background of the spin defect centers in 4H- and 6H-SiC will be introduced, including the general properties of the host material SiC, the optical and spin properties of the spin centers in SiC, the fabrication of these spin centers as well as the properties of the local vibrational structure. At the end of this chapter, I will point out a severe shortcoming of the previous PL measurement. In chapter 2, I will introduce the microwave-assisted spectroscopy technique to solve the problems with the PL measurements of spin ensembles. Meanwhile, I will describe our home-built setup. In chapters 3, the method is applied for one particular type of defects ( $V_{Si}$ ) and compared with theory. In chapter 4, the method is applied to a large variety of defects ( $V_{Si}$  and  $VV$ ) in two polytypes. In chapter 5, polarization properties of emitted photons will be discussed in detail. The final chapter will be the summary and outlook of my research on spin centers.

## 1.3 Silicon carbide

In this chapter, a brief introduction of SiC, including its basic properties, polytypism and growth technology will be provided. Further information of SiC can be found in ref. [25].

### 1.3.1 Basic properties

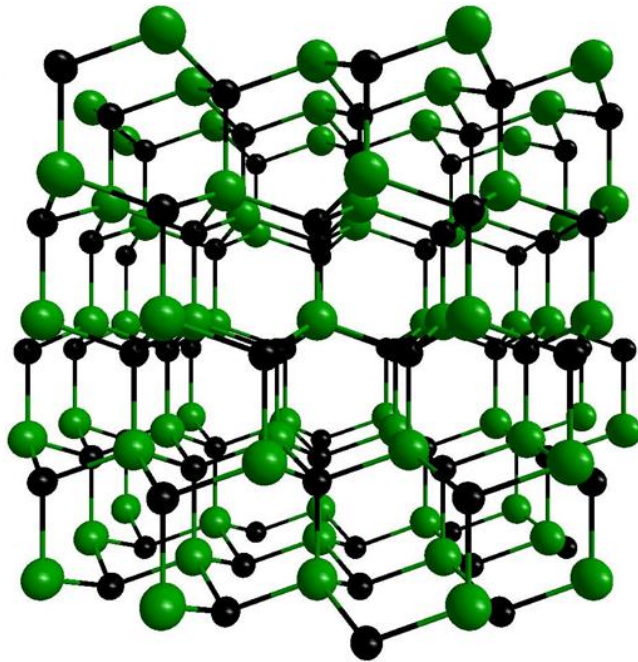


Figure 1.3.1 Crystalline structure of 4H-SiC. The green balls present silicon atoms and the black balls present carbon atoms.

SiC is an indirect wide bandgap semiconductor, a compound of silicon and carbon atoms by the highly covalent chemical bonding ( $sp^3$ ) with a short bond length of 1.89 Å [25]. Every Si atom is surrounded by four C atoms and vice versa, as shown in Fig.1.3.1. Its special structure gives itself many unique properties [25-27], including high stability at high temperature, high power and high radiation environment, high hardness, excellent oxidation resistance, good thermal conductivity, good light transmittance, and high thermal shock resistance. Part of its properties is shown in table 1.3.1 comparing with silicon and diamond. Plenty of advantages make SiC popular in the traditional industry. Therefore, it has extensive applications in the industry since it was first discovered in 1824 by Berzelius [28]. In the earlier years, SiC was utilized as an abrasive material because of its excellent hardness. Later on in the semiconductor era, due to its wide

bandgap, SiC was widely used in semiconductor devices [25] such as metal-oxide-field-effect transistors [29], power electronics [29] and light-emitting devices [30]. More recently, SiC as a host material for single photon sources and spin qubits is widely used in many quantum technologies, which will be discussed later.

	Si	SiC	Diamond
<b>Bandgap (eV)</b>	1.1	2.3-3.2*	5.5
<b>Density (g/cm<sup>3</sup>)</b>	2.33	3.17-3.21	3.53
<b>Hardness (Mohs)</b>	6.5	9.5	10
<b>Thermal conductivity (Wcm<sup>-1</sup>K<sup>-1</sup>)</b>	1.1	3.6-4.9	10-25
<b>Refractive index</b>	3.5	2.5-2.7	2.4
<b>Breakdown field (10<sup>5</sup>V<sup>-1</sup>)</b>	3	40-60	

Table 1.3.1. Basic material properties of Si, SiC and Diamond at room temperature. Values can be found in ref. [25,31]. \*Depending on the polytype.

### 1.3.2 Polytypism

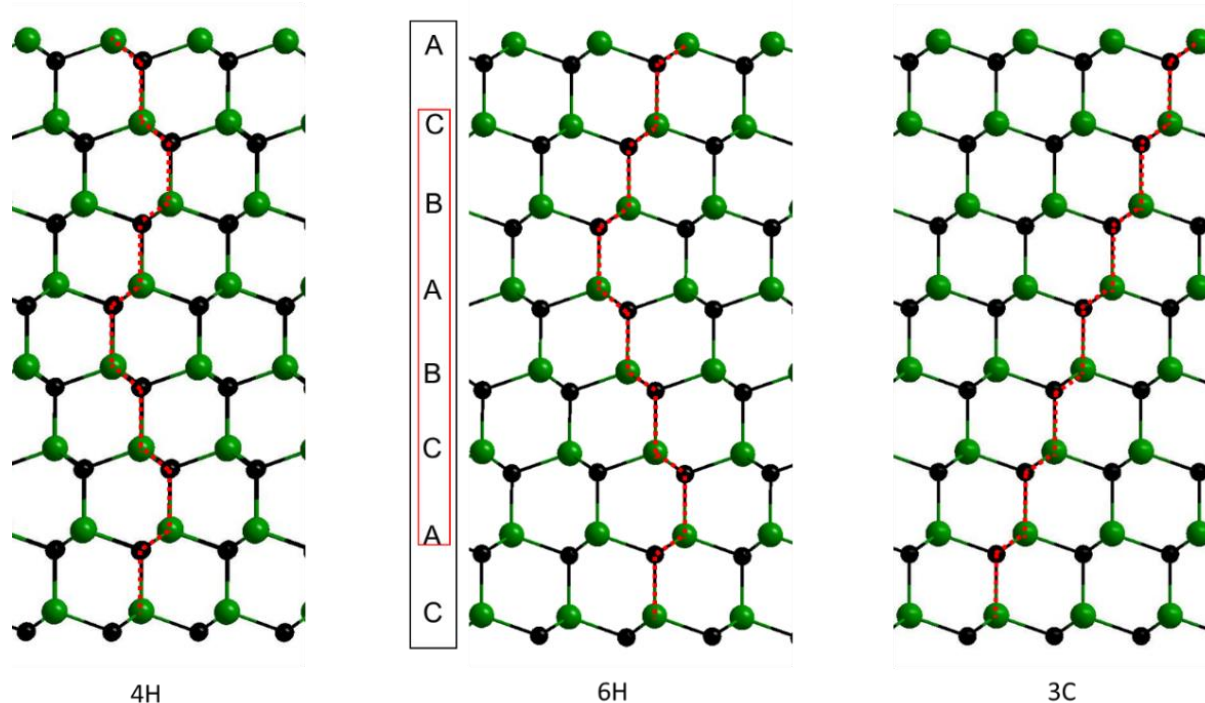


Figure 1. 3. 2 Crystal structure diagram of 4H, 6H and 3C polytypes of SiC.

The best-known property of SiC is the polytypism [25]. Bulk SiC is formed by stacking Si-C bilayers. Due to the different stacking sequences along the C-axis, more than 200

polytypes are reported until now. The most frequently polytypes are 6H, 4H, 3C and 15R. The numbers (4, 6, 3, and 15) in front of the capital letters represent the number of Si-C bilayers in a repeating cycle. The H, C and R mean that polytype has a hexagonal, cubic, or rhombohedral structure, respectively. Fig. 1.3.2 presents the crystal structure of 4H, 6H and 3C polytypes.

Here the 6H is used as an example to explain the polytypism. In the structure of the 6H polytype, there are 3 different Si-C bilayers, named A, B and C corresponding to h, k1 and k2 crystal sites. As shown in Fig. 1.3.2, it is clear that the 6H-SiC is the repeating sequence of ACBABC, six bilayers along the C-axis. As for 3C and 4H, the sequence is ABC and ABCB. Usually, the 3C-SiC is named  $\beta$ -SiC which is the substitutional structure of diamond; all other polytypes are named as  $\alpha$ -SiC. The table below gives some basic physical parameters of three SiC polytypes. It shows that some basic physical parameters are similar for these three different polytypes.

<b>Polytype</b>	<b>Density (g/cm<sup>3</sup>)</b>	<b>Bandgap (eV)</b>	<b>Melting point (K)</b>	<b>Lattice parameter (nm)</b>
<b>4H</b>	3.215	3.263	~3103K	a=0.308, c=1.008
<b>6H</b>	3.215	3.023	~3103K	a=0.308, c=1.512
<b>3C</b>	3.215	2.390	~3103K	a=0.435

Table 1.3.2. Some basic physical parameters of the three polytypes of SiC. Values are taken from ref. [25].

To identify the polytype of a SiC crystal, Raman scattering method [32] can be used. The Raman spectra of 4H-and 6H-SiC are shown in Fig.1.3.3, indicating obvious differences between 4H and 6H polytypes.

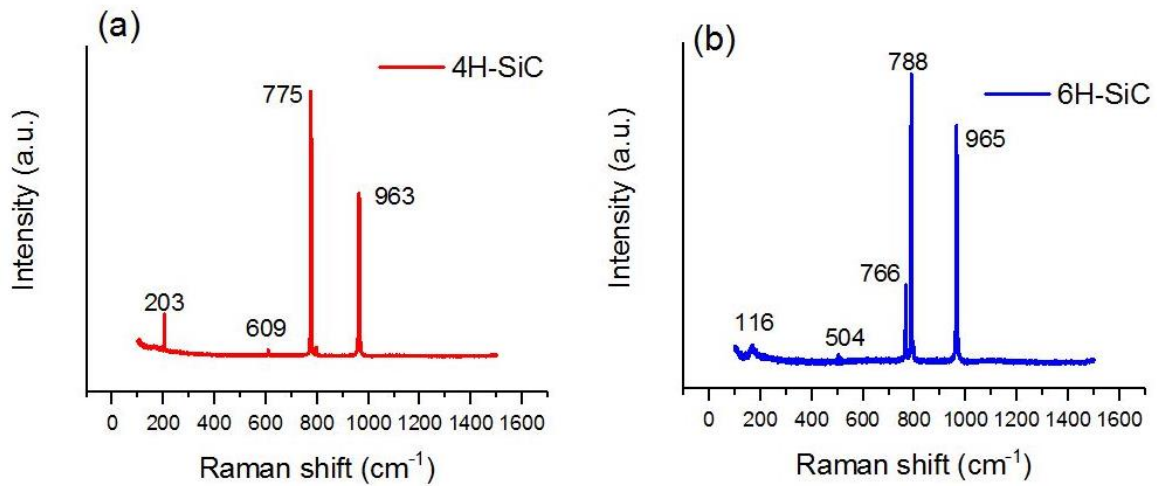


Figure 1.3.3 Raman spectra of 4H- and 6H-SiC, respectively.

### 1.3.3 SiC growth.

In this part, a brief introduction of growth technologies of bulk SiC including the growth methods, the control of polytypes and the defects produced during the growth will be given. The discussion of defects is limited to a brief introduction of defect species. Further details of the intrinsic defects will be discussed in the next section.

#### Growth technologies

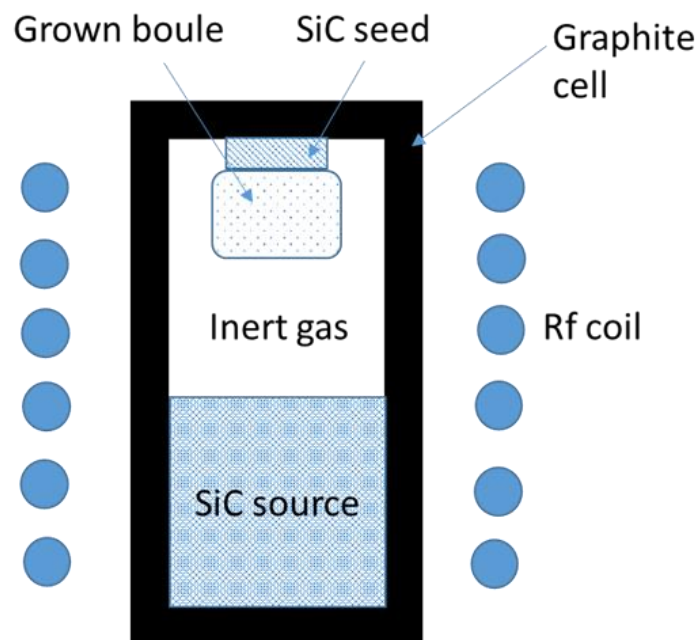


Figure 1.3.4 Growth chamber for physical vapor transport [33].

The natural SiC is found in extraterrestrial rocks known as carborundum. However, it is very rare and not suitable for industry. The first artificial synthesis work for SiC date back to 1892. In this year, Acheson successfully fabricated crystalline SiC from a reaction of carbon and silicon dioxide [34]. The requirement for large pure SiC bulk or wafer in the modern industry promotes the development of bulk SiC growth technologies. At present, the alternative bulk SiC growth techniques include physical vapor transport (PVT, also called seeded sublimation) [35], high-temperature chemical vapor deposition (HTCVD) [33], and solution growth [36].

The most mature technique for growing bulk SiC is the PVT [25,35,37]. Fig.1.3.4 schematically illustrates the setup of PVT employed in the growth of SiC. SiC powder or sintered polycrystalline SiC is placed at the bottom of a graphite cell as the source providing Si and C atoms. A SiC crystal is placed inside the top of the graphite cell as the seed in the SiC growth. The graphite cell is full of high purity inert gas, Ar or He. The cell is heated by radio frequency. At the bottom of the cell, the temperature is increased up to 2400 °C. At this temperature, the SiC powder sublimates into the gas species Si, Si<sub>2</sub>C and SiC<sub>2</sub>. At the seed area, the temperature is a little lower than the SiC source temperature, which induces the sublimed SiC species to recrystallize on the seed. Bulk growth occurs during this process. The philosophy of HTCVD and solution growth is similar to PVT. The difference is that for HTCVD, the SiC source is not SiC powder anymore but gases such as SiH<sub>4</sub> and C<sub>2</sub>H<sub>4</sub>. For the solution growth, the Si atoms come from the Si melt, while the C atoms come from the surrounded graphite wall.

### **Polytype control in growth**

The polytype control during the SiC growth [25,37] remains a challenge up to date. Due to the different polytypes resulting in a significant difference in electronic and optical properties, the growth of a desired single SiC polytype is mandatory in the crystal growth of SiC. The main factors determining the polytype stability include the C/Si ratio, the polarity of the seed crystal, the impurity incorporation, temperature as well as temperature gradient and inert gas pressure [25]. For example, the growth on seed SiC (0001) face (Si face) more likely gives 6H-SiC. In contrast, 4H-SiC crystal is more likely grown on seed SiC (000 $\bar{1}$ ) face (C face) no matter what the polytype of seed SiC is.

Another example, under C-rich growth ambient, the hexagonal SiC is more stable, especially 4H-SiC.

### **Defects in bulk SiC**

Another challenge in the growth is the defects. Defects in crystalline solids are interruptions of regular patterns and breaks of the translational symmetry. Although many works have been carried out to prevent the generation of defects, this problem remains unsolved until now. Dividing by dimensionality, there are four types of defects [25,37]:

- Zero dimensional defects or point defects
- One dimensional defects or line defects
- Two dimensional defects or planar defects
- Three dimensional defects or volume defects

**Point defects** include intrinsic point defects and extrinsic point defects, which depends on if the defect is related to foreign atoms or not. If a defect is caused by the presence of a foreign atom, it is named the extrinsic defect. For example, if a silicon atom in SiC is replaced by a vanadium, it forms a vanadium point defect [38]. If a defect comes from the rearrangement of the original atoms, it is named as intrinsic defects such as vacancies, antisites, self-interstitials, Frenkel pairs or defect complexes. Although most classes of point defects reduce the crystal quality, there are some special point defects bringing many novel properties to SiC. For example, nitrogen atoms – which are actually shallow impurities – turn the pristine SiC into an n-type semiconductor, which is widely used in the industry. As for vacancies, they are considered as excellent quantum technology platforms, today. Vacancies in SiC are the main topic of my thesis. The generation, properties, and applications of vacancies in SiC will be discussed in detail in the following chapters.

**Line defects** refer to dislocations in SiC crystals, such as threading edge dislocations and threading screw dislocation, which are the major reason for degradation and failure of electronic devices. They are usually generated from thermoelastic stress during the growing and cooling process. The growth rate in relation to the growth temperature may also cause dislocations during the SiC growth.

**Planar defects** are stacking faults during the crystal growth. For example, the 6H-SiC has a sequence ACBABC. If a stacking fault happens in 6H-SiC, the sequence may become ACBBBC. Various sources have been reported for the generation of stacking faults during growth [37], such as a high nitrogen doping level, overgrowth from threading screw dislocations in CVD or c-axis threading dislocations in the PVT growth. Recent papers reported that some unknown vacancies in 4H- and 6H-SiC are coming from stacking faults [39], which makes these defects more difficult to distinguish or investigate.

**The volume defects** can be SiC polytype switches, silicon or carbon inclusions as well as voids. Technologically, polytypes switches may come from unstable or wrong growth conditions, for example, the wrong gas phase composition. The temperature or temperature gradient, the type of doping, the seed polarity all play a role in the occurrence of polytype changes. Carbon inclusions are reported that they are basically from carbon particles in the SiC source or crucible material transporting to the growth interface by an upstream flow. However, the origin of silicon droplets is a low C/Si ratio in gas phase. As for voids, improper seed mounting is a major reason.



## 1.4 Spin defect centers in silicon carbide

The intrinsic point defects in SiC, such as  $V_{Si}$  [17],  $VV$  [20], antivacancies ( $V_C C_{Si}$ ) [22], and NV centers [21] are well known color centers or spin centers. In this section, a comprehensive introduction about the  $V_{Si}$  and  $VV$  in 4H- and 6H-SiC will be provided.

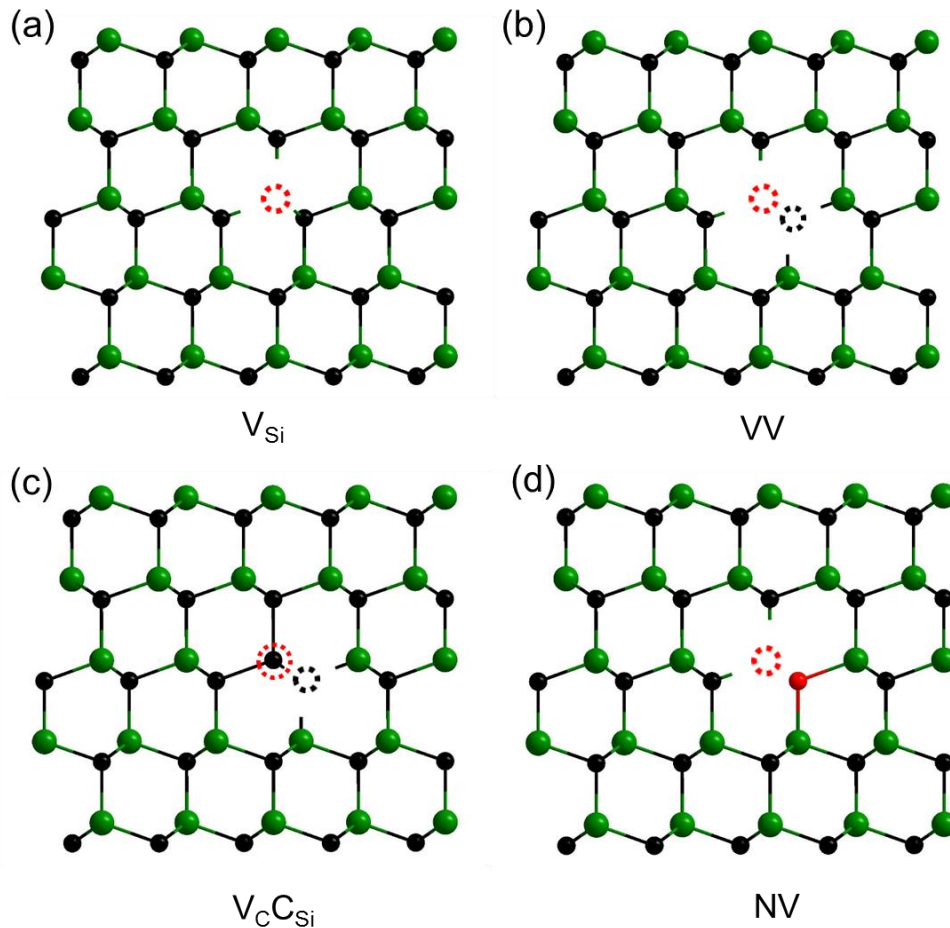


Figure 1.4.1 (a), (b), (c) and (d) schematic diagrams for  $V_{Si}$ ,  $VV$ ,  $V_C C_{Si}$ , and  $NV$  centers in 4H SiC, respectively. The green balls present silicon atoms and the black balls present carbon atoms.

Point defects break the translation symmetry of its host material and induce deep levels in the energy gap. The deep energy levels give point defects the property to absorb light at a particular wavelength leading to a specific color to the host material. Therefore, they are named as color centers [12]. The second important property of these point defects is that they possess multiple spin states in the ground and excited states, which give them the potential to function as spin qubits [17-21].

### Silicon vacancies

One of the most promising point defects in SiC for quantum applications is the negatively charged  $V_{Si}$ . As the name implies, it is one missing silicon atom from its lattice site as shown in Fig. 1.4.1 (a). The host material SiC provides  $V_{Si}$  a stable molecular environment and advantages in nanofabrication and integration with existing electronic and quantum devices. The main reason for attracting global interest is its outstanding optical and spin properties [23,40,41], such as high-spectral stability and long spin coherence time.

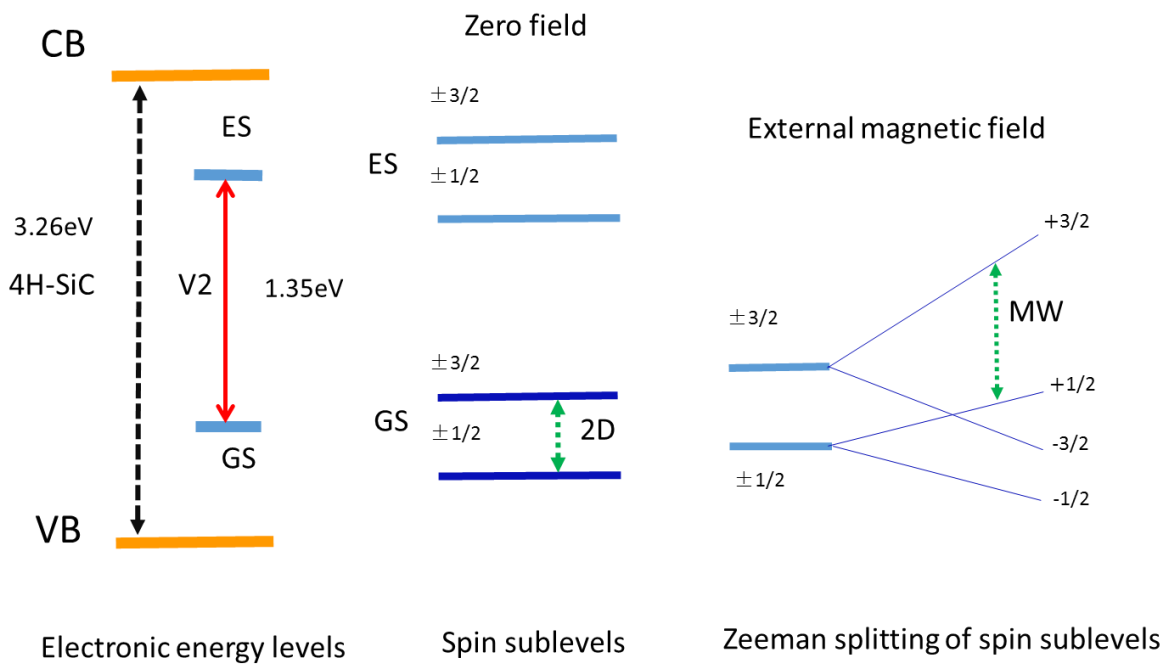


Figure 1.4.2 schematic energy level diagram of V2 (the vacancy at h inequivalent lattice site in 4, see the next page for an explanation) in 4H-SiC and the spin sublevels without and with an external magnetic field.

Dangling electrons around vacancies form an isolated in-bandgap electronic energy level structure, which can be optically excited and subsequently emit infrared or near infrared (NIR) photons [40]. For example, for V2 in SiC (see next page for a definition), the energy separation between the ground state and the excited state is 1.35 eV [42], which is much smaller than the bandgap (3.26 eV) of 4H-SiC. This means that the energetic transition between the valence and the conduction band of the host takes no place. Besides, comparing with the red light emitted from the NV center in diamond (637nm [15]), the infrared light from  $V_{Si}$  has lower scattering losses in optical fibers. Single  $V_{Si}$  defects have been isolated and proved as single photon sources by measuring

the so-called second order correlation function [40]. As a single photon source, the single  $V_{Si}$  defect is a highly attractive candidate for quantum information processing, quantum computing, among others. Moreover, the fact that the NIR light can efficiently penetrate organic tissue also gives the  $V_{Si}$  potential for biological sensing and imaging [43].

The second promising property is that the  $V_{Si}$  exhibits a spin multiplicity of a spin number equal to 3/2. Its spin Hamiltonian has the form [17]:

$$H = D \left( S_Z^2 - \frac{1}{3} \mathbf{S}(\mathbf{S} + 1) \right) + g\mu_B \mathbf{B} \cdot \mathbf{S} \quad 1.4.1$$

Where the first part  $D \left( S_Z^2 - \frac{1}{3} \mathbf{S}(\mathbf{S} + 1) \right)$  is related to the lattice field, the second part  $g\mu_B \mathbf{B} \cdot \mathbf{S}$  is the Zeeman splitting corresponding to the external magnetic field. At zero magnetic field, there is no Zeeman splitting. Thus, the electronic levels possess two spin sublevels:  $M_s = \pm 3/2$  and  $M_s = \pm 1/2$  with an energy gap equal to  $2D$  shown in Fig.1.4.2, which is known as zero-field splitting (ZFS). These two spin sublevels of the ground state can be initialized or polarized by optically pumping and can be manipulated by absorbing resonant microwave, which forms the fundamental of defect spin qubits.

In an external magnetic field, the two spin sublevels split further into four levels ( $+3/2$ ,  $1/2$ ,  $-1/2$ ,  $-3/2$ ) shown in Fig 1.4.2. The resonant microwave frequency of any two spin levels strongly depends on the external magnetic field. Therefore, the  $V_{Si}$  has very promising prospects in magnetic field sensing.

Because there are two different Si-C bilayers in 4H-SiC, there are two types of  $V_{Si}$  in 4H-SiC named V1 and V2 [42,44] corresponding to k and h inequivalent lattice sites, respectively. Due to the different lattice environments, the properties of V1 and V2 are also different. For instance, the energy separation between the ground and the excited states is 1.438 eV for V1 and 1.352 eV for V2. Further details will be discussed in the experimental results in the last three chapters. As for 6H-SiC, there are three kinds of  $V_{Si}$  named V1, V2 and V3 [42,44], corresponding to k1, k2 and h inequivalent lattice sites.

## **Divacancy (VV)**

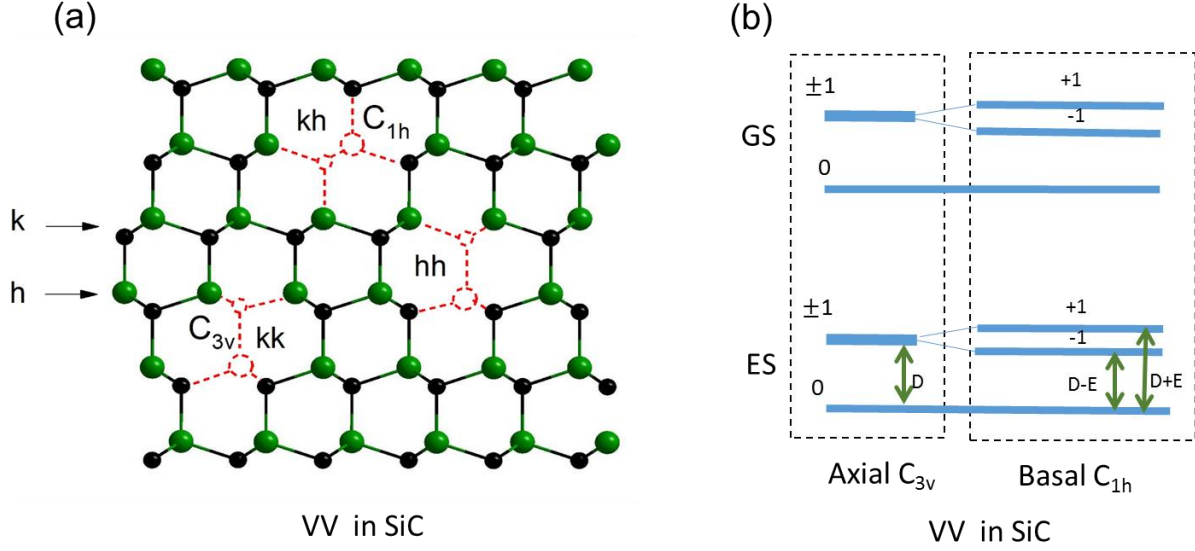


Figure 1.4.3 (a) Schematic diagram and (b) energy structure of spin sublevels of two types of symmetry of VV defects in 4H-SiC. Green balls represent Si atoms and black balls represent C atoms.

The other promising point defect in SiC is the neutrally charged divacancy, which also has been optically isolated on a single defect level recently [45]. The divacancy is a missing silicon atom coupled to a missing carbon atom from their lattice sites, which is shown in Fig1.4.1 (b). Similar to  $V_{Si}$ , the photons emitted from VVs also lie in NIR around 1100 nm and possess the property of behaving as a single photon source [45].

Because of symmetry and integer spin number ( $S = 1$ ), the VV spin properties are different from that of the  $V_{Si}$  centers. The spin Hamiltonian of the VV centers is [45,46]:

$$H = D \left( S_z^2 - \frac{1}{3} S(S+1) \right) + E(S_x^2 - S_y^2) + g\mu_B \mathbf{B} \cdot \mathbf{S} \quad 1.4.2$$

Here,  $D$  and  $E$  are the zero-field splitting parameters. As shown in Fig.1.4.3 (a), there are two different symmetries  $C_{3v}$  and  $C_{1h}$  corresponding to axial and basal defect orientations, respectively. For the higher symmetry  $C_{3v}$ , parameter  $E$  is zero; for the lower symmetry  $C_{1h}$ ,  $E$  is not zero. For axial defects, the zero-field splitting energy equals to  $D$ . For basal defects, the zero-field splitting energy equals to  $D \pm E$ . The spin sublevels of VV in SiC are shown in Fig 1.4.3 (b). Table 1.4.1 illustrates the orientation of observed VV defects in 4H- and 6H-SiC.

<b>polytype</b>	<b>VV</b>	<b>Orientation</b>	<b>Symmetry</b>
<b>4H</b>	PL1	c-axis	$C_{3v}$
	PL2	c-axis	$C_{3v}$
	PL3	basal	$C_{1h}$
	PL4	basal	$C_{1h}$
<b>6H</b>	QL1	c-axis	$C_{3v}$
	QL2	c-axis	$C_{3v}$
	QL3	basal	$C_{1h}$
	QL4	basal	$C_{1h}$
	QL5	basal	$C_{1h}$
	QL6	c-axis	$C_{3v}$

Table 1.4.2 Summary of orientation and symmetry of known VV defects in 4H- and 6H SiC. Data are taken from ref. [47] supplementary.

Because the missing atoms can be in the same Si-C bilayers (kk, hh), or in two different layers (hk), the VV centers reveal larger variety compared to the  $V_{Si}$  centers. Table 1.4.2 presents the identified VVs in 4H-SiC (named PL1 to PL4 [46]) and in 6H-SiC (name QL1 to QL6 [47]) and their orientations and symmetries.

### **The fingerprint of defects: PL spectra**

The photon energy emitted by defects depends on the energy separation between the ground and excited states of the defects. This optical transition is known as the zero-phonon line (ZPL) in the PL spectra, which is the fingerprint of each defect [15-17,20-23]. Figure 1.4.4 (a) gives an example of PL spectra of  $V_{Si}$  and VV defects in 4H-SiC. In Fig. 1.4.4 (a), the PL peaks named V1 and V2 are the  $V_{Si}$  ZPL in 4H-SiC. The PL peaks named PL2, PL3 and PL4 correspond the ZPL of different VV defects in 4H-SiC.

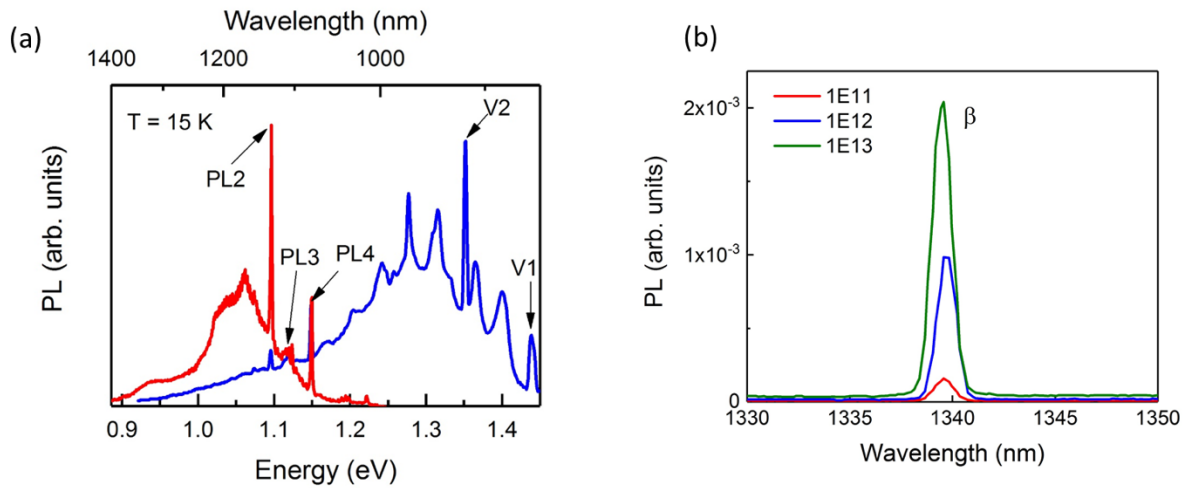


Figure 1.4.4 (a) A typical PL spectrum of  $V_{Si}$  and  $VV$  in 4H-SiC. (b) PL intensity of vanadium defects depending on the ion implantation dose.

Another important information, which can directly read out, is the PL intensity. Many factors influence the PL intensity including excitation laser intensity, laser wavelength, detector sensitivity, and defect density. In Fig. 1.1.4 (a), the red line represents a PL spectrum obtained by exciting the sample with a 940 nm laser, while the blue line stands for a PL spectrum recorded from the same sample upon an 808 nm laser excitation. By comparing these two lines, one can conclude that the 940 nm laser is more efficient for exciting  $VV$  defects in 4H-SiC, especially for PL2. Fig.1.4.4 (b) shows an example of PL intensity of vanadium defects in 4H-SiC as a function of implantation dose. Obviously, the PL intensity increase with increasing implantation dose. It is worth mentioning that PL intensity only gives an approximate concentration of effective defects. To obtain the defect density from the PL measurement is not trivial. This question will be discussed in detail in the next section.

## 1.5 Defect fabrication

Generally, many approaches can be used to create intrinsic defects, such as femtosecond laser writing [48] and thermal quenching [49]. The most common approaches are the passive creation during the growth [25] and the active defects fabrication by energetic particle irradiation/implantation [50-57]. During bulk growth, some defects can be created because of some material imperfections during growth, which is discussed in section 1.3. Although great efforts are devoted to reducing these defects during the bulk growth, it seems that the occurrence of defects is inevitable. Yet the concentration of these defects can be controlled in a low level by careful growth control. The passively created defects evenly distribute along the bulk, but the defect species cannot be controlled. Therefore, these defects are hardly applied in quantum devices. However, these stable, high-concentration and homogeneously distributed defect ensembles are very suitable for the investigation of the optical and spin properties. In my research, the  $V_{Si}$  defects in pristine SiC (bought from Cree) are created during the sample growth. In this section, the focus will be on the fabrication of optically active spin defects via energetic particle irradiation/implantation.

### **Energetic particle irradiation/implantation**

When the energetic particles penetrate a target wafer, they lose their energy and cause target atoms displacements in two ways: elastic collisions and inelastic collision. Elastic collisions refer to interactions between the implanted particles and the nuclei of the target. The inelastic collisions are the interactions with electrons while implanted particles pass through the electron cloud of target atoms. Both collisions are able to result in displacements of atoms from their original site and create vacancies and interstitial atom pairs, the so-called Frenkel pairs, if the kinetic energy of particles is large enough [55].

The reported particles used in  $V_{Si}$  and VV fabrication in SiC include electrons [52], neutrons [56], protons [53], helium ions [57] and carbon ions [57]. Electrons and ions are accelerated to a high energy by an accelerator and neutrons are generated in a nuclear reactor. The type of defect, its concentration and depth in the host material are determined by the type of particle, energy, fluences and subsequent annealing. Usually,

a Monte Carlo simulation software SRIM is used to simulate ion implantation/irradiation process and calculate defect depths and concentrations [58].

### **Particle species, energy and fluence**

Neutron irradiation results in a homogeneous distribution [50] of  $V_{Si}$  and VV defects in the bulk. This approach usually creates high-density defect ensembles, which means it is more suitable for the realization of magnetic field sensors and room-temperature masers [43]. Neutrons are not charged, therefore, they lose energy mainly by elastic collisions and induce considerably crystal damage, which results in a multitude of defect classes other than  $V_{Si}$  or VV and leads to deterioration of the spin coherence properties.

Electrons drop their energy by inelastic collision in interactions with orbital electrons. Hence, it is difficult to reach the defect densities created by ion or neutron irradiation. In addition, the electron irradiation results in a defect density gradient in a thick sample [50], with a high density close to the sample surface, which is different from the homogeneous distribution created by neutron irradiation.

In contrast to electron and neutron irradiation, implantation of ions, such as  $H^+$ ,  $He^+$ ,  $C^+$  and  $Si^{2+}$  ions [57], mostly form a defect layer at a given depth in the sample, the so-called the Bragg peak. Therefore, this approach is more suitable for defect fabrication at desired locations in the crystal. Moreover, ion implantation is a very useful method to fabricate transition metal-related defects, such as titanium defects, vanadium defects, etc.

Usually, the energy of ions determines the depth of defects in SiC. According to SRIM calculations, 1 MeV  $H^+$  ions create a  $V_{Si}$  defects layer at a depth of 10  $\mu m$  in a SiC wafer. Another important parameter is the implantation fluence, which is a crucial factor determining the density of defects. As shown in Fig. 1.5.1 [50], high implantation fluence causes the higher defect density measured by PL. However, the PL intensity decreases at a neutron fluence higher than  $6.7 \times 10^{17} \text{ cm}^{-2}$  (Fig.1.5.1 (a)). The neutron irradiation creates  $V_{Si}$  defects in SiC, in the meanwhile, it also causes a severe crystal damage, which leads to a strong decrease of the PL intensity.



Typically, a low ion fluence is required to engineer single photon emitters or single spin qubits. For instance, to create single  $V_{Si}$  defects by proton irradiation, the fluence is as low as  $10^9 \text{ cm}^{-2}$  [53]. On the contrary, a high implantation fluence is needed to create defect ensembles for a magnetic field sensor or to investigate the optical and spin properties of defects.

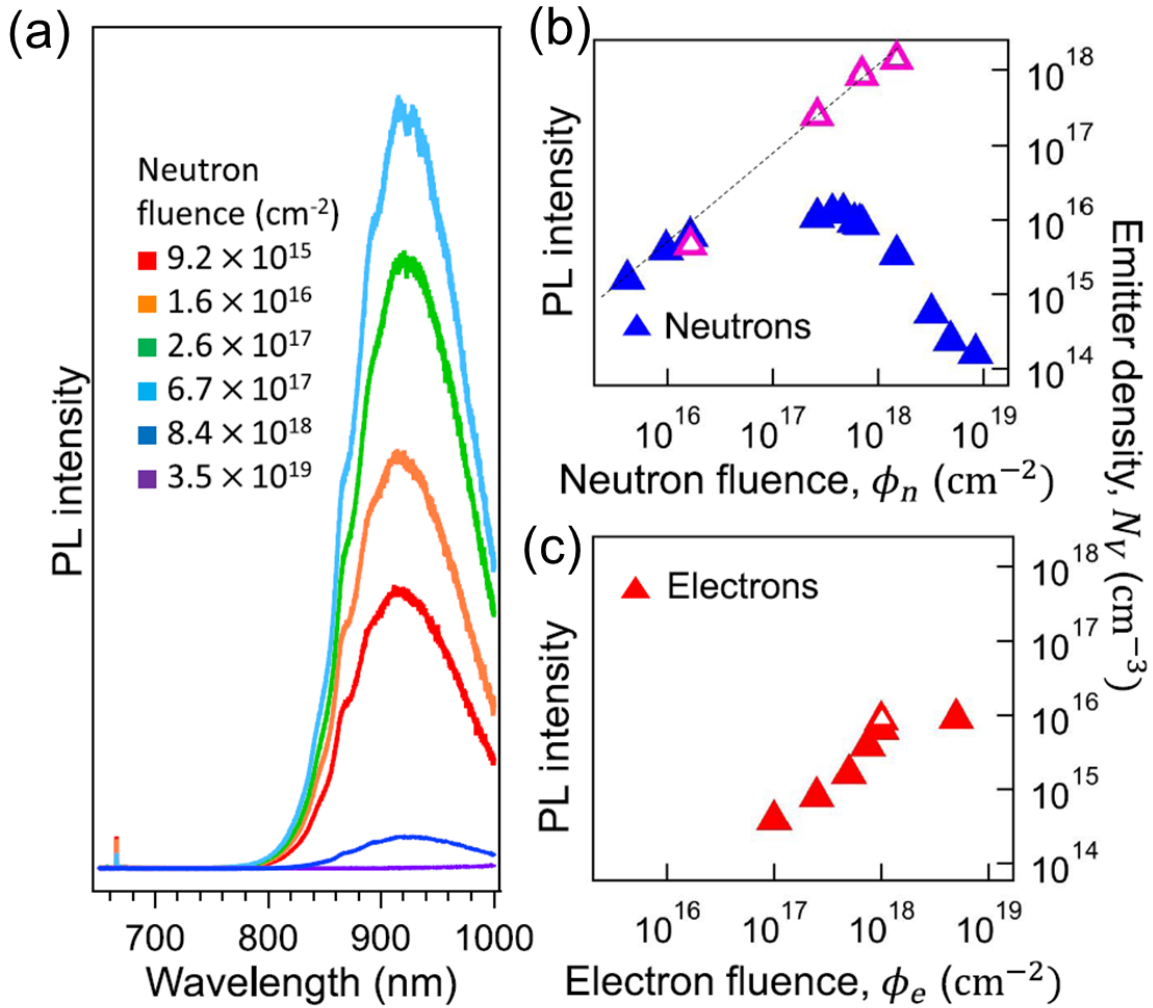


Figure 1.5.1 (a) PL spectra of the  $V_{Si}$  defects for different neutron irradiation fluences. (b) PL intensity as a function of the neutron irradiation fluence. (c) PL intensity as a function of the electron irradiation fluence. Open triangles in (b) and (c) show the  $V_{Si}$  density. The figure is taken from ref. [50].

### The subsequent furnace annealing

A subsequent anneal is widely used to optimize defect fabrication [57,59,60]. Usually, the annealing temperature and annealing time influence the defect densities and

properties. For example, a post-annealing step at 500 °C shows the best results in terms of the emitter density on the production of  $V_{Si}$  as shown in Fig. 1.5.2 (b).

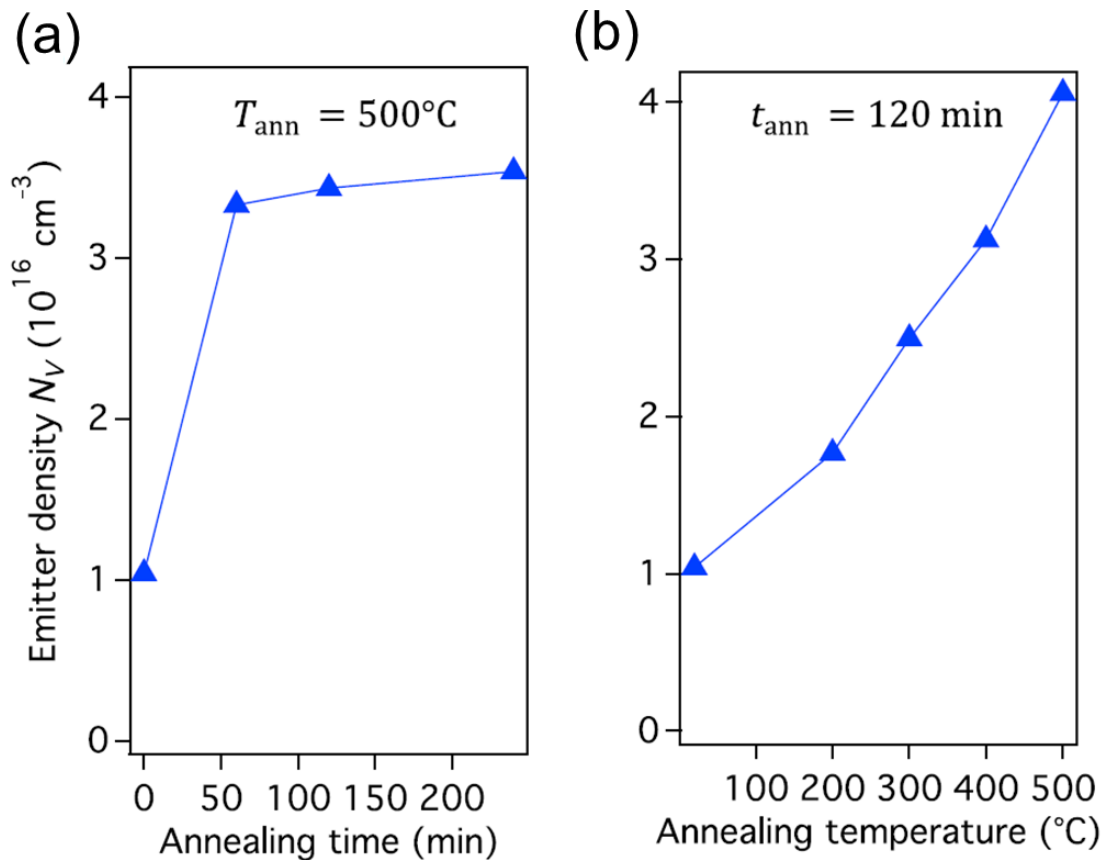


Figure 1.5.2 Emitter density as a function of annealing time (a) and temperature (b). The figure is taken from ref. [50].

Another example is that electron irradiation creates both  $V_{Si}$  and  $VV$  defects and a higher post-annealing temperature (up to 900 °C) can be used to improve the properties of  $VV$  defects [60]. This is because the  $VV$  defect is more stable than  $V_{Si}$  at high temperature.

If the sample is annealed at a temperature higher than 1400 °C, the annealing should be performed under the protection of a carbon cap to prevent sublimation of silicon atoms from the surface of SiC [38]. This carbon cap or protective carbon layer can be fabricated by spin coating a photoresist. For instance, to make vanadium defects optically active upon introducing them by implantation, the recipe includes two steps: First, deposition of the photoresist layer and subsequently an annealing process at three different temperatures as follows:

1. Annealing at 350 °C in Ar atmosphere for 30 min

2. Annealing at 1400 °C in Ar atmosphere for 30 min
3. Annealing at 750 °C in air for 60 min

The annealing at 350 °C is for carbonizing the photoresist to form a carbon cap. The second annealing at 1400 °C is to make the vanadium defects optically active. The third annealing at 750 °C is for removing the carbon cap by reaction with oxygen.

### **Defect fabrication in a desired location**

In some applications, for example quantum networks, defects in a desired location are required. The approaches discussed above apply to broad-beam irradiation, which produces defects randomly distributed in the bulk materials, stacked together and hard to isolate. To create defects in a desired 3D volume at the nanoscale, a PMMA layer with an array of holes of a few-micrometer size is used as a shadow mask for the electron irradiation process [47]. By reducing the diameter of holes and the irradiation fluence, single photon emitter in a desired location can be created. Other techniques such as focused ion beam [51] and direct femtosecond laser writing [48] can also be utilized for the creation of single spin defect centers in a desired location.

## 1.6 Local vibrational structure of spin defects in SiC

### Zero-phonon line and phonon-side bands

In the previous sections was introduced that the  $V_{Si}$  and  $VV$  defects possess localized electronic energy levels in the bandgap of SiC. The optical transition between the high energy level and lower energy level leads to luminescence. As a two-energy-level system, the PL line shape of a defect should emerge as a narrow line located at the wavelength which equals to the energy gap of these two energy levels. However, a typical PL spectrum of a specific defect usually depicts as a narrow peak accompanied by a series of broad peaks as shown in Fig 2.3.1. The narrow peak is known ZPL and the accompanying peaks are phonon side bands (PSBs).

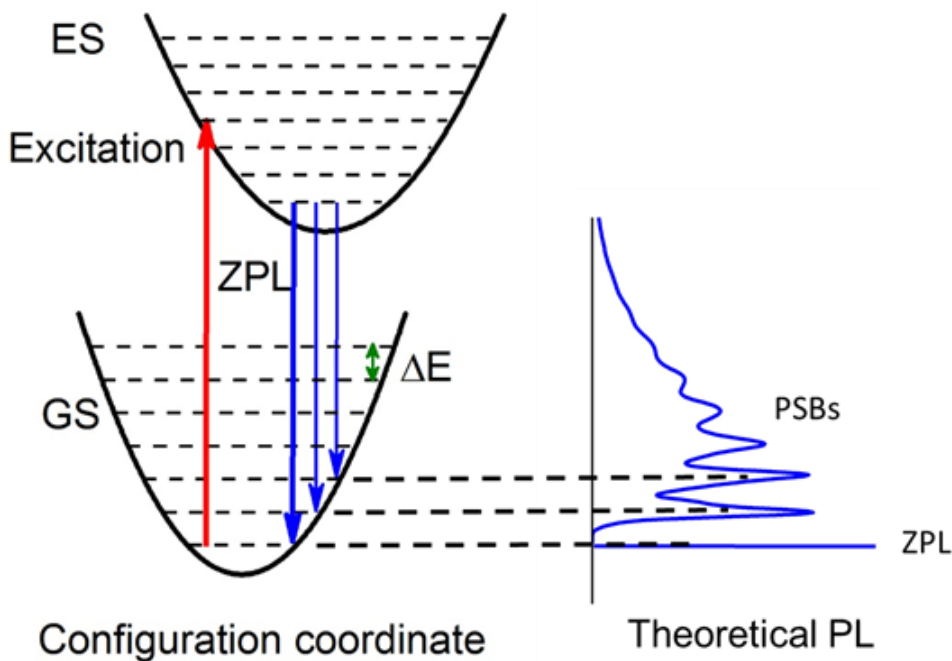


Figure 1.6.1 Diagram of vibrational energy levels of a defect and its theoretical PL line shape of zero phonon line (ZPL) and the accompanying peaks are phonon side bands (PSBs).

The spin defects can be considered as artificial atoms embedded in the lattice of host materials. These atom-like defects could vibrate around their lattice sites and form vibrational energy levels. The vibration motion can be explained by the configuration coordinate model assuming harmonic oscillator approximation [61,62]. The vibrational energy separation, or phonon energy, can be written as:

$$\hbar\omega = E_{n+1} - E_n \quad 1.6.1$$

where  $E_n$  and  $E_{n+1}$  are two adjacent vibronic energy levels.

According to the Franck-Condon principle [63,64], the transitions between the ground state and excited state in the energy level diagram of Fig.1.6.1 are vertical. Therefore, the transition should more likely happen in the two energy levels whose wave functions have overlap that is more significant. The probability of the transition is given by [64]:

$$P \propto | \langle \Psi(v_1) | \Psi(v_2) \rangle |^2 \quad 1.6.2$$

Where the  $\Psi(v_1)$  and  $\Psi(v_2)$  are the wave functions of the initial and final states. The overlap integral is called Franck-Condon factor.

### **The excitation and relaxation cycle in the PL process**

The excitation and relaxation cycle of defects starts from the bottom of the ground state to one of the vibrational levels of the excited state by absorbing light. Then, the excited state electrons decay to the bottom of the excited state by emitting phonons. After that, the electrons in the bottom of the excited state further relax to one of the vibrational levels of the ground state and emit photons during this period. If the relaxation is direct to the bottom of the ground state, a ZPL in the PL spectrum is observed. Otherwise, the PSB is expected. The excitation and relaxation cycle and theoretical PL spectrum is shown in Fig 1.6.1. Obviously, the ZPL possesses the same energy with the energy gap between the ground state and excited state of the defect, providing a spectroscopic tool for the unambiguous identification of optically active defects. The PSB provides information about the local vibrational structure of quantum defects. Identifying defects by ZPL has been widely used in the investigation of quantum defects in semiconductor materials, which was discussed in section 1.4. However, for the investigation of the vibrational structure of defects, PL spectroscopy cannot be applied. This will be discussed later.

### **The effect of local vibration on the spin defect centers**

The electron-phonon interaction leads to light emission by PSB instead of the ZPL. A perfect single photon emitter requires a high emission rate by ZPL. The Debye-Waller

(DW) factor, the ratio of light emitted to the ZPL relative to all, spectrally integrated light emitted can characterize this. The DW factor can be written as:

$$DW = \frac{\int_{eV} ZPL}{\int_{eV} PL} \quad 1.6.3$$

This parameter can be calculated by Huang-Rhys theory [67]. An ideal single photon emitter in the quantum application requires a high photon emission rate at the ZPL and as low as possible emission from the phonon sidebands. Hence, the DW factor is a very important parameter to characterize a single photon emitter. The phonon energy  $\Delta E$  ( $\hbar\omega$ ), which was aforementioned, is the quantized energy absorbed or emitted in the vibronic transition. This parameter can also be measured by a PL spectrum, which is only from one type of defect. The value equals to the energy distance of ZPL and the first phonon replica or the adjacent phonon replicas.

$$\Delta E = E_{ZPL} - E_{P_1}, \text{ or } \Delta E = E_{P_{n+1}} - E_{P_n} \quad 1.6.4$$

Where,  $E_{ZPL}$  is the energy of ZPL,  $E_{P_n}$  is the energy of the  $n^{\text{th}}$  phonon replica. The importance of investigating the phonon energy  $\Delta E$  is that this parameter has a strong relationship with the spin lattice relaxation time  $T_1$ , which determines the absolute limit for spin coherence at intermediate temperatures. Their relation can be described by the function [65]:

$$\frac{1}{T_1} \propto \left( e^{\frac{\Delta E}{k_B T}} - 1 \right)^{-1} \quad 1.6.5$$

This indicates that the vibrational signatures of defects play an important role in the characterization of spin defects.

### **The limitation of PL spectroscopy**

From the discussion above, it is clear that the characterization of the local vibrational structure of spin defects is crucial. However, quite a few papers focus on this aspect and most of them are solely devoted to theoretical calculations [66,67].

To investigate the DW factor or  $\Delta E$  of a specific type of defect, an isolated PL spectrum of this type of defect is needed. However, as shown in Fig1.4.4 (a), there is a severe

problem in the PL spectra. The polytypism of SiC and the defect fabrication technology give rise to more than one kind of defect species in SiC samples. In addition, the excitation laser can excite any defects whose energy gaps are smaller than the laser energy. These problems result in the overlapped PL contribution from different defects in the same PL spectrum. For instance, in Fig 1.4.4 (a), the PL intensity of V2-ZPL is overlapped by the phonon sidebands of V1 defect. Likewise, the PL spectra of all VV defects in 4H-SiC are covered by the long tail of the V2 PSBs, which makes the investigation of the local vibrational structure impossible. In this case, it is necessary to find a way to obtain the separated PL spectrum of each defect.

## **Chapter 2 Microwave-assisted spectroscopy**

This chapter introduces a new approach to measure the local vibrational structure for a specific type of defect with the help of modulated microwave, which is the so-called MW-assisted spectroscopy. By this approach, one can spectrally isolate each  $V_{Si}$  and VV defects in 4H- and 6H-SiC. With the separated PL spectra, the problem of the overlapping PL contributions from different defects will be solved.



## 2.1 Fundamentals of MW-assisted spectroscopy

### Optically-detected magnetic resonance

To explain the MW-assisted spectroscopy, we should start from the optically detected magnetic resonance (ODMR) method. With the development of the investigation techniques of spin defects, ODMR has become a standard approach to optically manipulate the spin state of defects in semiconductors. The detail of the theory of ODMR can be found in ref. [68]. In this chapter, a brief introduction will be given through an example of the  $V_{Si}$  defect in 4H-SiC. In section 1.4, it was discussed that the spin number of  $V_{Si}$  is  $3/2$ . Its ground state has two spin sublevels with an energy gap named zero-field splitting energy at zero magnetic field as shown in Fig. 1.4.2. The mechanism of the zero-field ODMR associated with the  $V_{Si}$  defects is qualitatively explained in Fig. 1.4.2 (a). The  $V_{Si}$  has spin  $S = 3/2$  in the ground state (GS) and excited state (ES). Optical excitation of the  $V_{Si}$  defect into the ES is followed by two processes, radiative recombination to the ground state GS and nonradiative spin-dependent relaxation through the metastable state (MS). Application of the resonant MW field which is equal to the ground-state zero-field splitting between the  $m_S = \pm 1/2$  and  $m_S = \pm 3/2$  states, changes the population of these spin sublevels. It breaks the equilibrium between the relaxation processes resulting in non-zero  $\Delta PL$ . As a result, a  $\Delta PL/PL$  can be measured. Fig. 2.2.1 (b) presents a typical ODMR signal of V2 in 4H-SiC. When the frequency of scanning microwave equals to the resonant frequency (70 MHz for V2 in 4H-SiC), a peak in the  $\Delta PL/PL$  signal emerges. This is what is understood as optically-detected magnetic resonance. This approach is widely used in the detection of spin properties of many types of spin defects.

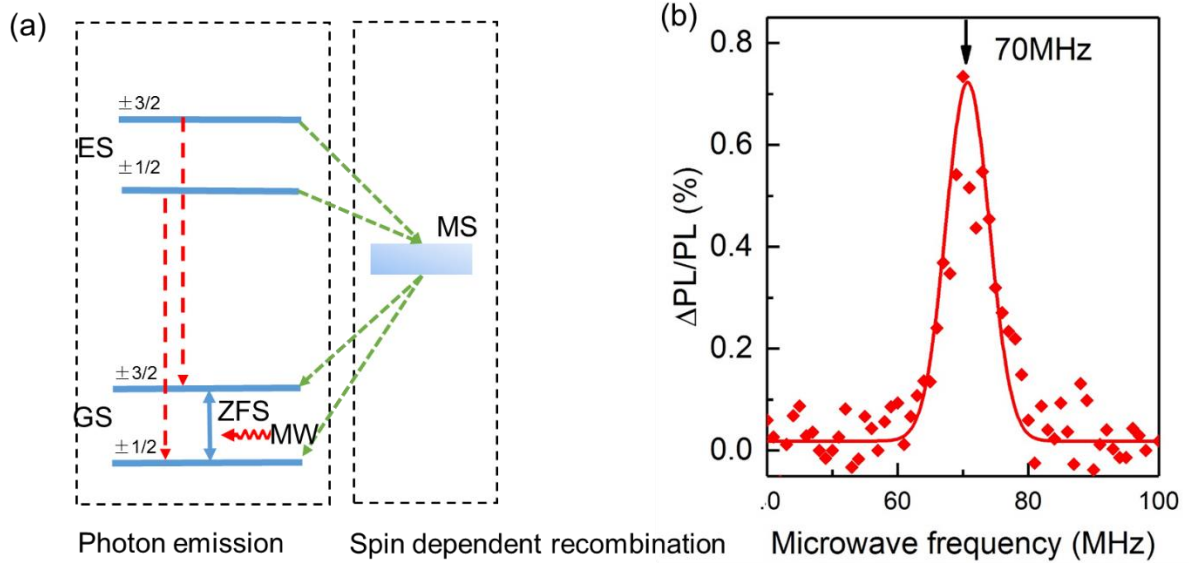


Figure. 2.1.1 (a) The fine structure of  $V_{Si}$  defect in 4H-SiC. The left dash box presents the radiative transition. The right box shows the spin-dependent recombination. (b) The typical ODMR signal depending on microwave frequency. At resonant condition (the energy of microwave equals to the ZFS energy), there is a PL intensity change resulting in a peak in the ODMR spectrum.

### MW-assisted spectroscopy

The MW-assisted spectroscopy is inspired by the ODMR method. We can obtain the resonant MW frequency for every spin defect from ODMR measurements. The results of all measured spin defects show that almost all quantum defects have their own unique resonant frequencies, which is shown in table 4.1 in chapter 4. This gives the opportunity to separate different species of defects by selecting a resonant microwave frequency. If the resonant microwave is modulated for a specific spin defect center (such as 70MHz for  $V_2$  in 4H-SiC), a modulated  $\Delta PL$  only corresponding to this defect will be obtained. With the help of a lock-in amplifier, a  $\Delta PL$  spectrum as a function of wavelength can be recorded. This is the principle of the MW-assisted spectroscopy.

### Lock-in amplifier

The realization of MW-assisted spectroscopy measurement relies on the help of lock-in amplifier. It can separate  $\Delta PL$  signal and PL signal by a reference frequency. The basic principle of a lock-in amplifier can be described by the function [69]:

$$V_{out} = V_{sig} \sin(\omega_s t + \theta_{sig}) V_{ref} \sin(\omega_{ref} t + \theta_{ref}) \quad 2.1.1$$

Where  $V_{sig} \sin(\omega_s t + \theta_{sig})$  is the real signal with frequency  $\omega_s$ ,  $V_{ref} \sin(\omega_{ref} t + \theta_{ref})$  is a reference signal with frequency  $\omega_{ref}$ .

If the signal frequency equals to the reference frequency, a DC signal is obtained in the following form:

$$V_{out} = \frac{1}{2} V_{sig} V_{ref} \cos(\theta_{sig} - \theta_{ref}) \quad 2.1.2$$

If the signal frequency is different from the reference frequency, two AC signals at the frequency  $(\omega_s + \omega_{ref})$  and  $(\omega_s - \omega_{ref})$  will be generated.

However, a low-pass filter can remove AC signals. The DC signal at the reference frequency will be left at the end as shown in Fig 2.1.2.

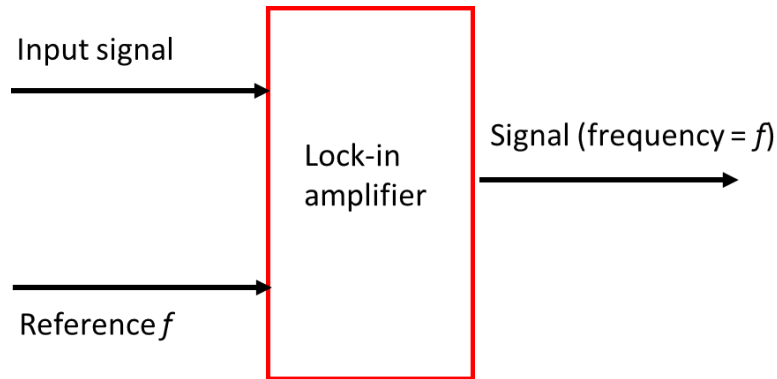


Figure 2.1.2 Simplified working principle of a lock-in amplifier.

### The signal reading by lock-in amplifier

Fig. 2.1.3 shows the difference of signal sequence in PL and  $\Delta$ PL measurements. In PL measurements, a chopper modulates the excitation laser, and the frequency of the chopper is used as the reference signal. Hence, the lock-in amplifier can read out the PL signal. In the MW-assisted spectroscopy, the chopper is removed. The resonant MW is modulated by a frequency that is used as a reference frequency for the lock-in amplifier. A constant PL and a modulated  $\Delta$ PL signal at the reference frequency are registered in the detector:

$$V_{sig} = \Delta PL_{modulated} + PL_{constani} \quad 2.1.3$$

With the help of the lock-in amplifier, one can successfully read out this  $\Delta PL$  signal. This is how our new approach MW-assisted spectroscopy works.

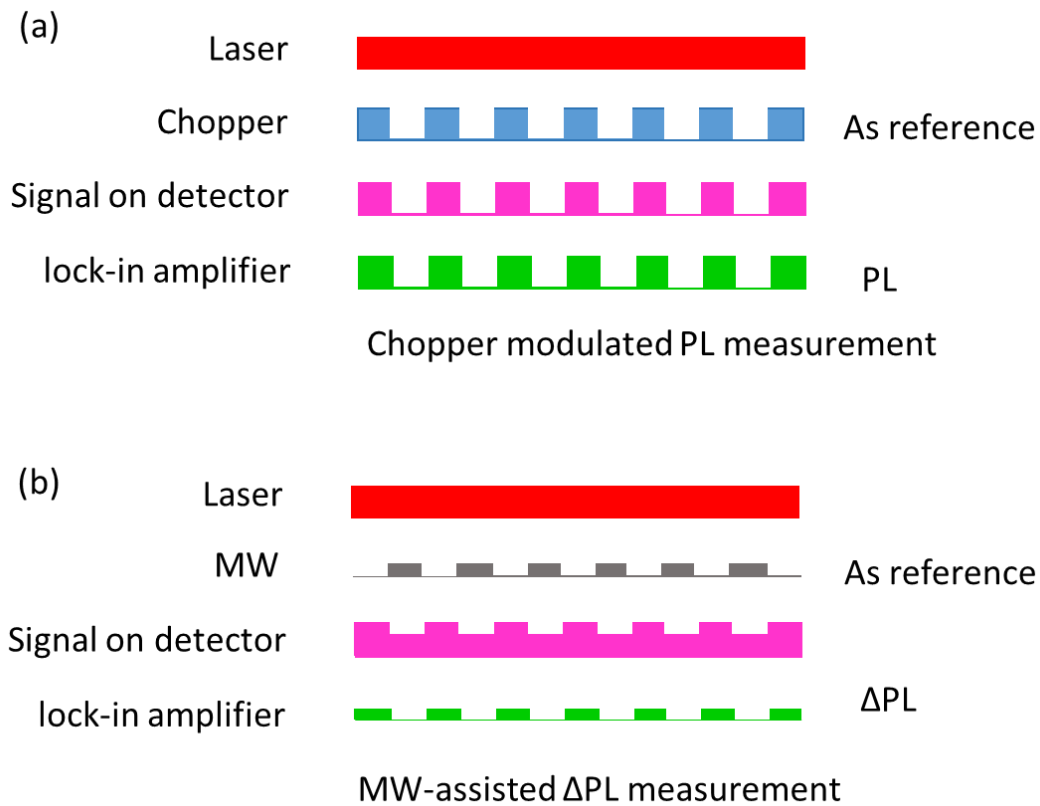


Figure 2.1.3 (a) Chopper modulated laser excitation and PL signal. (b) MW sequences and modulated  $\Delta PL$  signal.

### **An example of a MW-assisted $\Delta PL$ spectrum compared with its PL spectrum.**

In section 1.6, it was discussed that the PL spectrum of a specific defect includes contributions from other defects. The limitation of PL spectroscopy is clearly shown in Fig. 2.1.4 (a). ZPL and PSBs of V2 are overlapped by the contribution of PSBs of V1 and the long tail of V2 PSBs covers ZPLs of VVs (see fig. 1.4.4a). Because of the overlapping contributions, the intensity of ZPLs and the location of PSBs are not reliable.

Fig. 2.1.4 (b) shows an example of MW-assisted spectroscopy, the  $\Delta PL$  spectrum of V2 in 4H-SiC. In this figure, one can find a pure V2 spectrum with no contributions from other defects. From this spectrum, the location of the vibrational mode and the polarization properties of V2 defects in 4H-SiC can readily be obtained, which will be shown in the next chapters dealing with the experimental results. In other words, the

MW-assisted spectroscopy holds promise for investigating the optical, spin and vibrational properties of spin defects in solids.

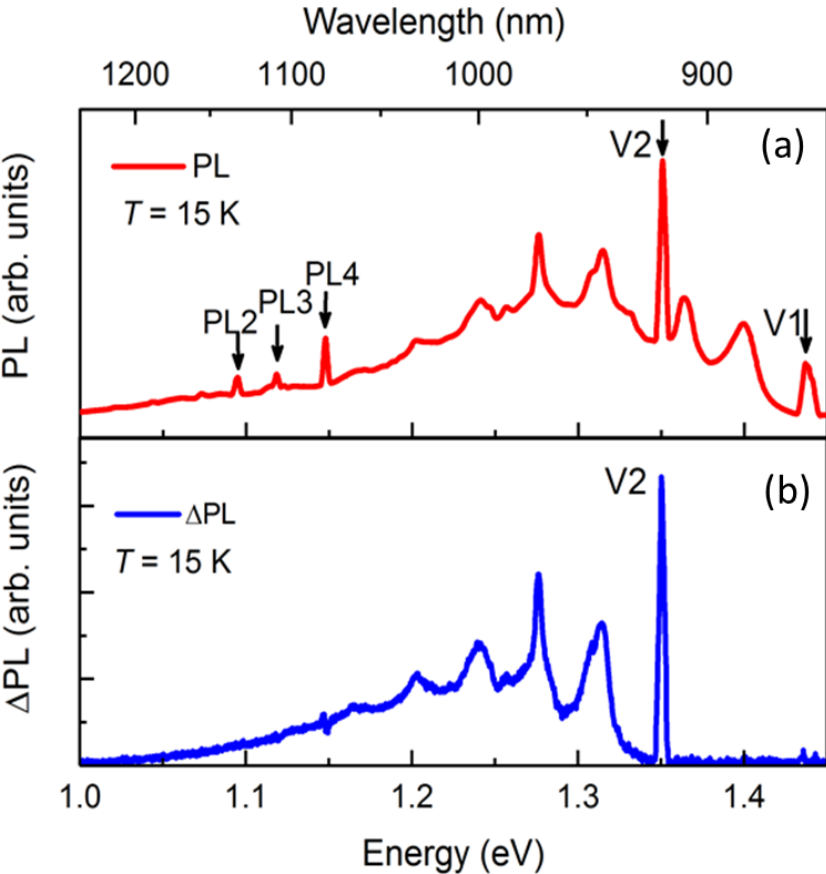


Figure 2.1.4 (a) PL spectrum of V2 in 4H-SiC in the wavelength range of 850-1250 nm. (b) MW-assisted  $\Delta$ PL spectrum of V2 in 4H-SiC in the same wavelength range.

## 2.2 Home-built setup

All measurements, including PL, ODMR and MW-assisted spectroscopy were performed on a home-built setup as shown in Fig. 2.2.1. This setup can be divided into five parts: the excitation system, the optical path, the signal read-out system, the temperature control system and the MW pumping system.

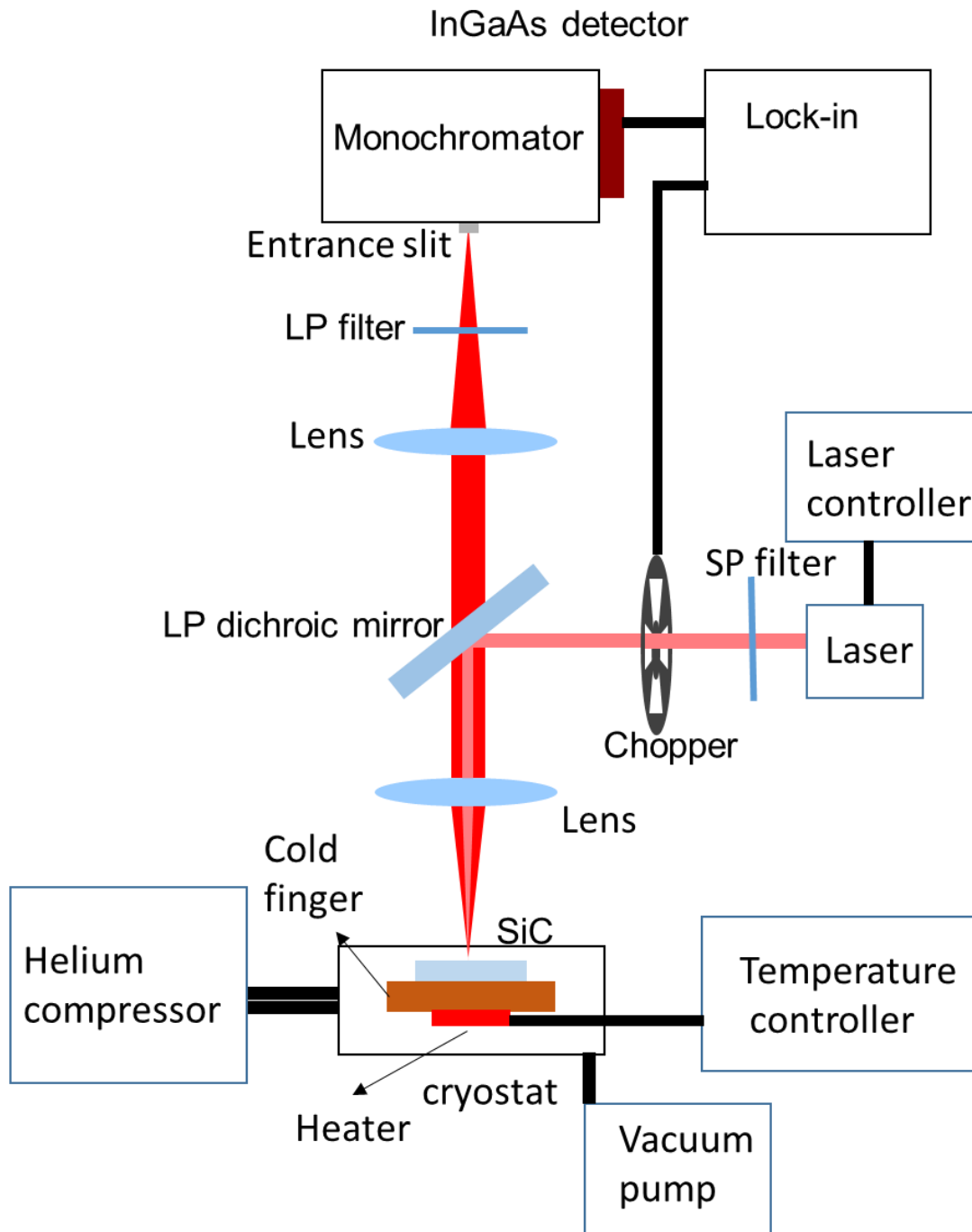


Figure 2.2.1. Schematic diagram of our home-built setup for PL, ODMR and MW-assisted spectroscopy measurement.

## Sample excitation system

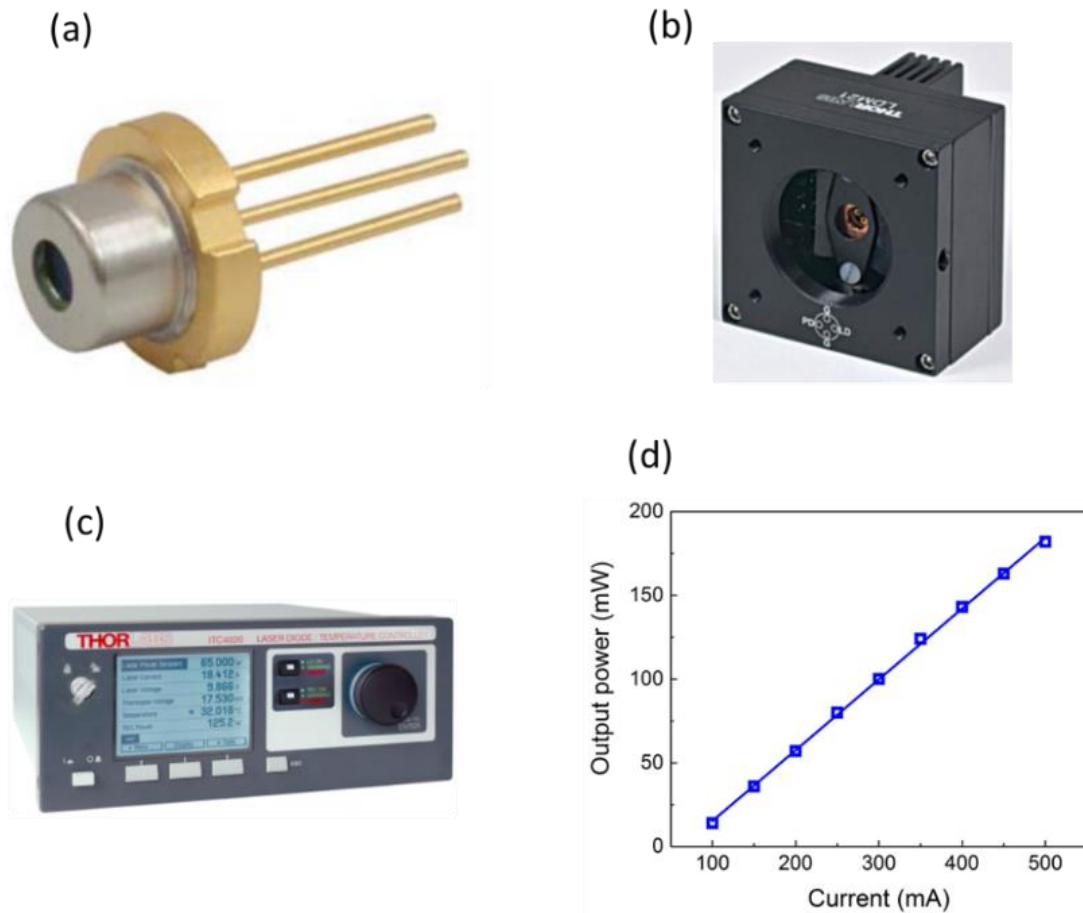


Figure 2.2.2 (a) The 808-nm laser diode. (b) the LDM21 laser diode mount. (c) the ITC4000 laser temperature and power controller. (d) the laser output power as a function of the input current.

The excitation or spin initialization is carried out by a 808-nm multimode laser diode (mounted in a LDM21 laser diode mount) and its current and temperature controller (ITC4000 laser controller) bought from Thorlabs, which are shown in Fig. 2.2.2. The maximum output power is more than 180 mW, which is suitable for most of the luminescence measurements. The laser output power as a function of input current measured by a power meter is depicted in Fig. 2.2.2 (d). It can also produce pulses with a frequency up to 100 kHz by programming the laser controller. Another advantage, compared with a solid-state laser, is the fact that the laser wavelength can be changed by changing the laser diode. For example, for high efficient excitation of VV defects in SiC, the laser diode can be changed to a 940-nm laser diode.

## Optical path

The optical path consists of several filters and lenses, which are employed to guide the excitation laser, as well as to clean and collect the luminescence signal. As shown in Fig. 2.2.1, a short-pass filter with a cut-on wavelength of 825 nm is used to clean the excitation laser. A long-pass dichroic mirror with an 850 nm cut-on wavelength is used to separate the excitation laser from the emitted PL signal. Two lenses are used in the light path to focus the excitation laser onto the sample as well as to collect and focus the PL signal from the sample into the entrance slit of the monochromator. A long-pass filter with 850 nm cut-on wavelength is used to eliminate laser contributions and in turn protect the detector.

## Signal read-out system



Figure 2.2.3 (a) TRIAX 322 monochromator. (b) IGA-020-E-LN7 infrared light detector mounted in LN7 Downview Dewar. (c) SR830 DSP lock-in amplifier.

This part includes a monochromator, an InGaAs detector and a lock-in amplifier. The collected PL or  $\Delta$ PL signal is spectrally resolved in the monochromator (TRIAX 322). This monochromator has two gratings: one is for the infrared range, another is for the visible range. All measurements in this thesis are performed with the infrared grating. Its spectral resolution depends on the size of the entrance and the exit slits. The slit size can also be used to control the signal intensity. For example, if the signal is very weak, one can choose a larger slit size to enhance it at the expense of losing spectral resolution. Typically, a 0.5 mm slit size is used for low-temperature high-resolution measurements; while the slit size is set to 1 or 2 mm for room-temperature low-resolution measurements. The monochromatic light is converted into photovoltage by an InGaAs detector (IGA-020-E-LN7) and a built-in transimpedance amplifier, which are mounted in an LN7 Downview Dewar that is coupled to the monochromator by an optical interface. In this



thesis, two working temperatures of the detector were employed: room temperature (23 °C) and liquid nitrogen temperature (-196 °C) by directly pouring liquid nitrogen into the Dewar. Fig 2.2.4 presents the wavelength response of our InGaAs detector for three working temperatures (supported by Electro-Optical Systems Inc.). In the wavelength range of 1000 - 1450 nm, there is no obvious difference for these three temperatures. However, the detector shows better sensitivity at low-temperatures for wavelengths shorter than 1000 nm. Since the spectral range to investigate both  $V_{Si}$  and  $V_V$  was set to 850-1300 nm, the detector at low temperature was used for the measurements. Considering the fact that the detector sensitivity depends on the wavelength, all the experimental results were corrected by this wavelength response curve.

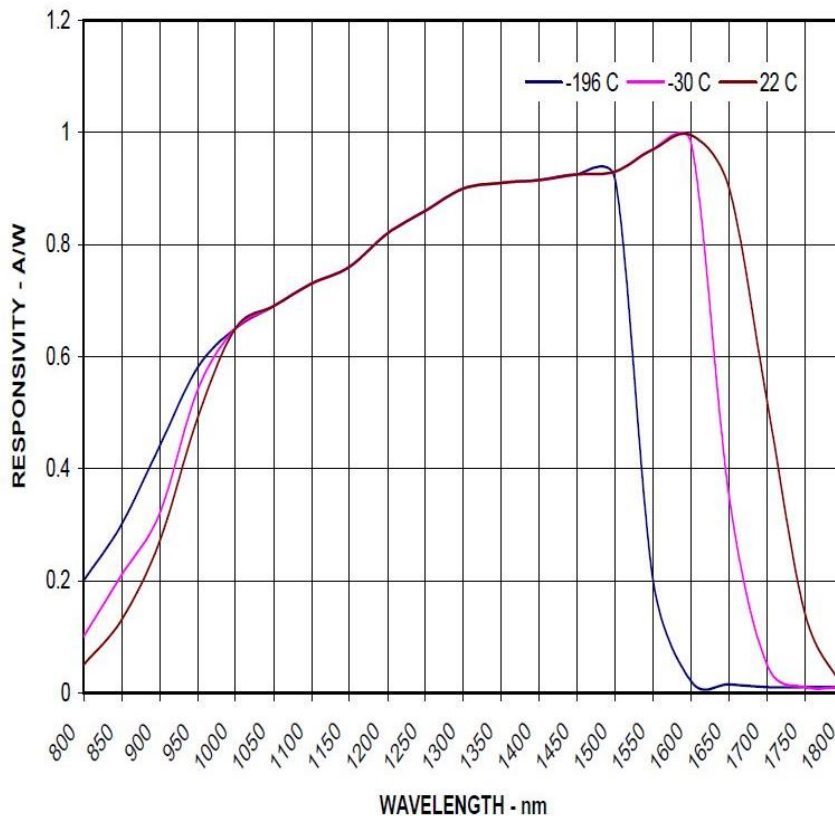


Figure.2.2.4 InGaAs detector responsivity as a function of wavelength. This figure is taken from the device manual of IGA-020-E-LN7.

A lock-in amplifier (SR830 DSP lock-in Amplifier) reads out the photosignal. The theory of the lock-in amplifier can be found in section 2.1. For the PL measurements, the frequency of the chopper is the reference frequency of the lock-in amplifier. For

ODMR and MW-assisted spectroscopy measurements, the modulation frequency of the resonant microwave is used as the reference frequency.

### Cooling system

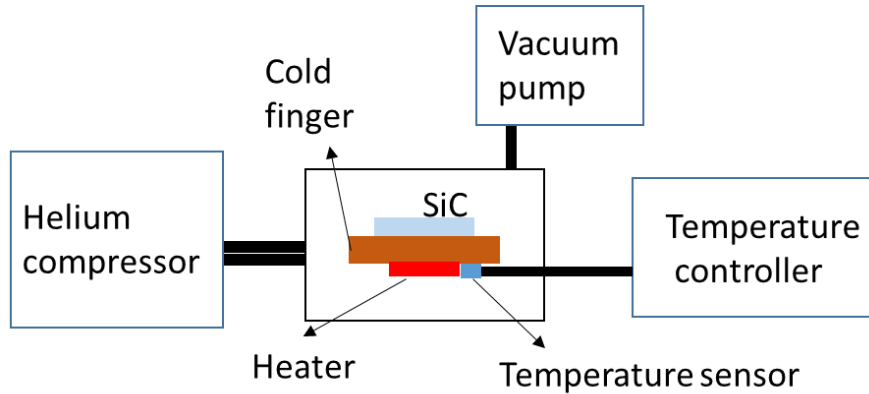


Figure 2.2.5 A schematic diagram of cooling system.

The cooling system consists of a vacuum chamber, a helium compressor, a vacuum pump and a temperature controller. The sample is placed on a sample holder, which is connected with a cold finger and a heater in a vacuum chamber. A mechanical vacuum pump is used to vacuum the chamber. A helium compressor is employed to pump liquid helium into the cold finger to cool down the sample until the desired temperature. A heater and a temperature sensor stick on the cold finger and are connected to a temperature controller for the temperature control. The temperature measured near the sample ranges from 15 to 300 K, which is good enough for the low- and room-temperature PL measurements.

### Microwave pumping system

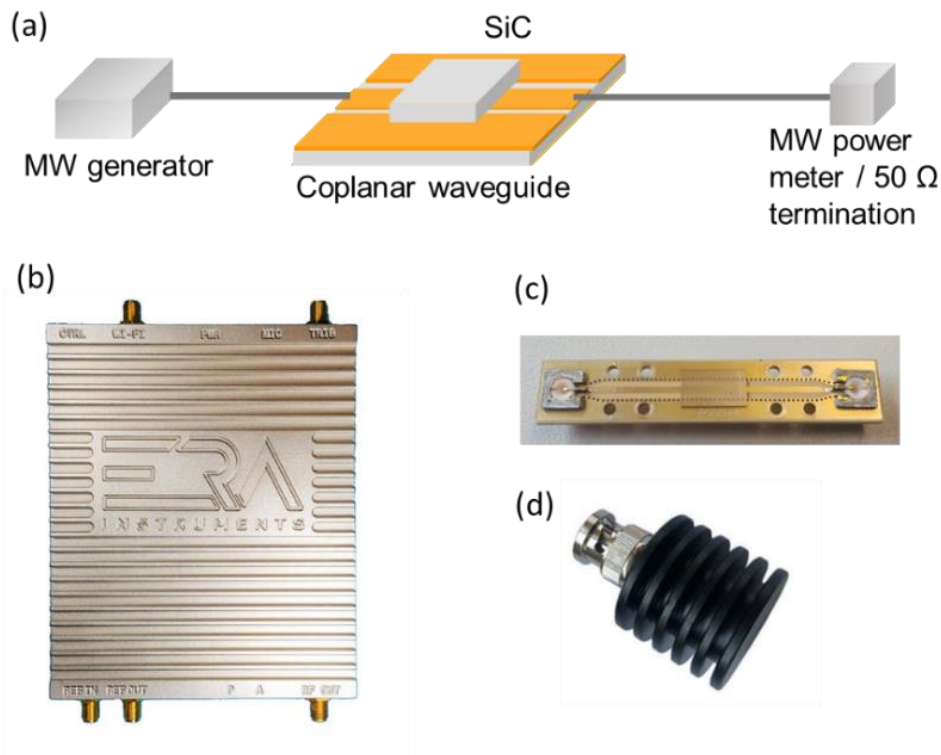


Figure 2.2.6 (a) A schematic diagram of the microwave pumping system. (b) ERASynth+ microwave generator. (c) Home-built coplanar waveguide. (d) 50-Ohm microwave termination.

The core part of the setup for the MW-assisted spectroscopy is the microwave pumping system. It includes three devices: a microwave generator, a coplanar waveguide, and a 50-Ohm microwave termination. All three devices are connected by standard 50-Ohm coaxial cables shown in Fig. 2.2.6 (a). The microwave generator is an open source and Arduino-compatible device bought from ERA instruments. It provides a microwave in the range of 250 kHz - 15 GHz with a maximum output power up to 12 dBm. The most important parameters are listed in table 2.2.1

<b>Name</b>	ERASynth+
<b>Frequency Range</b>	250 kHz to 15 GHz
<b>Maximum Output Power</b>	12dBm
<b>RF Output Impedance</b>	50 Ohm
<b>External modulation input voltage</b>	$0 \pm 1.65V$

Table 2.2.1 Basic parameters of the ERASynth+ microwave generator. The values are taken from the device manual of ERASynth+.

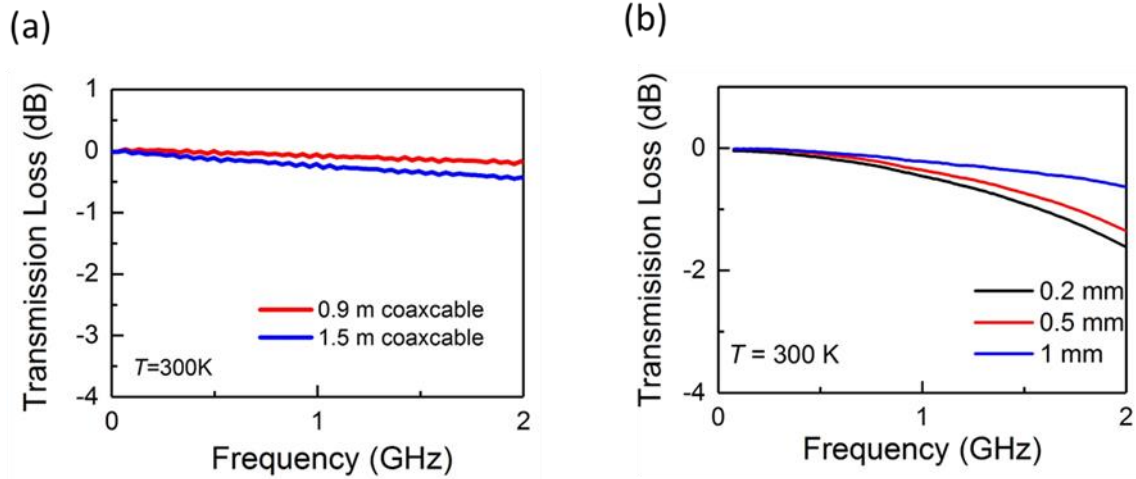


Figure 2.2.7 Microwave transmission loss as a function of microwave frequency in (a) coax cable and (b) three different coplanar waveguides.

The coplanar waveguide is a self-designed electrical planar transmission line with a 50-Ohm impedance, matched with the microwave generator. It is designed into three modules for different application scenarios based on the width of the waveguide (1 mm, 0.5 mm, and 0.2 mm). A 50-Ohm microwave termination is used to absorb the extra microwave and eliminate the microwave reflection. For ODMR and MW-assisted spectroscopy measurements, the lock-in amplifier externally modulates (“triggers”) the microwave generator. This modulation frequency is also used as the reference frequency of the lock-in amplifier for reading out the signal. The modulated microwave is guided into the coplanar waveguide and absorbed by defects leading to defect spin polarization. Fig. 2.2.7 presents the microwave transmission loss in the coaxial cables and the coplanar waveguide measured by a microwave analyzer (Keysight FieldFox N9918A). The power loss at frequencies between 0 and 2 GHz (the used range in  $V_{Si}$  and VV defects) is less than 2 dB.

### Parameter characterization and optimization

Before the ‘real’ measurements, the first mission is to optimize the setup and select all optimal parameters. This section will be devoted to discuss the MW-assisted spectroscopy measurements at different conditions by using the  $V_{Si}$  as an example. After these tests, the optimal parameters for the measurements in the next three chapters will be chosen. The  $\Delta PL$  spectra as a function of slit sizes are measured on  $V_2$  of  $V_{Si}$  in 6H-

SiC. All other parameter characterization and optimization measurements are performed on V2-ZPL in 4H-SiC as examples.

Figure 2.2.8 presents the  $\Delta$ PL intensity of V2 in a commercial 4H-SiC wafer ( $0.3 \times 5 \times 5 \text{ mm}^3$ ) as a function of the width of the coplanar waveguides at room temperature. In this case, the 0.5-mm-width waveguide has the best  $\Delta$ PL intensity. Hence, all the ODMR and MW-assisted spectroscopy measurements for  $V_{\text{Si}}$  in 4H-SiC wafer are performed by using the 0.5-mm-width microwaveguide. Fig. 2.2.9 shows the  $\Delta$ PL intensity at V2-ZPL as a function of the excitation laser power and microwave power, respectively. From these measurement results, one can conclude that the  $\Delta$ PL intensity is proportional to the laser power (at units of mW) and microwave power (at units of dBm). Therefore, the selected laser power and microwave power are as high as possible to get a stronger  $\Delta$ PL signal in the measurements, although the measuring range of the detector also limits the laser power.

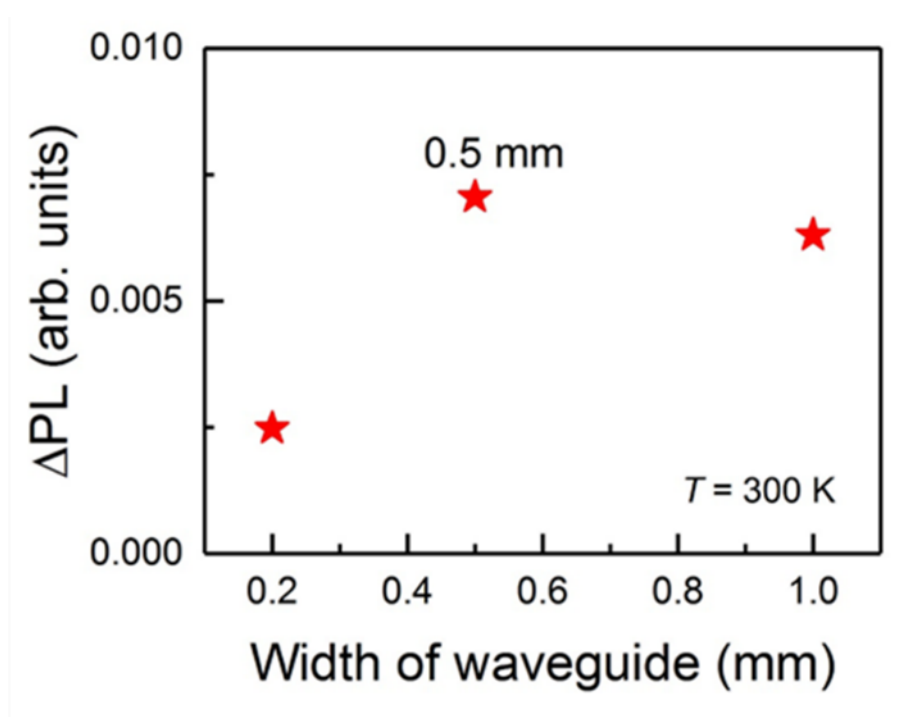


Figure 2.2.8  $\Delta$ PL intensity of V2-ZPL in 4H-SiC as a function of the width of the coplanar waveguide.

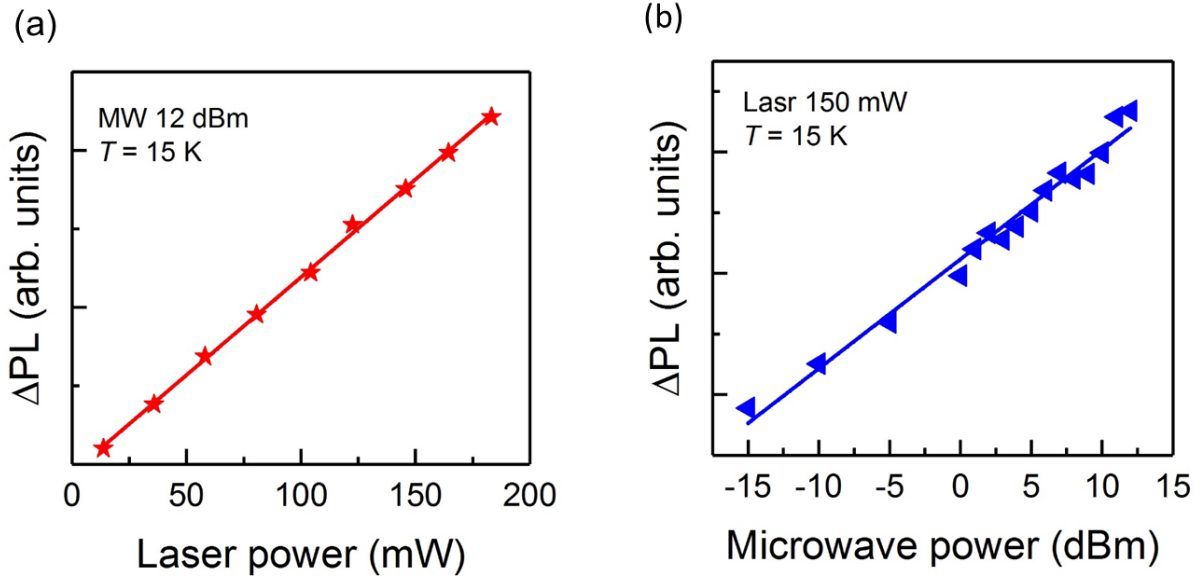


Figure 2.2.9  $\Delta PL$  intensity of ZPL of V2 in 4H-SiC as a function of the excitation laser power (a) and microwave power (b) at 15 K.

Another parameter, which is important in the  $\Delta PL$  measurements, is the size of the entrance slit of the monochromator. The different sizes of the monochromator entrance slit give different signal intensity and spectral resolution, leading to a different line shape for the same defect. The question is if the DW factor and the phonon energy depend on the slit size. Therefore, the MW-assisted spectroscopy is measured as a function of the slit size (Fig. 2.2.10). The  $\Delta PL$  spectra of V2 in 6H-SiC measured at a slit size of 0.5 and 1 mm are shown in Fig. 2.2.10. Although the line shape and the spectra resolution for the two different slit sizes are different, the DW factor and phonon energy  $\Delta E$  of V2 in 6H-SiC show no differences. In other words, the slit size of the monochromator has no influence on the determination of the DW factor.

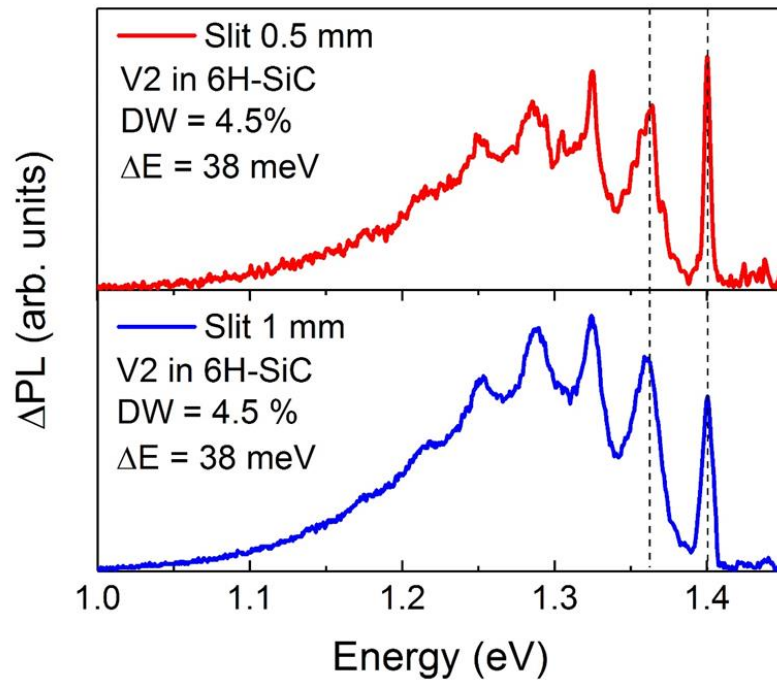


Figure 2.2.10 MW-assisted  $\Delta PL$  spectra at slit size of 0.5 mm (a) and 1 mm (b), respectively. In the measurement, all other parameters are the same except the size of the entrance and exit slits of the monochromator.

# **Chapter 3 Local vibrational modes of Si vacancy spin qubits in 4H-SiC**

The results of this chapter were published in “Z. Shang, A. Hashemi, Y. Berencén, H.-P. Komsa, P. Erhare, S. Zhou, M. Helm, A. V. Krasheninnikov, and G. V. Astakhov, Local vibrational modes of Si vacancy spin qubits in SiC, *Phys. Rev. B* 101, 144109 (2020).” The thesis author measured all experiments results in this chapter. A. Hashemi and A. V. Krasheninnikov did the theoretical calculation.

In this chapter, we uncover the local vibrational modes of the Si vacancy spin qubits in as-grown 4H-SiC. We apply microwave-assisted spectroscopy to isolate the contribution from one particular type of defects, the so-called V2 center, and observe the zero-phonon line together with seven equally separated phonon replicas. The results are compared with first-principles calculations of the photoluminescence line shape, which are in excellent agreement with our experimental data. A resonance phonon energy of 36 meV and a Debye-Waller factor of about 6% are obtained. We establish experimentally that the activation energy of the optically induced spin polarization is given by the local vibrational energy. Our findings give insight into the coupling of electronic states to vibrational modes in SiC spin qubits, which is essential to predict their spin, optical, mechanical, and thermal properties. The approach described can be applied to a large variety of spin defects with spectrally overlapped contributions in SiC as well as in other three and two-dimensional materials.



### 3.1 Introduction

As discussed in previous chapters, intrinsic point defects in silicon carbide [20,70-72] have been widely used to implement room-temperature quantum emitters [17,40,73] as well as to realize quantum sensing of magnetic fields [74-78], electric fields [79] and temperature [43,80,81]. Particularly, silicon vacancies ( $V_{Si}$ ) and silicon-carbon divacancies (VV) in SiC reveal extremely long spin coherence time [82-86] and hold promise to implement quantum repeaters due to inherent spin-photon interface and high spectral stability [87,88]. Existing device fabrication protocols on the wafer scale in combination with three-dimensional (3D) defect engineering [53] allow manufacturing integrated quantum devices [89-92] with electrical [93-95] and mechanical [96,97] control of defect spin qubits. SiC nanocrystals with color centers are also suggested as fluorescence biomarkers for biomedical applications [98,99].

Vacancies can be imagined as artificial atoms incorporated into the SiC lattice. The communication with them is usually realized through optical excitation and photoluminescence (PL) detection. Unlike atoms, radiative recombination in point defects is accompanied by phonon emission due to the interaction with lattice vibrations. This process results in the PSB, which is spectrally shifted towards longer wavelength relative to the ZPL [100]. A high ratio of the emitted light from the ZPL to the all emitted light, is necessary for the implementation of quantum repeaters. The local vibrational energy also contributes to the spin-lattice relaxation time  $T_1$  [65].

Although the understanding of the PSB is important for quantum applications, it has not been investigated systematically in SiC. The previous works [101] are limited to the report on the upper limit for the DW factor in a single  $V_{Si}$  defect, which is below 30%–40% depending on the crystallographic site and polytype. Most of the theoretical works are concentrated on the spin-optical properties [102-104].

This chapter deals with the measurement of the  $V_{Si}$  PL spectrum in polytype 4H-SiC, consisting of the ZPL and seven increasingly broadened phonon replicas. There are two  $V_{Si}$  defects in 4H-SiC associated with different crystallographic environments, V1 and V2 [105]. Here, the focus is on the V2  $V_{Si}$  defect. MW-assisted spectroscopy and optically detected magnetic resonance (ODMR) are used to clearly separate spectrally

overlapped contributions from other  $V_{Si}$  and  $VV$  defects. This approach allows us to unambiguously determine the  $V2$  local vibrational energy. To shed more light on the microscopic nature of the PSB, the line shape is calculated by density functional theory (DFT). The experimental line shape is very well reproduced and concurrently leads to close values for the DW factor and the local vibrational energy.

### 3.2 Experiment

The experiment is performed on our home-built setup. The samples are excited with an 808-nm laser, which is modulated by a chopper at 20 Hz. An InGaAs detector and a built-in transimpedance amplifier convert the PL intensity into a photovoltage, which is amplified and read out by a lock-in amplifier. For the ODMR measurements, the chopper is removed and a commercial signal generator provides a MW signal modulated at 20 Hz. The MW field guided into a coplanar waveguide induces spin transitions in the sample placed on the top of the waveguide. The modulated  $\Delta$ PL signal is read out by a lock-in amplifier, which is thus given in meV.

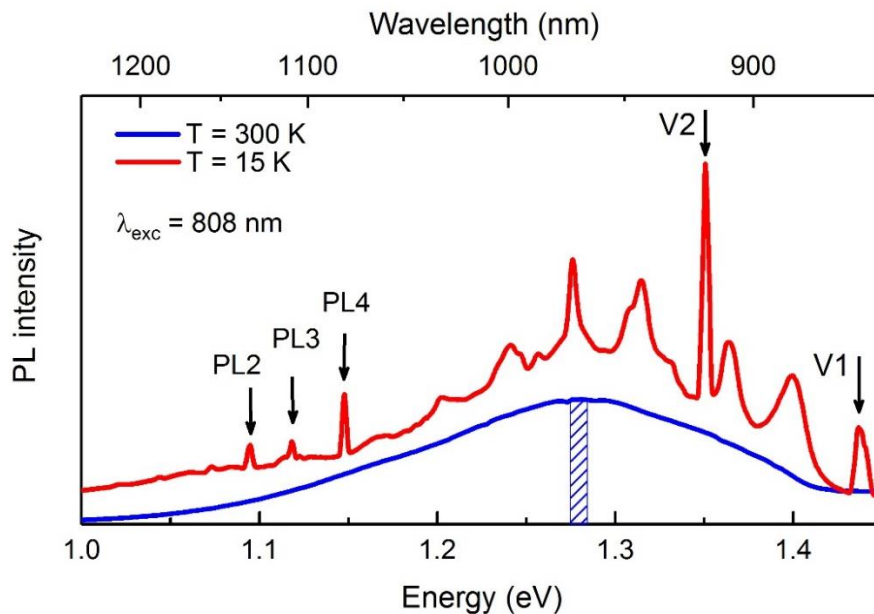


Figure 3.1 Room- and low-temperature PL from  $V_{Si}$  in pristine 4H-SiC. At  $T = 300$  K, the shadow area around 970 nm indicates the spectral resolution  $\lambda = 5.5$  nm. At  $T = 15$  K, the zero-

phonon lines of two distinct  $V_{Si}$  centers, V1 (ZPL at 863 nm) and V2 (ZPL at 918 nm), are clearly observed. The spectral resolution is  $\Delta\lambda = 1.2$  nm ( $\approx 2$  meV).

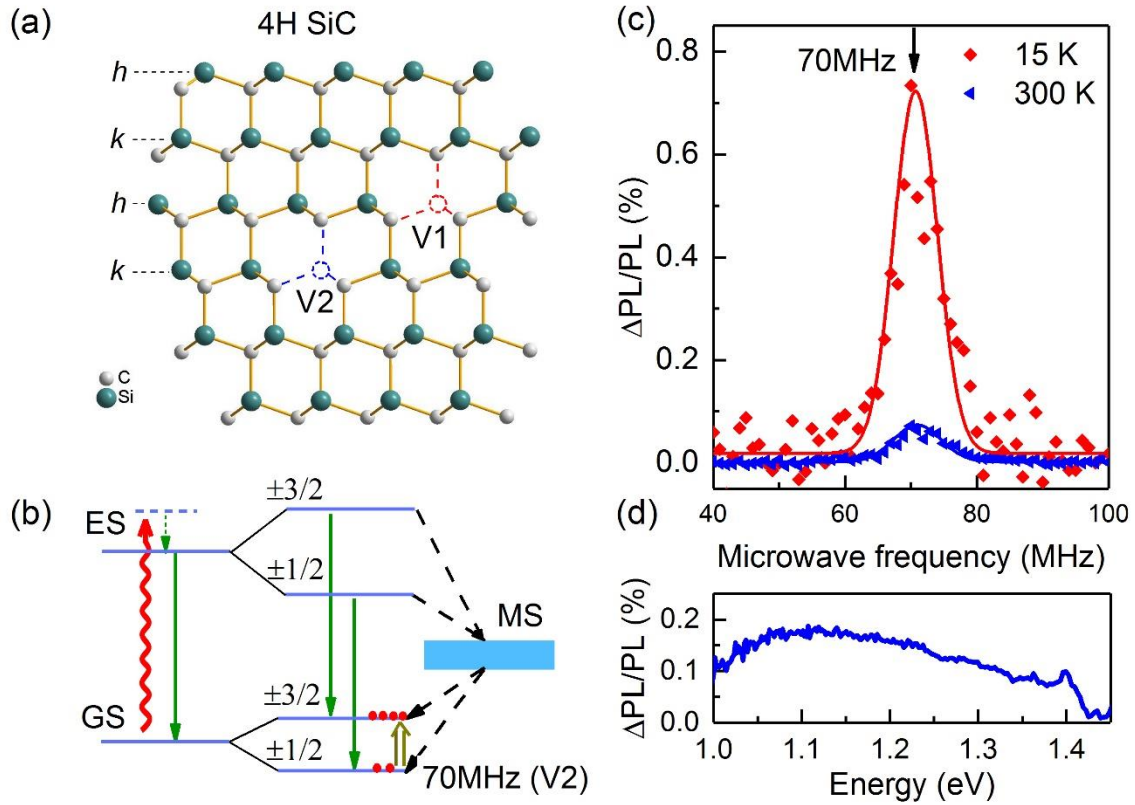


Figure 3.2 (a) Schematic representation of the V1 and V2  $V_{Si}$  defects associated with different crystallographic sites in 4H-SiC, according to [42]. (b) A scheme of the V2 spin pumping process. The red line presents the V2 spin center excited by an 808-nm laser. It relaxes to the ground state by two processes: radiative recombination (solid lines) and non-radiative spin-dependent relaxation through the metastable states (MS) (dashed lines). The double arrow shows spin manipulation by the MW field at 70 MHz. (c) The V2 ODMR spectrum at room and low temperature. The arrow indicates the resonance frequency at 70 MHz under zero external magnetic field. (d) V2 ODMR contrast ( $\Delta PL/PL$ ) at 70 MHz as a function of detection energy over the PL spectrum at room temperature.

The sample under study is diced from a pristine high-purity semi-insulating (HPSI) 4H-SiC wafer purchased from Cree. It is not irradiated and contains native  $V_{Si}$  and  $VV$  defects. The sample is mounted on the cold finger of a closed-cycle cryostat and the experiments are performed in the temperature range from  $T = 300$  K down to  $T = 15$  K.

To increase the PL intensity at  $T = 300$  K, a relatively wide monochromator entrance slit of 2 mm with a corresponding spectral resolution of 5.5 nm is used. At  $T = 15$  K, the entrance slit size is reduced to 0.5 mm to improve the spectral resolution to 1.2 nm.

Typical PL spectra of the sample under study are presented in Fig. 3.1. A broad emission band with a maximum intensity at around 1.28 eV (970 nm), associated with the  $V_{Si}$  defects [42], is clearly observed at  $T = 300$  K. The line shape of this broad emission band changes to a series of ZPLs accompanied by PSBs when the sample is cooled down to  $T = 15$  K. Two ZPLs at 1.44 eV (863 nm) and 1.35 eV (918 nm) correspond to the V1 and V2  $V_{Si}$  defects, respectively [40,42]. Several other ZPLs (labeled as PL2–PL4) are observed in the spectral range 1.1–1.2 eV and related to the silicon-carbon VV defects [106].

We concentrate on the V2  $V_{Si}$  defect, associated with one of the two possible crystallographic sites in 4H-SiC [Fig. 3.2(a)]. The mechanism of the zero-field ODMR associated with the  $V_{Si}$  defects has been explained in chapter 3.2. Therefore, no further explanation will be given again.

Fig. 3.2(c) presents the ODMR contrast ( $\Delta PL/PL$ ) as a function of MW frequency. The PL is detected at 970 nm at  $T = 300$  K (shaded area in Fig. 3.1) and at the V2 ZPL at  $T = 15$  K. To ensure that ODMR experiments are performed under optimum conditions, we investigate the laser power and MW power dependencies at different temperatures. The ODMR contrast saturates in both cases [86] and we obtain  $C_{\max} = 0.80 \pm 0.02\%$  and  $C_{\max} = 0.21 \pm 0.05\%$  for  $T = 15$  K and  $T = 300$  K, respectively [Fig. 3.2(c)]. Remarkably, the ODMR contrast only marginally depends on the detection energy over the PL band (1.1–1.35 eV) at room temperature [Fig. 3.2(d)]. This is an indication that both spin states couple to phonons in the same way. A possible explanation is weak spin-orbit coupling [107], but a theoretical consideration of the spin polarization through intersystem crossing [108] involving local vibrational states is necessary to confirm this.

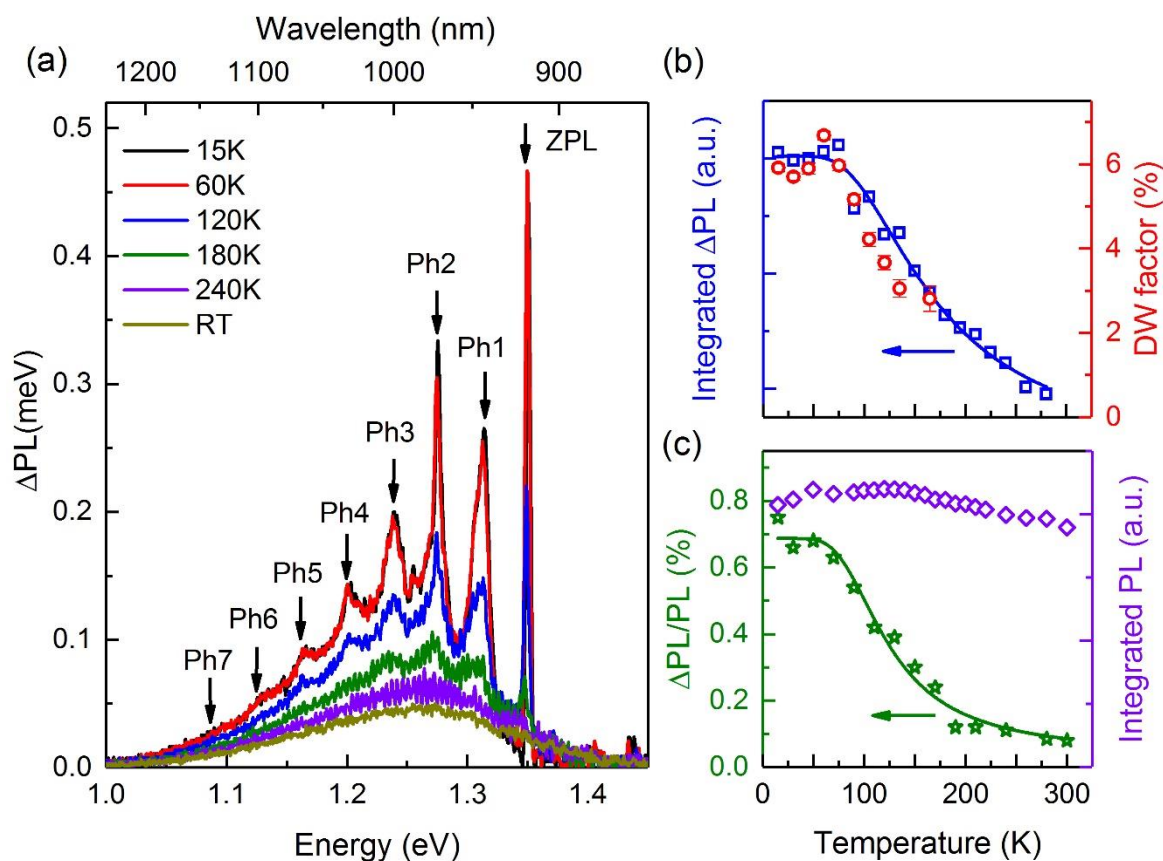


Figure 3.3 (a) Evolution of the PL spectrum with temperature under applied MW field at 70 MHz. (b) Temperature dependence of the spectrally integrated V2  $\Delta$ PL and the DW factor. The solid line is a fit to Eq. (1) with the activation energy  $E_A = 39 \pm 4$  meV. (c) Temperature dependence of the ODMR contrast  $\Delta$ PL/PL detected at the V2 ZPL and the integrated PL. The solid line is a fit to Eq. (1) with the activation energy  $E_A = 39 \pm 3$  meV and  $PL(0)$  replaced by  $PL/PL(0)$ .

Next, we analyze how the change in the V2  $\Delta$ PL emission induced by the MW depends on the detection wavelength. We set the MW frequency to 70 MHz [Fig. 3.2(c)], and the  $\Delta$ PL spectrum at  $T = 300$  K is presented in Fig. 3.3(a). With decreasing temperature, the  $\Delta$ PL spectrum changes to the ZPL along with the PSB consisting of seven equally separated phonon replicas (Ph1 – Ph7). These spectra differ from the PL spectrum presented in Fig. 3.1, which is composed of overlapping contributions from different defects. Especially, the V1 and V2 PSBs are merged, making their separation difficult. In the  $\Delta$ PL measurements, the MW frequency of 70 MHz is in the V2 spin resonance and, therefore, only the V2 PSB appears. The spectrally integrated V2  $\Delta$ PL as a function

of temperature is presented in Fig. 3.3(b). The experimental data can be well-reproduced using a single activation energy [109]:

$$\Delta PL(T) = \frac{\Delta PL(0)}{1 + C \exp\left(-\frac{E_A}{k_B T}\right)} \quad 3.1$$

We obtain from the best fit [solid line in Fig. 3.3(b)] the activation energy  $E_A = 39 \pm 4$  meV, which is equal within the experimental uncertainty to the local vibrational energy  $\Delta E_{\text{exp}} = 37 \pm 4$  meV, as discussed hereafter. The unitless coefficient  $C = 9 \pm 2$  is determined by the ratio of different relaxation rates [109]. The  $\Delta PL$  is composed by the spin polarization and the PL intensity. In order to separate these contributions, we plot in Fig. 3.3(c)  $\Delta PL/PL$  detected at the ZPL and the spectrally integrated PL. The experimental data for  $\Delta PL/PL$  can also be well fitted to Eq. 3.1 with the activation energy  $E_A = 39 \pm 3$  meV and  $\Delta PL(0)$  replaced by  $\Delta PL/PL(0) = 0.7\%$ . This indicates that the integrated PL intensity of the V2 V<sub>Si</sub> is nearly temperature independent up to 300 K. Indeed, this is in agreement with the integrated PL of Fig. 3.3(c), where a small decrease with increasing temperature can be attributed to the contribution of other defects with stronger temperature dependence.

Fig. 3.3(a) clearly shows the PSB extends below 1.1 eV (above 1150 nm). Thus, the DW above 30% found in earlier experiments [101] is definitely overestimated. Spectral integration of the experimental data in Fig. 3.3(a) [Fig. 3.4(b) shows a zoom-in of the V2 ZPL] results in the DW factor of about 6% for  $T < 60$  K. This value should be corrected by the spectrally dependent readout contrast. Given the  $\Delta PL/PL$  spectral dependence in Fig. 3.2(d), the expected value for the DW factor falls between 6% and 9%. The DW decreases with temperature as shown in Fig. 3.3(b). As the DW factor gives the fraction of elastic scattering, the temperature reduction can be attributed to the thermal motion effect [110] and multiphonon contributions.

We determine the local vibrational energy as the separation between two adjacent phonon peaks in  $\Delta E_{\text{exp}} = 37$  meV as presented in Fig. 3.4(a). The PSB formation is schematically presented in Fig. 3.4(c). The radiative recombination between the ES and the GS is accompanied by phonon emission. The energy dispersion of these phonons differs from the bulk phonon dispersion because of the broken translation symmetry in

the vicinity of the  $V_{Si}$  defect. In the next section, a detailed theoretical analysis of the local vibrational modes is presented.

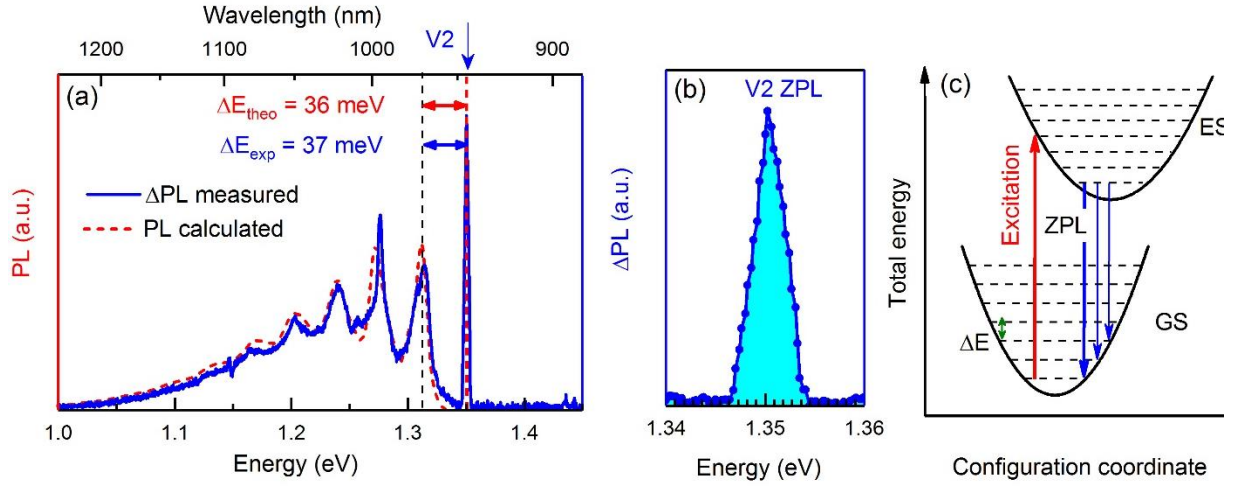


Figure 3.4 (a) Low-temperature ( $T = 15\text{K}$ ) PL of V2 as a function of the detection wavelength at the MW frequency of 70 MHz. The vertical axis for PL is the lock-in voltage of the modulated photodiode signal. The V2 ZPL (at 1.35 eV) and PSB are clearly resolved. The local vibrational energy read from two adjacent peaks is  $E_{\text{exp}} = 37\text{ meV}$ . The dashed line represents the calculation of the V2 PSB as described in the text. (b) Zoom-in of the V2 ZPL. (c) A configuration coordinate diagram for the V2 phonon modes. The blue arrows show transitions from the ES to different vibrational levels of the GS.

### 3.3 Theory

DFT calculations were carried out as implemented in VASP [111] code to determine defect properties, configurational coordinate diagrams, and vibrational modes. A plane wave basis with a cutoff energy of 450 eV was employed to represent the electronic wave functions. All structural relaxations and the vibrational properties were calculated using the PBEsol [112] exchange-correlation functional. The geometry optimization continues until the energy differences and ionic forces are converged to less than  $10^{-6}$  eV and  $0.01\text{ eV/\AA}$ , respectively. The PL line shape is calculated using the approach described in Ref. [66] and described in more detail below, which requires evaluation of the phonon spectra of the defective systems, but obtaining converged spectra requires large supercells that are very demanding computationally. Here, to speed up phonon calculations, the HIPHIVE [113] package was used to extract interatomic force constants (IFCs). Second-order IFCs were constructed using the recursive feature

elimination optimizer by including pairs and triplets up to 4.2 and 3.6 Å, respectively. The modeled IFCs result in the validation root-mean-squared error of 13 meV/Å. The phonon frequencies and eigenvectors were finally assessed using PHONOPY software [114]. To adjust the energy scales, i.e., the band gap and the position of the defect levels within, we additionally used HSE06 [115] to calculate total energies and Kohn-Sham levels. The HSE functional has been shown to reproduce intra-defect transition energies very well [116]. The calculated band gap of 3.25 eV is in excellent agreement with the experimental band gap of 3.2 eV [117].

Theoretically, the determination of the average numbers of active phonons during the optical transition for mode  $\lambda$  with frequency  $\omega_\lambda$  is given by the unitless partial Huang-Rhys (HR) factor  $S_\lambda$  defined as [118]

$$S_\lambda = \frac{1}{2\hbar} \omega_\lambda \Delta Q_\lambda^2 \quad 3.2$$

Where

$$\Delta Q_\lambda = \sum_{\alpha} \sqrt{m_\alpha} [(\mathbf{R}_{e,\alpha} - \mathbf{R}_{g,\alpha}) \cdot \mathbf{u}_\lambda] \quad 3.3$$

Here,  $\mathbf{u}_\lambda$  indicates the normalized displacement vector corresponding to mode  $\lambda$ , and  $m_\alpha$  is the mass of atom  $\alpha$ .  $\mathbf{R}_g$  and  $\mathbf{R}_e$  are the atomic coordinates in the ground and excited states. Thus,  $\Delta Q_\lambda$  describes whether the vibrational mode is parallel to the change in the atomic coordinates. The fundamental spectral density of electron-phonon coupling can be determined as

$$S(\hbar\omega) \approx \sum_{\lambda} \frac{S_\lambda}{\sigma\sqrt{\pi}} e^{-\frac{(\hbar\omega - \hbar\omega_\lambda)}{2\sigma^2}} \quad 3.4$$

where a broadening parameter  $\sigma = 5$  meV is considered. It is worth mentioning that we assume the vibrational modes in the ground state and the excited state to be identical, and we use in Eq. (3) the  $\mathbf{u}$  evaluated in the ground state. Once  $S(\hbar\omega)$  is calculated, we make use of the method of generating function [119] to derive the optical absorption spectrum



$$L(\hbar\omega) = \frac{A\omega^3}{2\pi} \int_{-\infty}^{+\infty} g(t)e^{i\omega t} dt \quad 3.5$$

where the prefactor A is the normalization constant and

$$g(t) = e^{S(t)-S(0)} \quad 3.6$$

is the generating function, where S(t) is defined by

$$S(t) = \frac{1}{2} \int d(\hbar\omega) e^{-i\omega t} S(\hbar\omega) \quad 3.7$$

The  $V_{Si}$  defect is modeled in a large 400-atom supercell using  $2 \times 2 \times 2$  meshes for k-point sampling. The V2 defect is considered as  $V_{Si}$  at the  $h$  site [42], in the  $-1$  charge state, and with spin  $S = 3/2$ . The HSE06-calculated Kohn-Sham levels are shown in Fig. 3.5(a), indicating that the V2 defect introduces several electronic states deep in the band gap. The lowest energy electron configuration has the high-spin state with three unpaired electrons ( $S = 3/2$ ). The excitation is modeled by moving spin-down electrons from the highest occupied to the first unoccupied electronic state, which is achieved by fixing the occupations of the relevant states in the DFT calculations. In the excited state, the two states related to the excitation become closer while others remain the same. From the DFT-calculated total energies, the configuration coordinate diagram can be readily extracted, as shown in. It is noted that the potential energy curve is calculated using PBEsol, but the ZPL energy difference  $[E(Q_g) - E(Q_e)]$  is obtained using HSE06. The emission energy of 1.28 eV and the ZPL of 1.35 eV are in excellent agreement with the experimental values (the former corresponding to the PSB maximum). Introduction of the V2 defect also leads to the expansion of the lattice by  $\Delta a = 0.083\%$  and  $\Delta c = 0.077\%$ .

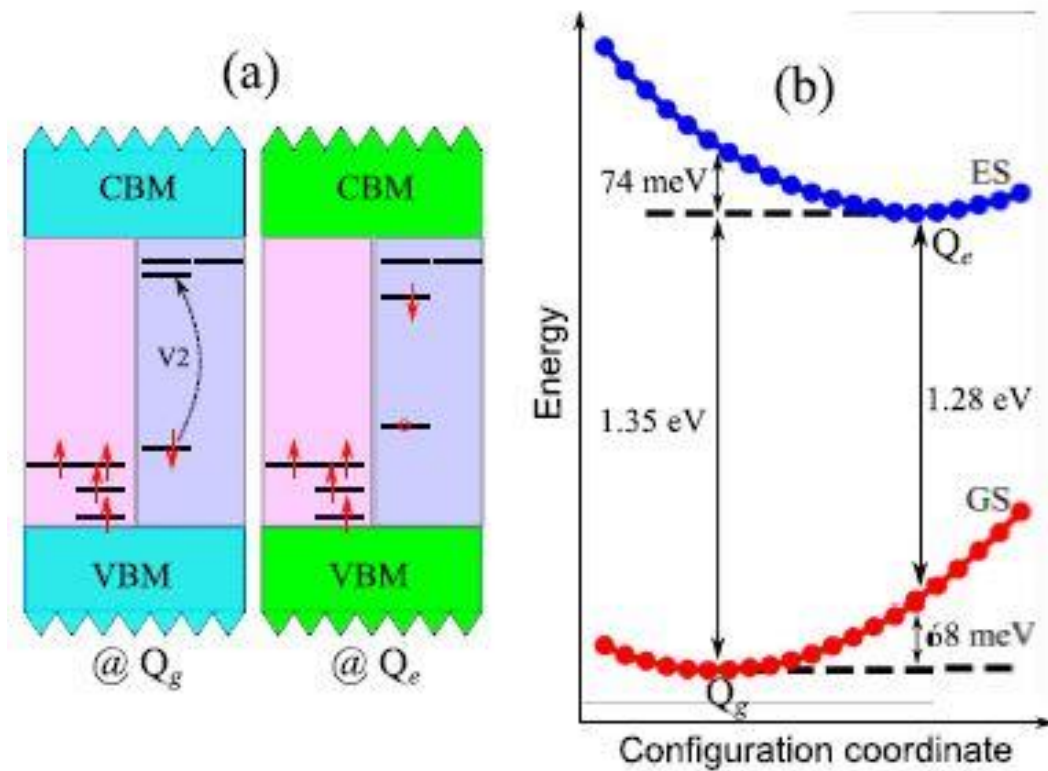


Figure 3.5. (a) The arrangement of electronic states before ( $Q_g$ ) and after ( $Q_e$ ) excitations calculated using HSE06 functional. The states (dark lines) filled by electrons represented by arrows for spin-up and -down. The hollow circle denotes hole. (b) A schematic configuration coordinate diagram for the GS and ES showing the energy scale for different transitions.

The defects can induce new vibrational modes, which are either resonant or antiresonant with vibrational modes of the host crystal. To map the vibrational modes on the same Brillouin zone as for the pristine SiC, the unfolded phonon dispersion curve is illustrated in Fig. 3.6(a). Results are that (i) the phonons between 20–40 meV and 90–110 meV are disturbed by the defects, but still follow the dispersion of the bands seen in the pristine system, and (ii) four localized vibrational modes (flat bands) appear at energies 73.45, 74.4, 111.47, and 112.8 meV. To find active phonons during the emission process, the electron-phonon spectral function is calculated as shown in Fig. 3.6(b). The calculation predicts that the PSB can be produced by a mix of about four phonon replicas: the double-degenerate Raman-active  $E_1$  mode with energy 31.3 meV, the M-point transverse acoustic phonon active at 35.3 meV, and two defect modes appearing at energies 73.45 and 74.4 meV, denoted as  $D_1$  and  $D_2$ , respectively. As illustrated in Fig

3.6(d), in  $D_1$  defect mode atoms up to second-nearest silicon neighbors from the vacancy center move, while for the  $D_2$  case, vibration is more intense and partially includes third-nearest silicon atoms.

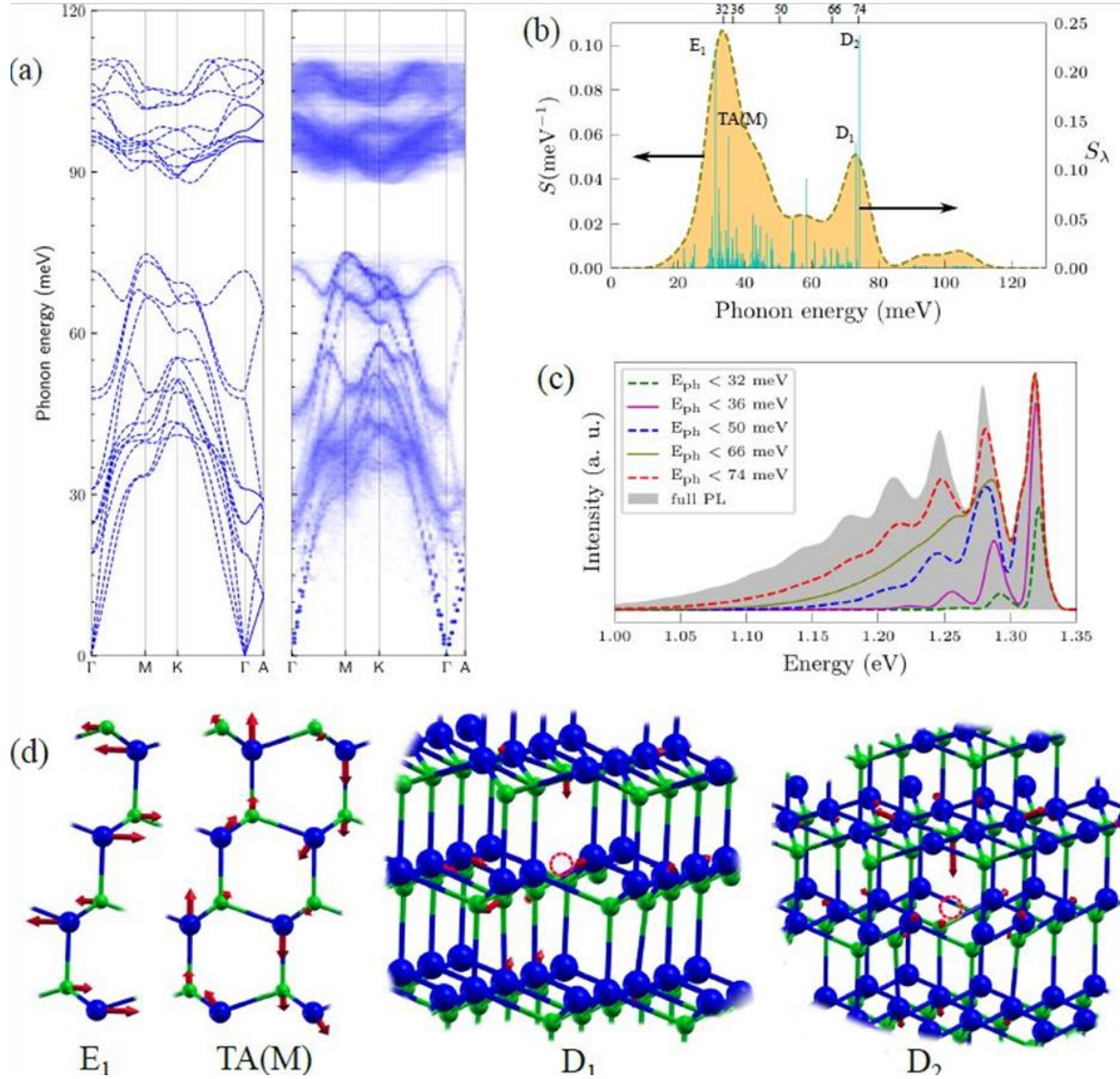


Figure 3.6 (a) Pristine SiC phonon dispersion curves and the unfolded phonon curves of defective SiC along high-symmetry directions. (b) Electron-phonon spectral function accompanied by partial Huang-Rhys factors. (c) The calculated partial PSB in the energy range of 1.0-3.5 eV. (d) Schematic representations of atomic displacements of  $E_1$ , TA(M),  $D_1$ , and  $D_2$  modes. Blue and green balls denote silicon and carbon atoms, respectively. Arrows are proportional to the displacements and come from the real part of the eigenvectors at the  $\Gamma$  point. The defect site is shown by a red circle.

The partial HR factor ( $S_\lambda$ ) is the average number of phonon  $\lambda$  emitted during an optical transition. The predicted total HR factor is  $S = 2.785$ , which corresponds to the average

number of phonons emitted during an optical transition. As a result, the weight of the ZPL (DW factor) defined by  $w_{\text{ZPL}} = e^{-S}$  is 6.17%, which is close to our measured value. As was illustrated in Fig. 3.4(a), the prediction for the PL line shape is in full agreement with the experiments. The PSB with seven peaks falls off at around 1.1 eV.

Following the analysis of vibrational modes, both bulk and defect phonons should contribute to the PSB. To get more insight into line shape, the partial PSB line shape is calculated. To this end, phonons up to a specific energy in  $S(\hbar\omega)$  are included. The phonon energy ( $E_{\text{ph}}$ ) is chosen based on the values of partial HR factors. In this way, the contribution of different phonons to the total line shape can be assessed. As seen in Fig. 3.6(c), the first peak shape is completed by adding phonons up to 50 meV, but it quickly vanishes at lower energies. In this range of energy, bulk phonons take place. The position of the first peak is at 36 meV lower than the ZPL, which is in agreement with the experiments. The comparison of the  $E_{\text{ph}} < 66$  meV and full PL curves indicates that a little more than half of the second phonon peak intensity at 1.275 eV (75 meV below the ZPL) arises from two-phonon or higher-order processes. Whereas, a little less than half of the peak intensity comes from one-phonon processes with  $E_{\text{ph}}$ . Furthermore, the defect-induced phonons at around 74 meV are crucial in shaping the second and higher phonon peaks of the optical emission spectrum at low temperature.

### 3.4 Discussion and conclusions

Though the DW factor of 40% and 30% was reported for the V1 and V2  $\text{V}_{\text{Si}}$  defects, respectively [101,120], the actual value is smaller due to the low detection efficiency at longer wavelengths of the PSB. We experimentally estimated the lower bound for the DW factor of 6%–9%. On the other hand, the calculations also yielded a DW factor of about 6%, which suggests that the real value is indeed in this range. Though this value is at least by a factor of 2 larger than that of the nitrogen vacancy defect in diamond [66]. The coupling of these spin defect centers to an optical resonator would be an alternative to realize quantum repeaters [121]. The vibrational energies of 37 and 36 meV from experiments and calculations, respectively, are also in close agreement. This is an important parameter, which determines at which temperature the phonon-assisted spin lattice relaxation mechanism associated with local vibrational modes is activated [65].

To summarize, we have investigated the local vibrational structure of the  $V_2 V_{Si}$  defect in a HPSI 4H-SiC wafer. The MW-assisted spectroscopy has enabled us to clearly separate the spectrally overlapped contribution from other intrinsic defects. We have found the resonant vibrational energy to be 36 meV, while the lower bound for the DW factor have been estimated to be 6%. We have applied DFT-based methodology to calculate and analyze the PL line shape. In addition, we have established that the contribution to the optical emission process is narrowed down to dominant bulk and defect-induced phonons. All together, the perfect agreement between the experimental data and the theoretical calculations shows that our approach can be applied to a large number of highly promising optically addressable spin qubits in all stable SiC polytypes, including vacancies, divacancies, and transition-metal color centers [122,123]. It is especially important when the spectral contribution of different defects overlaps and cannot otherwise be separated. The interaction of local vibrational modes with point defects allows us to understand the spin, optical, mechanical, and thermal properties of these defects. This is crucial for designing defect spins for quantum technologies.

# **Chapter 4 Microwave-assisted spectroscopy of vacancy-related spin centers in hexagonal SiC**

The results presented in this chapter were published in “Z. Shang, Y. Berencén, M. Hollenbach, S. Zhou, H. Kraus, T. Ohshima, and G. V. Astakhov, Microwave-assisted spectroscopy of vacancy-related spin centers in hexagonal SiC, *Phy. Rev. Appl.* 15, 034059 (2021)”. Zhen Shang, the thesis author, did all measurements.

In this chapter, spin resonant microwave-assisted spectroscopy is applied to investigate the optical and vibrational properties of silicon vacancies in 6H-SiC and divacancies in 4H- and 6H-SiC. We isolate spectral contributions of each type of defects, investigate their local vibrational modes and obtain the Debye-Waller factor.

## 4.1 Introduction

Since the NV center in diamond had emerged as an outstanding platform for solid-state quantum applications, single-point defects in wide-bandgap semiconductors have attracted a lot of interest [11-14,124]. Usually, these artificial atom-like defects possess a deep-energy level structure in the bandgap of the host material, which can result in a sub-bandgap light emission. Single-photon emission from single defects has been proved by the Hanbury Brown and Twiss experiments [22,90]. In addition, dangling bonds have been found to form optically controllable spin qubits [45,71,73]. Due to these properties, point defects in wide-bandgap semiconductors have been used to engineer single-photon emitters and spin qubits, allowing a variety of quantum applications such as quantum key distribution [125], quantum computing [107], quantum sensing of temperature, magnetic field [43,74,81], among others. The most studied point defects in SiC are the  $V_{Si}$  and VV (Fig. 4.1). According to previous reports [23,82,85], these two defects exhibit a modest single-photon emission rate, long spin coherence time and high spectral stability, which make them good candidates for quantum technologies. Additionally, the host material SiC, as a wide-bandgap group-IV semiconductor, has advantageous electrical, thermal, chemical and mechanical properties as well as advanced growth and device engineering protocols [126,127]. These advantages make spin qubits in SiC competitive prospects with other spin qubits in materials like diamond, for instance [124].

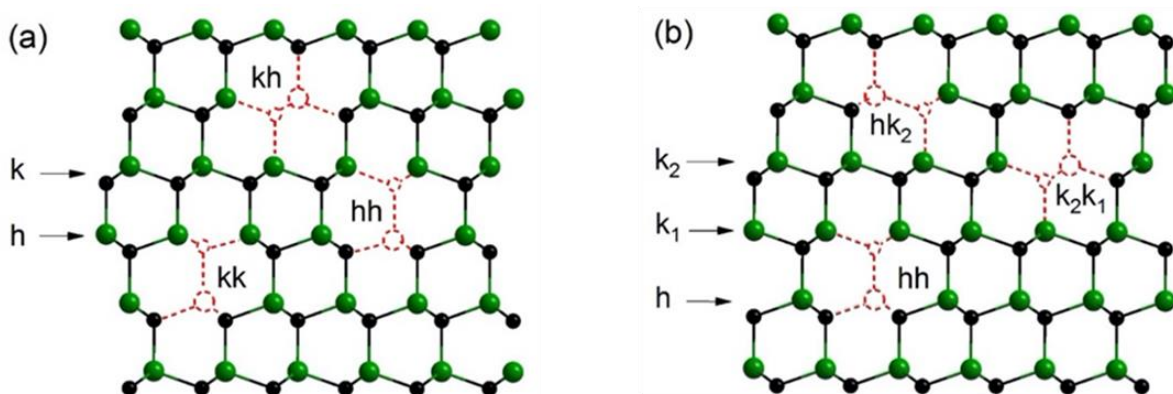


Figure 4.1. Schematic representation of the VV defects in 4H (a) and 6H (b) SiC. The cubic and hexagonal sites are labelled as k and h, respectively

Low-temperature PL has been widely used to spectrally identify point defects by inspecting the spectral position of the ZPL as well as to investigate their local vibrational structure [44,65,128]. The phonon energy and the DW factor can be deduced by the investigating of the local vibrational structure. However, there are only few reports on the local vibrational structure of point defects in SiC, and all of them are limited to the 4H-SiC polytype [129].

As spin-carrying defects,  $V_{Si}$  and VV have spin numbers of  $3/2$  and  $1$ , respectively, which split the ground state of  $V_{Si}$  and VV defects into two or three spin sublevels at zero magnetic field (Fig. 4.2 (a) and (b)). The zero field splitting (ZFS) is a fingerprint of each defect and can be detected by optically-detected magnetic resonance (ODMR) [130]. This spin property provides the opportunity to spectrally isolate the contribution of a certain defect by selecting a resonant microwave (MW) field [129].

In this chapter, we measure the  $V_{Si}$  and VV PL spectra in polytypes 4H- and 6H-SiC to identify the ZPL of each defect. Three VV defects in 4H-SiC and five VV defects in 6H-SiC corresponding to different combinations of cubic (k) and hexagonal (h) sites (Fig. 4.1) were detected [47]. Next, ODMR and MW-assisted spectroscopy are used to isolate the ZPL and PSB contributions of each defect. From the MW-assisted  $\Delta$ PL spectra, we can clearly determine the local vibrational energy and DW factors of all measured defects.



## 4.2 Experiment

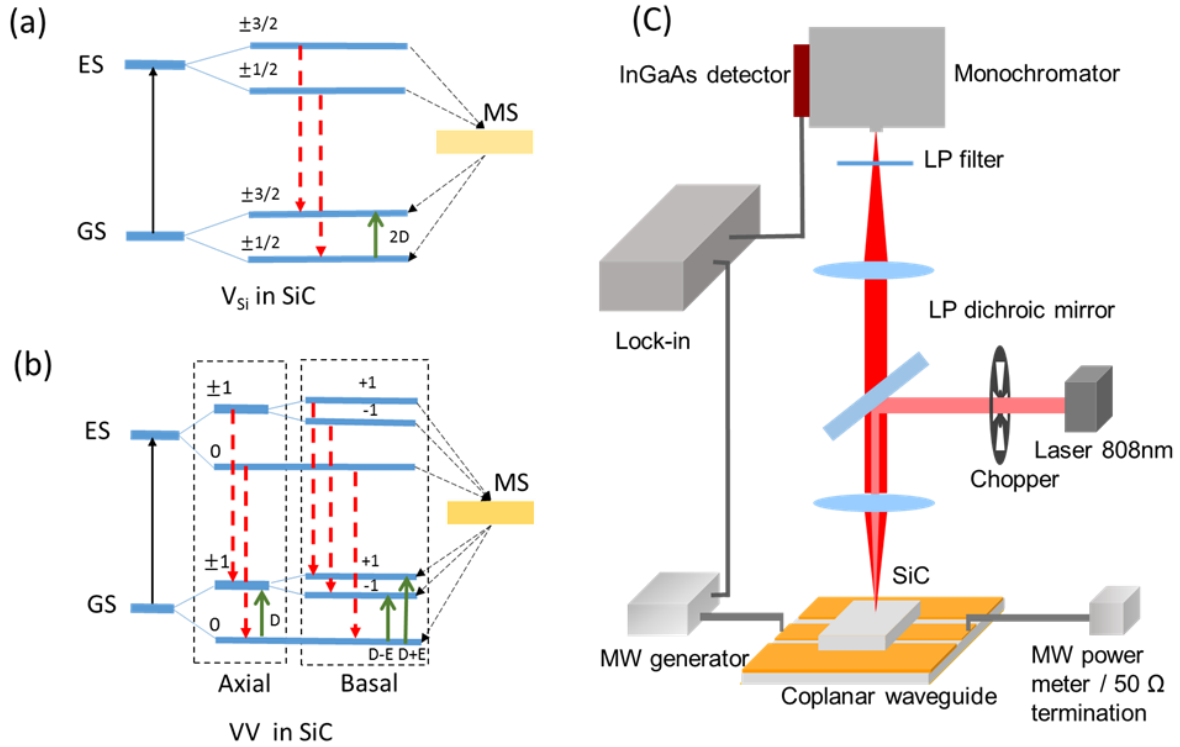


Figure 4.2 (a) and (b) Simplified schemes of the  $V_{Si}$  and  $VV$  optical pumping process, respectively. The defects are excited by an 808 nm laser, which is represented by a black arrow. The red dashed arrows represent the radiative recombination process. The black short dashed arrows indicate the spin-dependent relaxation process. The green arrows show spin transitions induced by the MW field. Because the basal and axial  $VV$  defects have different symmetry ( $C_{3v}$  and  $C_{1h}$ ), their zero field resonance structure is different. The left and right dashed boxes represent the spin resonance for the axial and basal  $VV$  defects spin at the MW frequencies  $D$  and  $D \pm E$ , respectively. (c) A scheme of our home-built MW-assisted spectroscopy setup.

The ODMR and MW-assisted spectroscopy measurements are performed in a home-built setup as shown in Fig. 4.2 (c). The sample is mounted on the cold finger of a closed-cycle cryostat. The temperature measured near the sample is 15K. An 808 nm laser is used to excite both the silicon vacancies and divacancies. The emitted PL signal from the sample is collected by a set of lenses and focused into a monochromator. An InGaAs detector and a built-in transimpedance amplifier are used to convert the PL intensity into a photovoltage, which is read out by a lock-in amplifier. For PL measurements, a chopper at 20 Hz modulates the excitation laser. Alternatively, we use a 940 nm laser to excite divacancies and the PL spectrum is recorded by an InGaAs

photo-diode array. For ODMR and MW-assisted spectroscopy measurements, the sample is placed on a coplanar waveguide in which the lock-in-modulated MW field propagates and induces spin resonance in the sample. The  $5 \text{ mm} \times 5 \text{ mm}$  4H-SiC sample under investigation was diced from a pristine high-purity semi-insulating wafer, which contains native  $V_{\text{Si}}$  and VV defects. The 6H-SiC samples were diced from a commercial 6H-SiC wafer (semi-insulating with resistivity above  $10^5 \Omega\cdot\text{cm}$  purchased from Sixon) possessing a size of  $5 \text{ mm} \times 3 \text{ mm}$ . Electron irradiation was performed in these 6H samples to create  $V_{\text{Si}}$  and VV defects with an energy of 1 MeV with fluences of  $10^{13}$ ,  $10^{14}$ ,  $10^{15}$ ,  $10^{16}$ ,  $10^{17}$  and  $10^{18} \text{ cm}^{-2}$ .

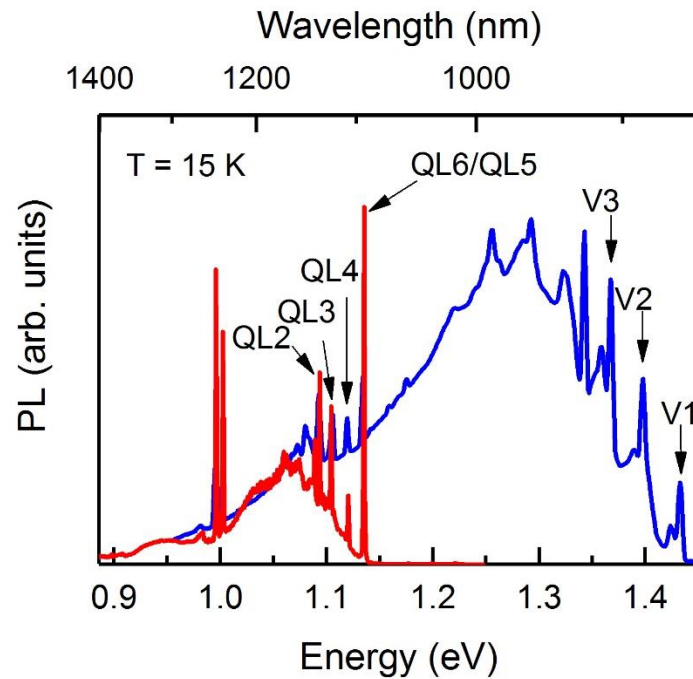


Figure 4.3 Low-temperature PL spectrum from the  $V_{\text{Si}}$  and the VV centers in 6H-SiC. The blue and red curves are measured with an 808 nm and 940 nm laser excitation, respectively. The QL5 and QL6 centers in 6H-SiC reveal a spectrally indistinguishable ZPL. The PL spectrum from  $V_{\text{Si}}$  and VV centers in 4H-SiC is shown in Fig. 1.4.4 (a).

Fig. 1.4.4 (a) and Fig. 4.3 represent typical PL spectra of vacancy-related defects in 4H- and 6H- SiC at 15K. In 4H-SiC, three ZPLs at 1078 nm, 1103 nm and 1130 nm corresponding to the so-called PL2, PL3 and PL4 defects are detected. As for the  $V_{\text{Si}}$  defects in 4H SiC, V1 and V2 have previously been investigated and thus they are not discussed here. In 6H-SiC, three  $V_{\text{Si}}$  ZPLs at 865 nm, 887 nm and 906 nm (labeled as

V1, V2 and V3 [130]) and four VV ZPLs at 1093 nm, 1108 nm, 1123 nm and 1135 nm (labeled as QL6- QL2 [47]) are detected, respectively. Several phonon replicas of the  $V_{Si}$  and VV defects are also obtained in this energy range.

From Fig. 1.4.4 (a) and Fig. 4.3, the overlapping contribution of ZPLs and phonon replicas are observed. For instance, the V3 ZPL superimposes on the V2's phonon replicas, making the calculation of the local vibrational energy of the V2 defect difficult. Another example is that the QL5 and QL6 centers have spectrally indistinguishable ZPLs, and hence the spectral properties of these two defects are inseparable through standard PL measurements. By changing the excitation wavelength from 808 nm to 940 nm, the contribution from the  $V_{Si}$  defects can be suppressed in conjunction with an enhancement of the signal from the VV defects (red curves in Fig. 4.3). However, the spectrally overlapped contributions from the different VV defects cannot be eliminated.

To separate the spectral contributions of different defect centers, MW-assisted spectroscopy is applied [129]. The optically excited  $V_{Si}$  and VV defects have two relaxation processes: the radiative recombination (red dash line in Fig. 4.2 (a), (b)) and the spin-dependent relaxation through metastable states (black short dash line in Fig. 4.2 (a), (b)). The spin Hamiltonian in zero magnetic field can be written in the form [17,46]:

$$H = D \left( S_z^2 - \left( \frac{1}{3} \right) [S(S + 1)] \right) + E(S_x^2 - S_y^2) \quad 4.1$$

Here, S is the spin number; D and E are zero field splitting parameters which are related to the crystal field and the symmetry of defects, respectively. If a MW field with an energy equal to the zero field splitting is applied, the spin population of the ground state spin sublevels changes and induces a measurable  $\Delta$ PL signal which can be recovered by lock-in amplification. The MW-assisted spectroscopy is based on the measurement of  $\Delta$ PL as a function of detection wavelength, where the sensitivity to one particular defect type is given by the frequency of the applied MW field. For the  $V_{Si}$  defects, the spin number is 3/2. The resonance frequency (i.e., the zero-field splitting) is equal to 2D (Fig. 4.2(a)). For the VV defects, the spin number is 1. Due to the hexagonal crystal structure, the VV defects have two kinds of symmetries,  $C_{3v}$  and  $C_{1v}$ . In Fig. 4.2(b), the left dash box represents the c-axis defects (PL2, QL1, QL2 and QL5), which have  $C_{3v}$  symmetry

with the zero-field resonant MW frequency equal to  $D$ . The right dashed box represents the basal defects (PL3, PL4, QL3, QL4, and QL6) which have lower symmetry  $C_{1v}$  with the zero-field resonant MW frequency given by  $D \pm E$ .

### 4.3 Experimental results

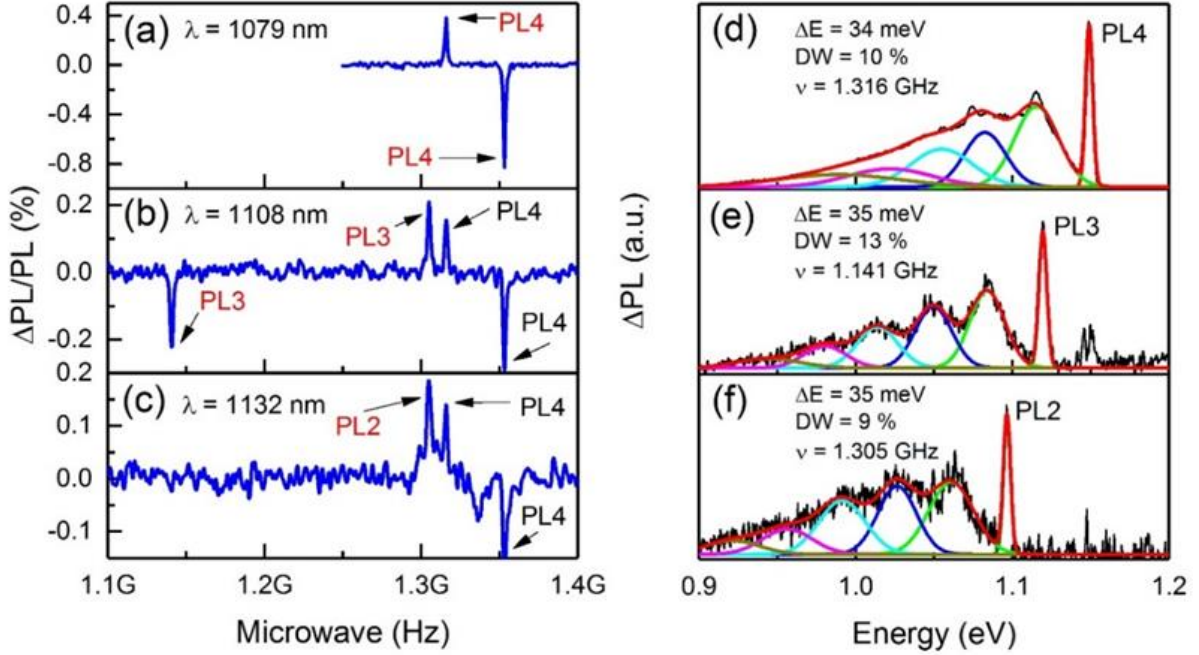


Figure 4.4 (a)-(c) ODMR spectra of the VV centers PL4, PL3 and PL2 in 4H-SiC. The peak position indicates the resonance frequency of a certain divacancy at zero magnetic field. For basal VV centers PL4 and PL3, there are two zero-field resonance frequencies corresponding to  $D \pm E$ . (d) - (f) Low-temperature MW-induced DPL spectrum under the resonance frequency. The ZPL, phonon energy ( $\Delta E$ ) and DW factor can be acquired directly from these spectra.

First, we performed ODMR measurements for each type of defect to determine the resonant MW frequency at 15 K. The results of the ODMR frequencies for all defects are summarized in Table 1. The ODMR contrast ( $\Delta\text{PL}/\text{PL}$ ) as a function of MW frequency is presented in Fig. 4.4 (a)-(c), Fig. 4.5 (a) and Fig. 4.6 (a)-(e) corresponding to  $V_{\text{Si}}$  defects in 6H-SiC and VV defects in 4H-SiC and 6H-SiC. The  $\Delta\text{PL}$  intensity is detected at the ZPL of each defect. For the VV defects in 4H-SiC, the resonant MW frequency is in the range of 1.0 - 1.4 GHz [40]. For QL2- QL6, the resonant MW frequency is in the range of 1.2 - 1.5 GHz [40]. For  $V_{\text{Si}}$  in 6H SiC, the resonant MW frequency associated to V2 and V3 is 128 MHz and 27 MHz, respectively [39]. All these values are listed in Table 1. The basal VV defects PL3, PL4 and QL4 have two resonant

MW frequencies corresponding to  $D \pm E$ . However, due to the low PL intensity, only one resonant MW frequency for the basal defect QL3 is obtained.

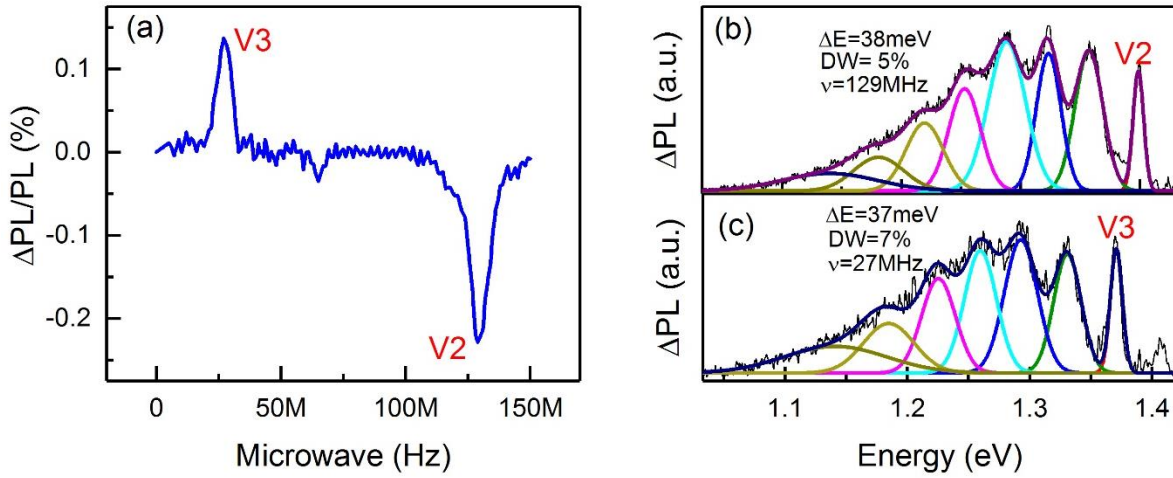


Figure 4.5 (a) ODMR spectrum of the V2 and V3 center in an electron irradiated 6H-SiC at a fluence of  $10^{17} \text{ cm}^{-2}$  at 100K. The peak position indicates the resonance frequency of 129 MHz and 27 MHz at zero magnetic field. (b), (c) Low-temperature MW-induced  $\Delta\text{PL}$  spectrum under the resonance frequency. The ZPL, phonon energy ( $\Delta E$ ) and DW factor can be acquired directly from this spectrum.

After determining the resonant frequencies, the MW-modulated  $\Delta\text{PL}$  is investigated for each defect. To increase the  $\Delta\text{PL}$  intensity, the monochromator slit is opened larger compared with the slit size used to perform the PL measurements. The somehow larger slit size decreases the spectral resolution but does not change the ratio of the ZPL to the PSB integral intensity. The experimental results are shown in Fig. 4.4(d)-(f) (PL2- PL4), Fig. 4.5 (b), (c) (V2 and V3) and Fig. 4.6 (f)-(j) (QL2- QL6). The spectral contributions of different centers can clearly be separated. Next, we use the Gauss multiple peak fitting to obtain the ZPL and phonon replicas. The separation between two adjacent phonon peaks gives the local vibrational energy  $\Delta E$ , which is shown in each figure. This implies that local vibrational modes of the  $V_{\text{Si}}$  and VV centers dominate the bulk phonons and can be characterized by a single phonon frequency. The real picture is more complex, but detailed theoretical calculations for the  $V_{\text{Si}}$  centers confirm that this is a good approximation [67]. The DW factors of all defects at 15 K fall between 5% and 17%, which are deduced by spectral integration, as shown in figures. The obtained  $\Delta E$  and DW factor are summarized in Table 1. We note that by determining the DW factor by



means of the MW-assisted spectroscopy, the spin-dependent variation of DW factor is neglected. This has been reported for the  $V_{Si}$  defects [67] and we assume the same for the divacancies.

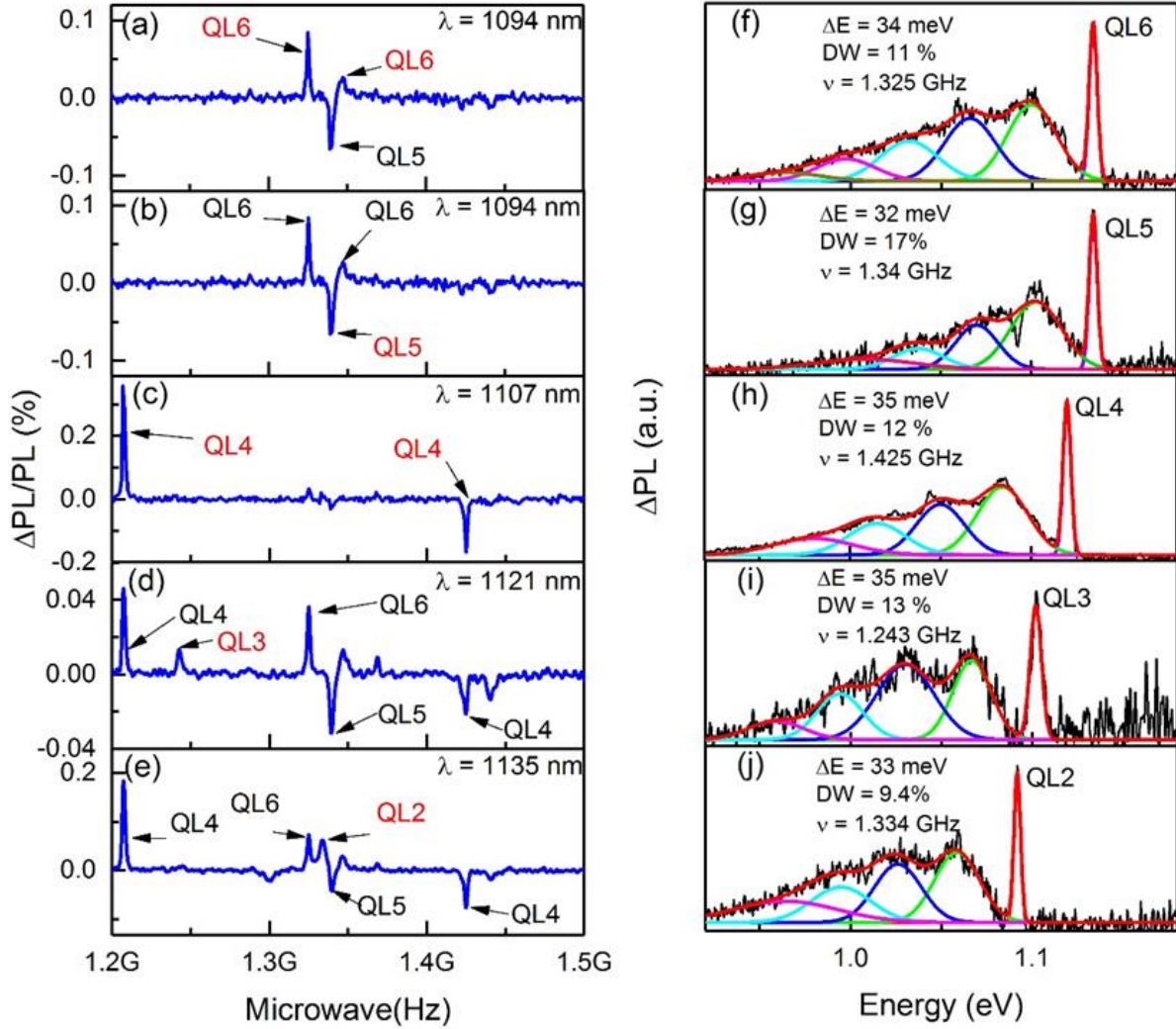


Figure 4.6(a)-(e) The ODMR spectra of divacancies QL2-QL6 in 6H-SiC. The peak position indicates the MW resonance frequency of a certain divacancy at zero magnetic field. For the basal VV, QL6 and QL4, there are two zero-field resonance frequencies D+E and D-E. (f)-(j) Low-temperature  $\Delta PL$  spectrum corresponding to QL2-QL6 in 6H-SiC. For each defect, the ZPL and PSBs emerge clearly. Because the zero-field splitting is individual for each divacancy, the  $\Delta PL$  spectrum contains information about the certain divacancy, whose ground state spin splitting is equal to the applied MW frequency. The local vibrational energy is obtained from two adjacent phonon peaks and the DW factor can be directly acquired from the  $\Delta PL$  spectrum.

Polytype	Spin centers	ZPL (eV)	ZFS (GHz)	$\Delta E$ (meV)	DW factor (%)	
$V_{Si}$	4H	V1	1.44	0.004	~38	8 [67]
		V2	1.35	0.070	37	6
	6H	V2	1.40	0.129	38	5
		V3	1.37	0.027	37	7
$VV$	4H	PL2	1.10	1.305	34	9
		PL3	1.12	1.141, 1.305	35	13
		PL4	1.15	1.316, 1.353	35	10
	6H	QL2	1.09	1.334	34	9
		QL3	1.10	1.243, 1.243 [47]	32	13
		QL4	1.12	1.425, 1.027	35	12
		QL5	1.13	1.340	35	17
		QL6	1.13	1.347, 1.325	33	11

Table 4.1 Summary of ZPL, ZFS,  $\Delta E$  and DW factor of  $V_{Si}$  and  $VV$  defects in 4H- and 6H-SiC.

We compared the two normalized MW-assisted  $\Delta PL$  spectra of QL4 as shown in Fig. 4.7(a). This figure shows that these two normalized MW-assisted  $\Delta PL$  spectra give the same phonon energy  $\Delta E$  and DW factor as expected. We then apply this approach to other defects. In Fig. 4.6 (a) and (b), the ODMR spectra show three resonant MW frequencies from the peak at 1.13 eV which are demonstrated to belong to the QL5 and QL6 defects [40]. It has been indicated that these two defects occupy the axis- and basal-oriented lattice sites (Fig. 4.1). However, it was not possible to unambiguously identify which one is basal-oriented because only one MW frequency was given for each of these defects, namely 1.340 GHz for QL5 and 1.347 GHz for QL6. In addition, the third resonant frequency was measured to be 1.325 GHz. To assign this resonant MW frequency to one of the aforementioned defects, we compared the normalized 1.325 GHz

MW-assisted  $\Delta$ PL spectra with the other two resonant frequency-assisted spectra and found that the 1.325 GHz and 1.347 GHz MW modulated spectra possess the same  $\Delta E$  and DW factor as shown in Fig. 4.7 (b). This indicates that the QL6 is a basal oriented-defect.

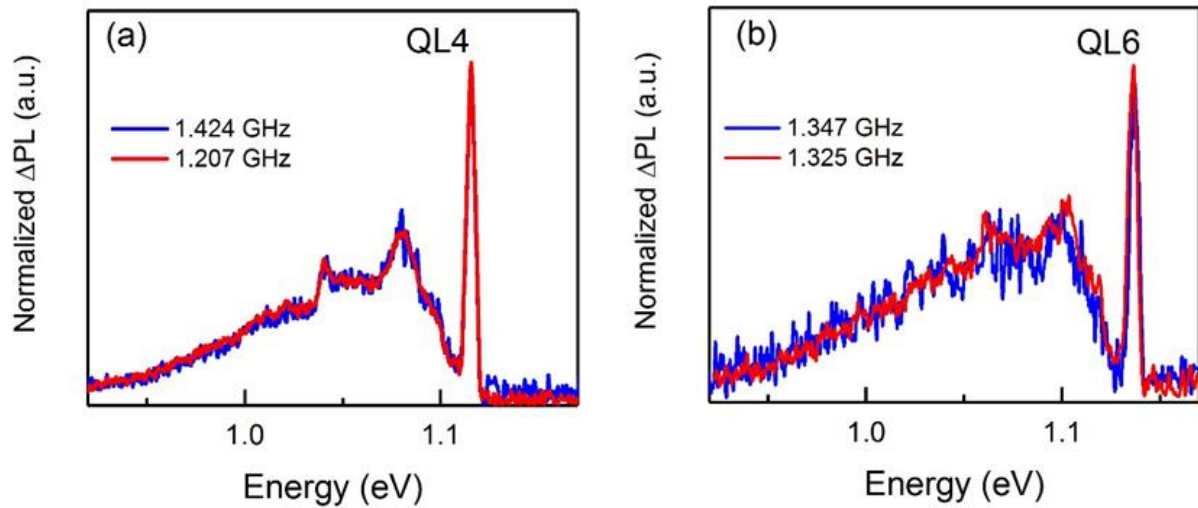


Figure 4.7 Normalized  $\Delta$ PL spectrum of basal divacancies QL4 (a) and QL 6 (b). Owing to the lower symmetry ( $C_{1h}$ ), there are two MW resonance frequencies corresponding to the GS zero-field spin transition energies  $D + E$  and  $D - E$ . The two different resonance frequencies give the same phonon energy and DW factor.



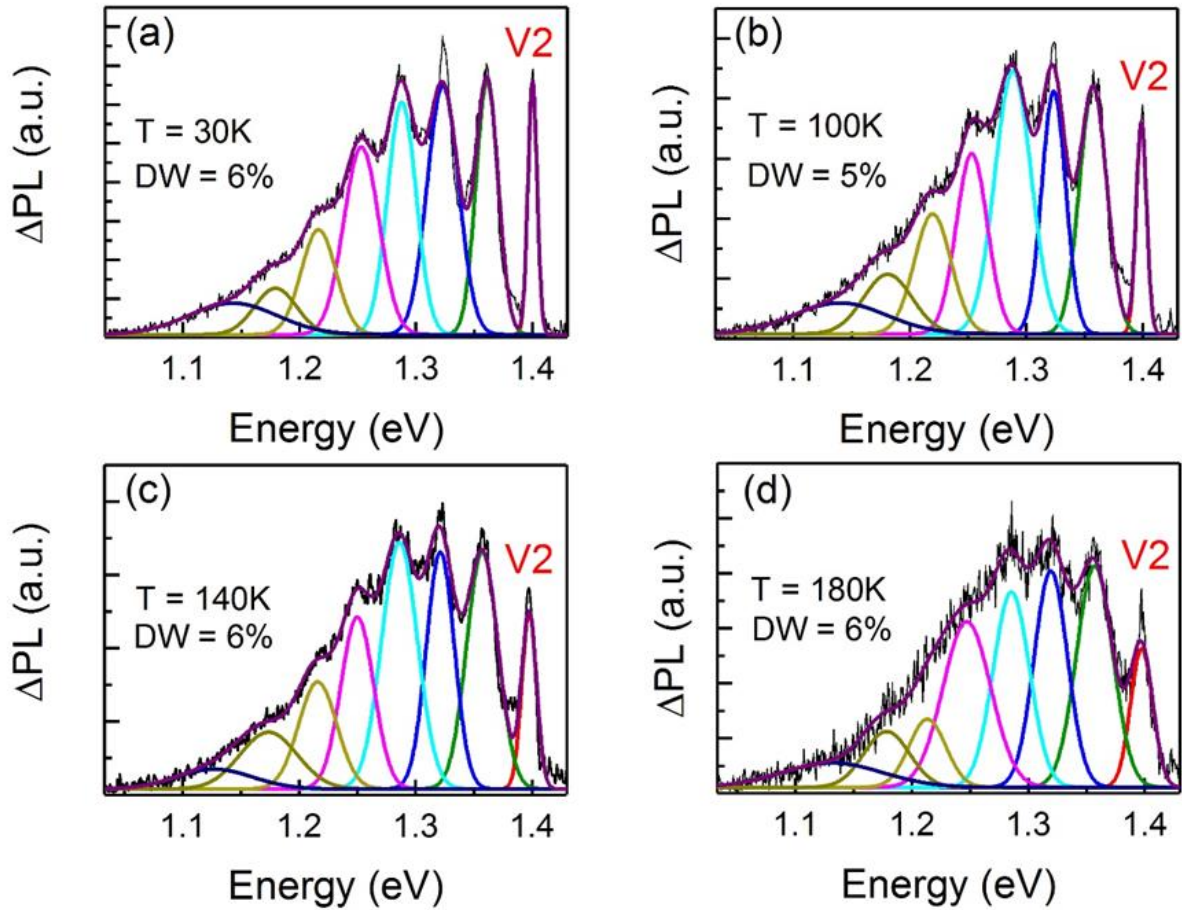


Figure 4.8  $\Delta$ PL spectrum of V2 from the  $10^{17} \text{ cm}^{-2}$  electron irradiated sample at 30K (a), 100K (b), 140K (c) and 180K (d). As the temperature increases, the ratio of ZPL intensity to the first phonon replica decreases, but the DW factor does not change appreciably.

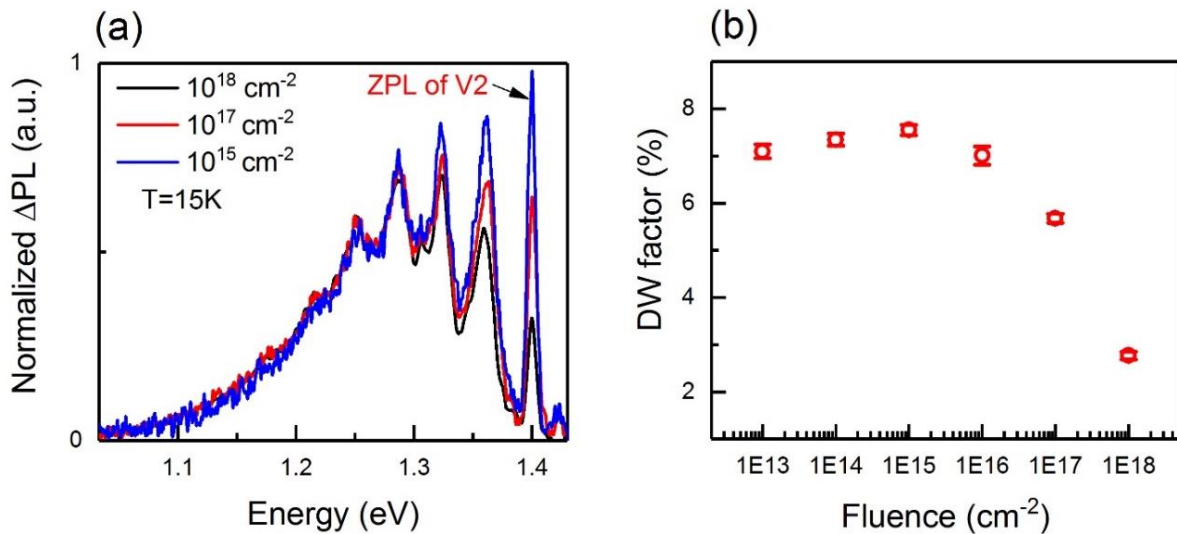


Figure 4.9 Normalized  $\Delta$ PL spectrum of V2 from three samples with irradiation fluence of  $10^{15}$ ,  $10^{17}$  and  $10^{18} \text{ cm}^{-2}$ . (b) DW factor as a function of fluence at 15K.

After obtaining the vibrational structure of  $V_{Si}$  and  $VV$ , we focus on the DW factor as a function of temperature and irradiation fluence of the  $V_2 V_{Si}$  defect in 6H-SiC. The results from the  $\Delta$ PPL spectra at 30 K, 100 K, 140 K and 180 K and the calculated DW factor of each spectrum are shown in Fig. 4.8 and Fig. 4.9. With increasing temperature, the relative amplitude of the ZPL decreases but the linewidth increases. This results in no clear changes in the DW factor. It indicates that the energy exchange between the lattice phonons and the local phonons does not change the ratio of the ZPL and the phonon replicas. The results from the normalized  $\Delta$ PPL intensity and the DW factor as a function of irradiation fluence at 15 K are depicted in Fig. 4.9. It is observed that the overall intensity of the ZPL decreases for the high-fluence irradiation sample (Fig. 4.9 (a)), whereas the DW factor decreases as the irradiation fluence increases (Fig. 4.9 (b)). High-fluence electron irradiation leads to crystal damage around the  $V_{Si}$  defects resulting in stronger interaction with local vibrations in the photon emission process.

#### 4.4 Conclusion

In summary, we have investigated the local vibrational structure of the  $V_{Si}$  defects and  $VV$  defects in 4H- and 6H-SiC. By MW-assisted spectroscopy, we successfully isolated the optically overlapped contributions of each defect. Using this approach, we have found the phonon energy and DW factor of all defects as summarized in Table 1. We have also verified that the MW-assisted spectra measured by different resonant frequencies associated with the same defect reveal the same vibrational states and DW factor. Furthermore, we have assigned some ODMR lines to certain defects, not reported before. From the study of the  $V_2 V_{Si}$  in 6H-SiC, we have found that the temperature does not have a clear influence on the DW factor, but high-fluence electron irradiation has shown to decrease the DW factor.

# **Chapter 5 Characterization of the polarization properties of $V_{Si}$ in 6H-SiC by PL and MW-assisted spectroscopy.**

Part of the results in this chapter are under preparation for publication “I. D. Breev, Z. Shang, A. V. Poshakinskiy, H. Singh, Y. Berencén, M. Hollenbach, S. S. Nagalyuk, E. N. Mokhov, R. A. Babunts, P. G. Baranov, D. Suter, M. Helm, S. A. Tarasenko, G. V. Astakhov, and A. N. Anisimov, Inverted fine structure of a 6H-SiC qubit enabling robust spin-photon interface, arXiv:2107.06989”.

In this chapter, two approaches are used: the MW-assisted spectroscopy and low temperature PL to measure the polarization properties of emission photons from  $V_{Si}$  in 6H-SiC. Both approaches give the same results. Therefore, MW-assisted spectroscopy holds promise for investigating the polarization properties of spin defects in wide bandgap semiconductors.

## 5.1 Introduction

Spin centers in SiC are considered as appealing candidates for the realization of quantum computing [18,19] and quantum networks [131]. Especially, the negatively charged  $V_{Si}$  centers in 4H- and 6H-SiC reveal promising quantum properties [70,71]. They have robust spin–photon interface [23], extremely long spin coherence time [65,78], high spectral stability of their ZPLs [88,101] and the well-developed nanoscale engineering technology [51,53]. These advantages pave the way for the on-demand generation of indistinguishable single-photon emitters. In chapter one, it has been explained that 4H-SiC has two non-equivalent lattice sites, resulting in two  $V_{Si}$  centers V1 and V2. Recent researches indicate that the ZPL of V1 dominates at low temperature. This low-temperature V1-ZPL is found to split into two lines V1 and V1' [44,120], which are orthogonally polarized. The V2-ZPL is linearly polarized along the c-axis [120], revealing that V2 emits preferentially perpendicular to the c-axis. As the SiC epitaxial layers are typically grown along the c-axis, the photon collection from the growth surface is less efficient. The  $V_{Si}$  centers in 6H-SiC have the similar quantum properties to those in 4H-SiC. However, the polarization properties of  $V_{Si}$  centers in 6H-SiC have not been investigated in detail. In previous chapters, the MW-assisted spectroscopy has been proved to be a powerful tool to spectrally isolate spin defects by their unique resonant MW frequencies. It has been used to determine the relative ratio of the PL emitted from different kind of spin defects, investigate the local vibrational structure of a specific spin defect, as well as to identify the symmetry of some special VV defects. This chapter deals with the use of MW-assisted spectroscopy to investigate the polarization properties of spin defects. The polarization properties of the  $V_{Si}$  centers in 6H-SiC are investigated systematically from PL spectra with no overlapping spectral contributions of other defects.

## 5.2 Experiment

The sample used in this chapter is a 6H-SiC bulk of  $2.3 \times 2.3 \times 1.15 \text{ mm}^3$  grown by physical vapor deposition with a concentration of dopants below  $1 \times 10^{17} \text{ cm}^{-3}$ . To create  $V_{\text{Si}}$  defects, electron irradiation with an energy of 2 MeV and a fluence of  $10^{18} \text{ cm}^{-2}$  was performed. All the measurements were carried out in our home-built setup, as described in chapter 2. For angular-dependence measurements, a commercial linear polarizer (LPNIRE2  $\times$  2, Thorlabs) mounted on a rotational mount was placed in front of the monochromator. The sample face, which is perpendicular to the c-axis is named as n-face; the other faces which are parallel to the c-axis are named as m-face. The experiments were performed at 300 K, 100 K and 15 K controlled by the temperature control system.

### Detection sensitivity calibration

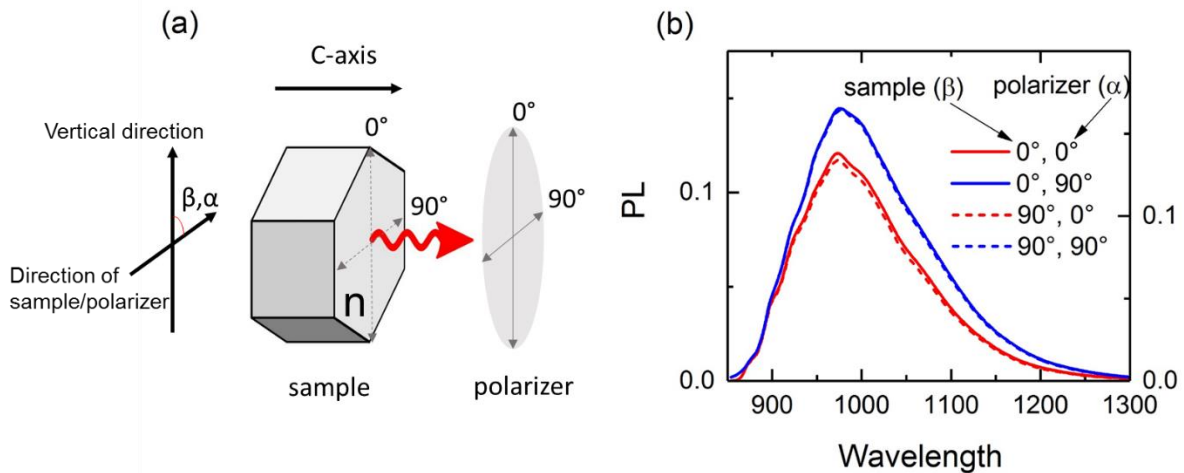


Figure 5.1 (a) Calibration of the angular-dependent detection sensitivity:  $\alpha$  is the angle between the polarizer direction and the vertical direction (the monochromator slit),  $\beta$  is the angle between the sample direction and vertical direction. (b) PL measurements for different  $\alpha$  and  $\beta$  at room temperature.

When the PL signal passes through optical components (such as the monochromator), there is a polarization-dependent intensity loss. Therefore, we perform the calibration of the angular-dependent detection sensitivity before the investigation of the polarization of light emission from  $V_{\text{Si}}$ . The method and results are shown in Fig. 5.1. The PL intensity  $I_{\text{meas}}$  of the unpolarized signal  $I_{\text{PL}}$  depends on the angle  $\alpha$  between the axis of

the linear polarizer and the certain direction (for instance, defined by the monochromator slit) as

$$I_{meas} = I_{PL}(1 + A - A\cos 2\alpha), \quad 5.1$$

Here,  $1+A$  is the correction factor due to the different sensitivity for  $\alpha = 0^\circ$  and  $\alpha = 90^\circ$ . To take into account the possible intrinsic PL polarization, we perform measurements for two sample orientations with  $\beta = 0^\circ$  and  $\beta = 90^\circ$  as presented in Fig. 5.1(b). The correction factor for different wavelengths ( $\lambda$ ) is obtained as

$$1 + 2A(\lambda) = \frac{I_{0^\circ,90^\circ}(\lambda) + I_{90^\circ,90^\circ}(\lambda)}{I_{0^\circ,0^\circ}(\lambda) + I_{90^\circ,0^\circ}(\lambda)}, \quad 5.2$$

Where  $I_{\beta,\alpha}(\lambda)$  is the PL intensity for the given orientations of the sample ( $\beta$ ) and polarizer ( $\alpha$ ) at a wavelength  $\lambda$ . To obtain the angular dependences of the PL signal  $I_{PL}(\alpha)$ , the measured intensities  $I_{meas}(\alpha)$  are corrected for each orientation using Eq. (5.1)

### **Two approaches to obtain polar plots at low temperature.**

There are two alternative approaches to obtain the polar plots of the  $V_{Si}$  in 6H-SiC. Here, we use V2 in 6H-SiC as an example to explain these two approaches. In the first approach, we use the MW-assisted spectroscopy, which allows separating overlapping contributions of different color centers as shown in Chapter 4. In Fig. 5.2 (a), we present a zoom-in of  $\Delta$ PPL spectrum of isolated V2 ZPL. The angular-dependence measurements of V2 in Fig. 5.2 (b) are directly obtained from the isolated ZPL of V2 at 15 K. In the second approach, we measure the ZPL intensity and subtract the PSB contributions from other centers. The polar plots of V2 measured by this approach from the m-face of sample is presented in Fig. 5.2 (d) as an example. Here, the angle  $\varphi_m$  is the angle between the polarizer direction and the c-axis. Both approaches give the same results.

Further validation of the second approach is presented in Fig. 5.2 (c) at  $T = 15$  K. In case V1, the  $ZPL_{V1}$  angular dependence can directly be obtained from the low-temperature PL spectra because there is no contribution from V2 and V3 (Fig. 5.2 (c)). The PL intensity at the V2-ZPL includes two contributions, the V2-ZPL and the V1-PSB

$$ZPL_{V2} = PL_{at\ ZPL_{V2}} - PSB_{V1\ at\ ZPL_{V2}}. \quad 5.3$$

We assume that the ratio  $a = \text{ZPL}/\text{PSB}$  is polarization independent and Eq. (5.3) can be rewritten as

$$ZPL_{V2} = PL_{at\ ZPL_{V2}} - aZPL_{V1}. \quad 5.4$$

The parameter  $a$  is obtained from the PL spectrum at  $\varphi_m = 90^\circ$ , when the contribution from the V2-ZPL is negligible (Fig. 5.2 (c) red curve). The V2 angular dependence before and after the PSB subtraction is shown in Fig. 5.2 (d). Similarly, the PL intensity from the V3-ZPL includes three contributions, the V3-ZPL, the V1-PSB and the V2-PSB, which can be written as

$$ZPL_{V3} = PL_{at\ ZPL_{V3}} - bZPL_{V1} - cZPL_{V2}. \quad 5.5$$

The parameters  $b$  and  $c$  are obtained from the PL spectra of Fig. 5.2 (c) at  $\varphi_m = 90^\circ$  and  $0^\circ$  (red and blue curves), respectively.

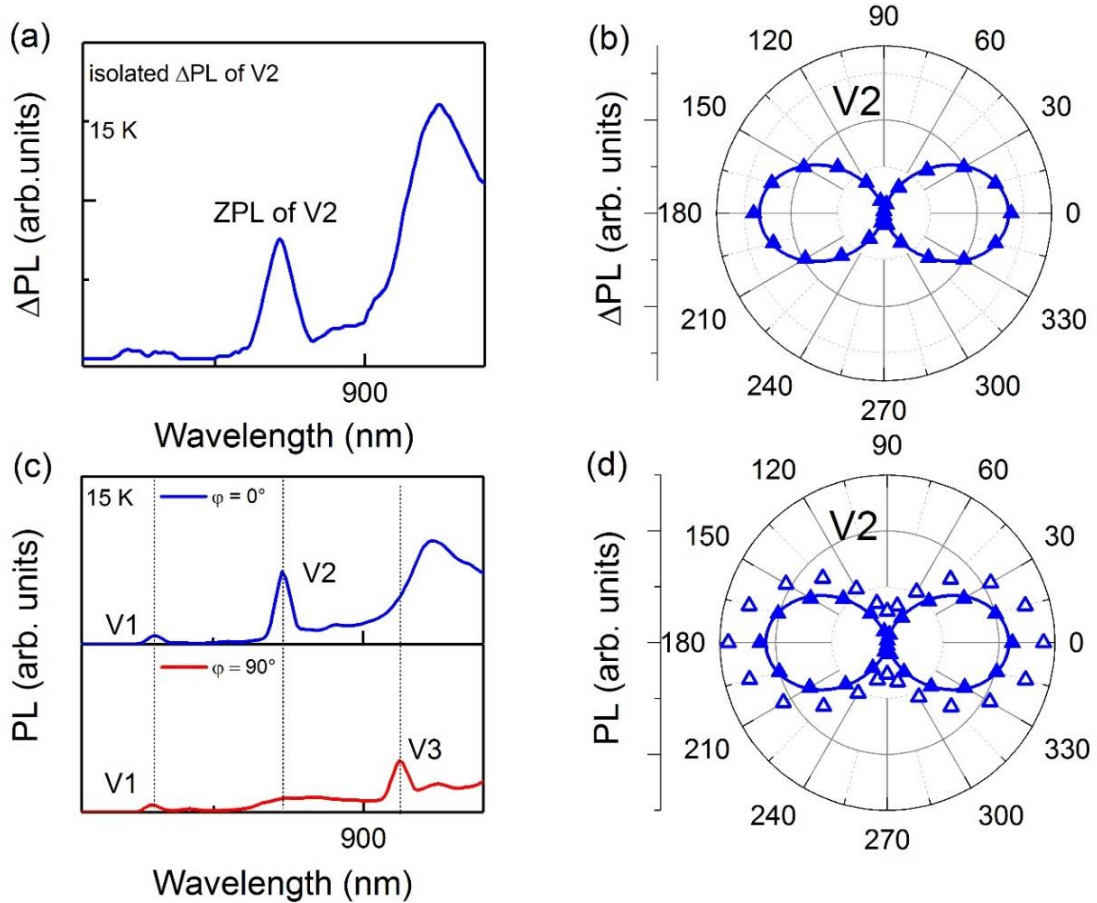


Figure 5.2 (a) Isolated  $\Delta\text{PL}$  spectrum of ZPL of V2 at 15 K. (b) V2 polar plots obtained from the MW-assisted spectroscopy. (c) PL spectra of V1, V2 and V3 ZPLs from the m-face at 15 K. (d) V2 polar plots obtained from the PL measurements. The open symbols represent the PL

intensity at the wavelength of the corresponding ZPL. The solid symbols are the values after the PSB subtraction. The solid lines are the fitting results.

### 5.3 Experimental results

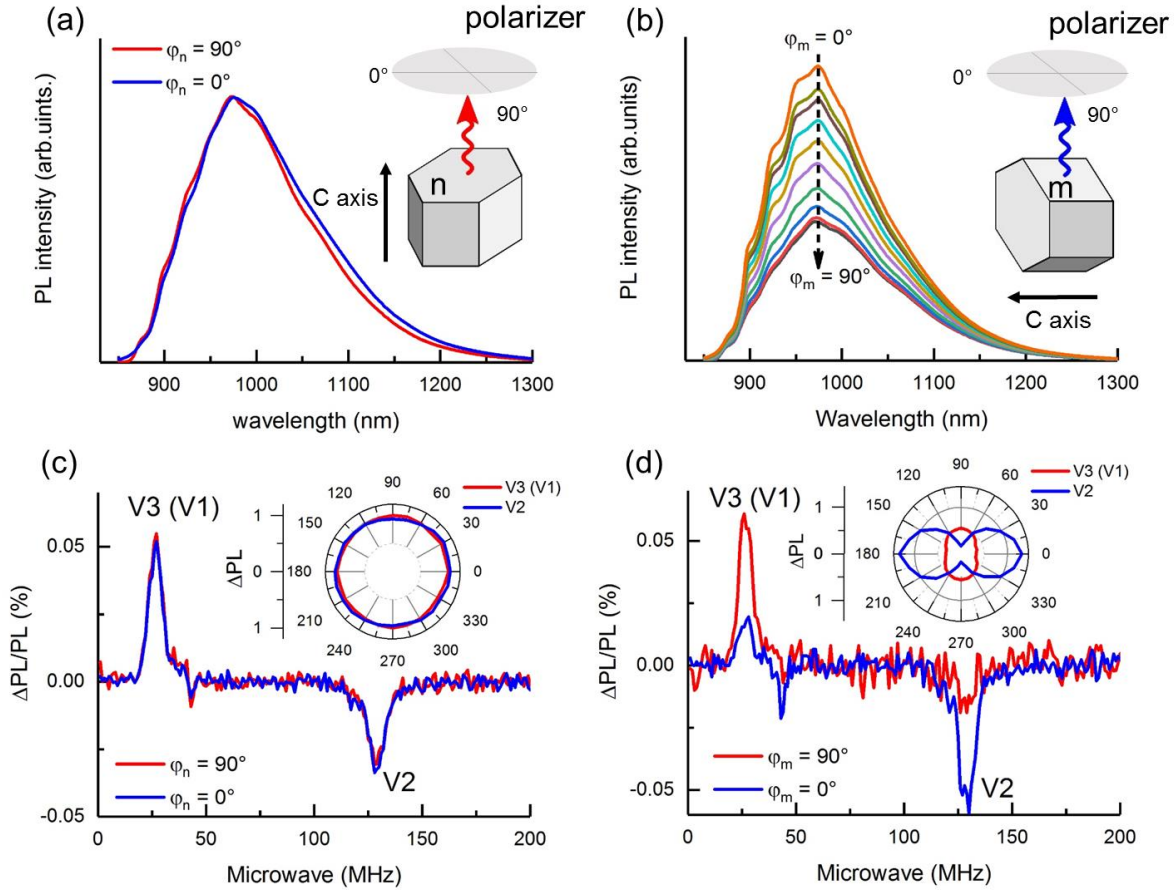


Figure 5.3 (a) and (b) Room-temperature PL measurement from the n-face (perpendicular to the c-axis) and m-face (parallel to the c-axis), respectively. The insets present the relation between the signal-collected-face and polarizer orientation. (c) and (d) Room-temperature ODMR measurement of the V1/V3 and V2 centers at two angles of the polarizer. In m-face,  $\phi_m$  is the angle between the polarizer direction and c-axis; in n-face,  $\phi_n$  is the angle between the polarizer orientation and any reference direction.

Fig. 5.3 (a) and (b) present the room-temperature PL spectra measured from n- and m-face. The light collected from n-face is unpolarized, but the light collected from m-face is partially polarized along the c-axis. However, due to the PL spectra including three contributions from V1, V2 and V3, we cannot just obtain the polarization properties from the room-temperature PL measurements. Therefore, the ODMR and the MW-assisted spectroscopy are used to spectrally separated V1, V2 and V3 centers as shown



in Fig. 5.3 (c) and (d). ODMR spectra present the resonant frequencies at 27 MHz and 128 MHz corresponding to V2 and V1/V3. MW-assisted spectroscopy gives similar results with the PL spectra for the n-face. For the m-face, MW-assisted spectroscopy can separate V2 by its resonant frequency and thus to obtain strong E||c polarization. However, because V1 and V3 have the same resonant frequency [47], the polarization of the V1/V3 cannot be separated at room temperature.

Hence, the low-temperature PL and MW-assisted spectroscopy of V1, V2 and V3 on m-face is measured at 100 K. The results of two experimental approaches are shown in Fig. 5.4. All the results are fitted by the function:

$$I(\varphi) = I_0(1 + \cos(2\theta) \cos(2\varphi)). \quad 5.6$$

Where  $I(\varphi)$  is the intensity of PL or  $\Delta$ PL,  $I_0$  and  $\cos(2\theta)$  are fitting parameters,  $\varphi$  is the angle between the c-axis and the direction of the polarizer.

By both approaches, we find that V2 ZPL has nearly 100% E||c-axis polarization. The fit to Eq. 5.6 gives  $\cos(2\theta) = 0.97$  ( $\theta \approx 0^\circ$ ). V3-ZPL has a relatively E $\perp$ c polarization ( $\cos(2\theta) = -0.89$ ,  $\theta \approx 90^\circ$ ). As for V1, due to the weak ODMR contrast, the PL can only obtain the polar plot after subtracting the background. The result in Fig. 5.4 (d) indicates the V1-ZPL is unpolarized ( $\cos(2\theta) = 0.01$ ,  $\theta \approx 90^\circ$ ). To verify that the temperature and the polarization of the excitation laser have no contribution to the polarization properties, we characterized the polarization of the excitation laser (Fig. 5.5) and repeated the measurements at 15 K with two laser orientations (solid and open symbols in Fig. 5.6 b-d). The observed angular dependencies are not related to the thermal population in the excited state or the polarization of the excitation laser as expected.

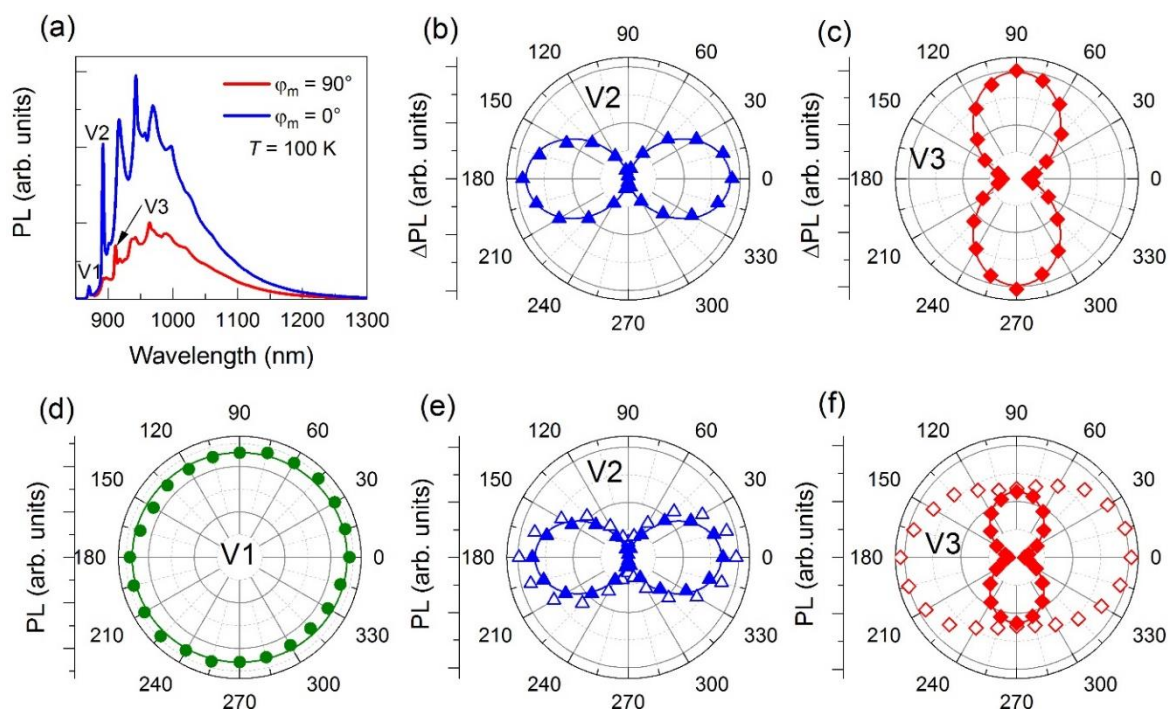


Figure 5.4 (a) PL spectra measured from m-face at  $T = 100$  K. (b) and (c) polar plots of V2 and V3 at 100 K measured by MW-assisted spectroscopy. (d), (d) and (f) Polar plots of V1, V2 and V3 at 100 K measured by PL spectra with PSB contributions subtraction. The open symbols represent the PL intensity at the wavelength of the corresponding ZPL. The solid symbols are the values after the PSB subtraction. The solid lines are the fitting results.

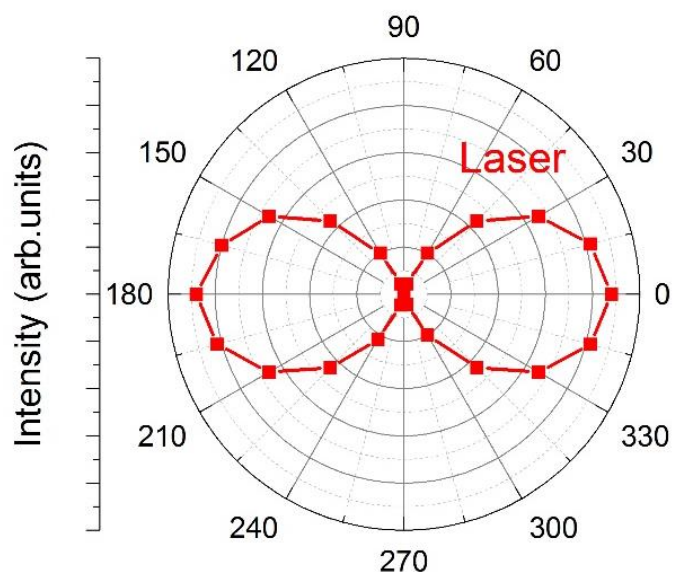


Figure 5.5 Polar plots of the excitation laser.  $0^\circ$  corresponds to the vertical direction.

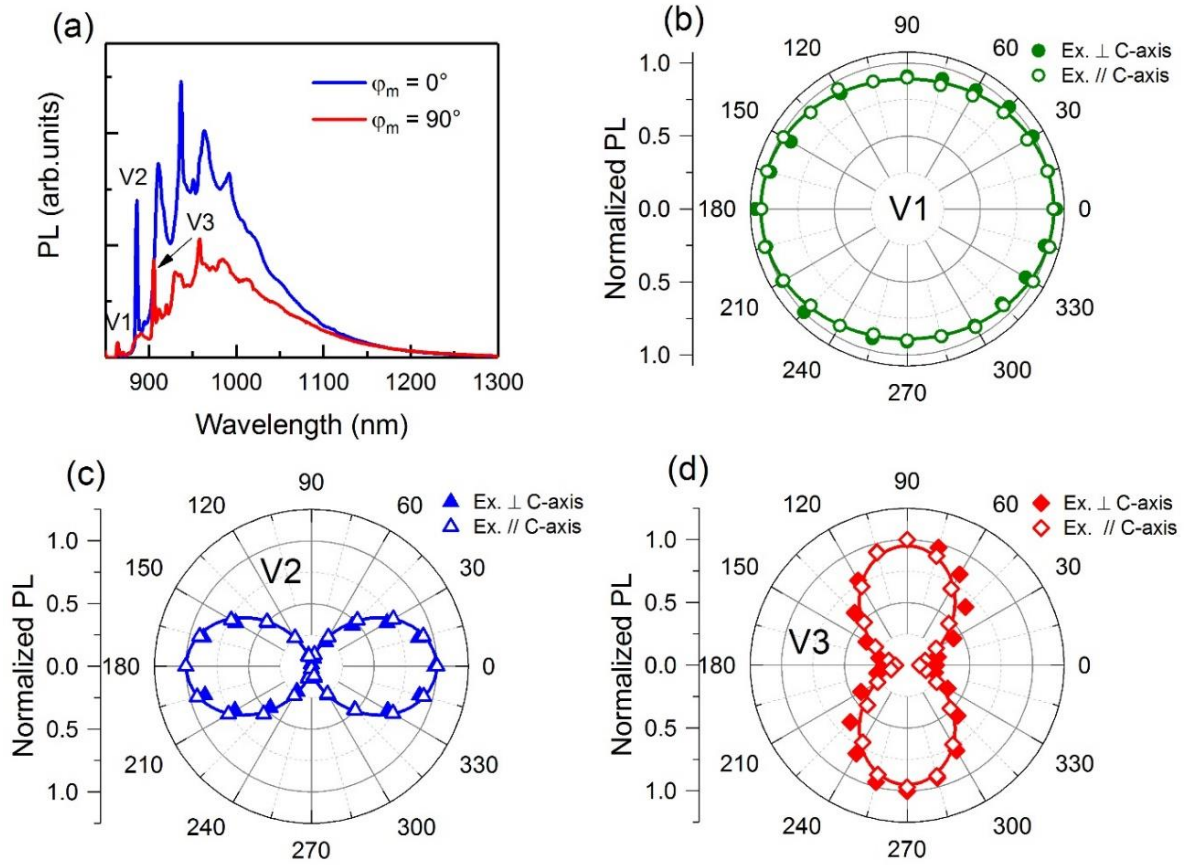


Figure 5.6 (a) PL spectra measured from m-face at  $T = 15$  K. (b), (c) and (d) Polar plots of V1, V2 and V3, respectively, at 15 K. The solid symbols are measurements with the laser polarization perpendicular to the c-axis. The open symbols are measurements with the laser polarization parallel to the c-axis.

## 5.4 Conclusion

In this chapter, two approaches have been used to investigate the polarization properties of photons emitted from  $V_{Si}$  in 6H-SiC. In particular, MW-assisted spectroscopy is used for the first time to investigate the polarization on spin defects. The results show that the V3 center in 6H-SiC emits preferentially along the c-axis, making the photon extraction more efficient and the integration into photonic structures technologically easier.

# Chapter 6 Summary and outlook

## Summary

To summarize this entire thesis, MW-assisted spectroscopy has been proposed as a promising approach to investigate the optical properties of  $V_{Si}$  and VV spin defects in 4H- and 6H-SiC. The MW-assisted spectroscopy has enabled to separate the spectrally overlapped contribution of different types of defects. From a PL spectrum containing no overlapping spectral contributions of other defects, the local vibrational mode of all measured  $V_{Si}$  and VV in 4H- and 6H-SiC has been found along with the phonon energy and DW factor. The interaction of local vibrational modes with point defects has allowed to understand the spin, optical, mechanical, and thermal properties of these defects. In the investigation of V2 in 4H-SiC, a perfect agreement between the experimental data and theoretical calculation have been obtained. The MW-assisted spectra measured at different resonant frequencies associated with the same defect have been found to reveal the same vibrational mode and DW factor. Furthermore, some new ODMR lines to certain defects have been assigned, which have never been reported before. From the investigation of the V2  $V_{Si}$  in 6H-SiC, it has been found that the temperature does not have a clear influence on the DW factor, but high-fluence electron irradiation has been shown to decrease the DW factor. In the polarization investigation, it has been found that in 6H-SiC, V1 possesses no polarization, V2 shows a strong  $E||c$ -axis polarization, while V3 exhibits a strong  $E \perp c$ -axis polarization. It has also been demonstrated that the temperature and the orientation of the excitation laser have no influence on the photon polarization. In short, this thesis has demonstrated that MW-assisted spectroscopy is a powerful technique to investigate a large number of spin defects in wide-bandgap semiconducting materials.

## Outlook

MW-assisted spectroscopy has been demonstrated to be a promising technique to investigate the local vibrational structure and polarization properties of spin defects. Both properties play significant roles in the characterization of spin defects for quantum applications. Some other spin defects in wide-bandgap semiconducting materials and

2D materials have similar spin and optical properties, which means that the approach used in this thesis holds promise for the characterization of these defects. Hence, the MW-assisted spectroscopy can be widely applied in the investigation of these spin defects in the years to come. With the help of MW-assisted spectroscopy, two important aspects in quantum technology can be addressed. First, a single-photon source with a high DW factor can be selected from all the potential candidates. The high ZPL emission could benefit the generation rate of spin-photon entanglement and make a great difference in quantum repeater and long distance quantum network. The second aspect that could be tackled is to find the optimal single-photon source with polarized indistinguishable single photons, which could be used in quantum key distribution, for instance.

# Bibliography

- [1] F. Arute, et al., Quantum supremacy using a programmable superconducting processor, *Nature* **574**, 505 (2019).
- [2] H.-S. Zhong, H. Wang, Y.-H. Deng, M.-C. Chen, L.-C. Peng, Y.-H. Luo, J. Qin, D. Wu, X. Ding, Y. Hu, P. Hu, X.-Y. Yang, W.-J. Zhang, H. Li, Y. Li, X. Jiang, L. Gan, G. Yang, L. You, Z. Wang, L. Li, N.-L. Liu, C.-Y. Lu, and J.-W. Pan, Quantum computational advantage using photons, *Science* **370**, 1460 (2020).
- [3] R. P. Feynman., Simulating physics with computers, *Int. J. Theor. Phys.* **21**, 467 (1982).
- [4] A. Montanaro, Quantum algorithms: an overview, *npj Quantum Inf.* **2**, 15023 (2016).
- [5] T. D. Ladd, F. Jelezko, R. Laflamme, Y. Nakamura, C. Monroe, and J. L. O'Brien, Quantum computers, *Nature* **464**, 45 (2010).
- [6] E. Knill, R. Lalamme, and G. J. Milburn, A scheme for efficient quantum computation with linear optics, *Nature* **409**, 46 (2001).
- [7] R. Blatt and D. Wineland, Entangled states of trapped atomic ions, *Nature* **453**, 1008 (2008).
- [8] I. Buluta, S. Ashhab, and F. Nori, Natural and artificial atoms for quantum computation, *Rep. Prog. Phys.* **74**, 104401 (2011).
- [9] R. Barends, J. Kelly, A. Megrant, A. Veitia, D. Sank, E. Jeffrey, T. C. White, J. Mutus, A. G. Fowler, B. Campbell, Y. Chen, Z. Chen, B. Chiaro, A. Dunsworth, C. Neill, P. O'Malley, P. Roushan, A. Vainsencher, J. Wenner, A. N. Korotkov, A. N. Cleland, and J. M. Martinis, Superconducting quantum circuits at the surface code threshold for fault tolerance, *Nature* **508**, 500 (2014).
- [10] D. Bera, L. Qian, T.-K. Tseng, and P. H. Holloway, Quantum Dots and Their Multimodal Applications: A Review, *Materials* **3**, 2260 (2010).
- [11] M. W. Doherty, N. B. Manson, P. Delaney, F. Jelezko, J. Wrachtrup, and L. C. L. Hollenberg, The nitrogen-vacancy colour centre in diamond, *Phys. Rep.* **528**, 1 (2013).

- [12] S. Castelletto and A. Boretti, Silicon carbide color centers for quantum applications, *J. Phys. Photonics*. **2**, 022001 (2020).
- [13] A. Lohrmann, B. C. Johnson, J. C. McCallum, and S. Castelletto, A review on single photon sources in silicon carbide, *Rep. Prog. Phys.* **80**, 034502 (2017).
- [14] S. E. Economou and P. Dev, Spin-photon entanglement interfaces in silicon carbide defect centers, *Nanotechnology* **27**, 504001 (2016).
- [15] A. Gruber, A. Dräbenstedt, C. Tietz, L. Fleury, J. Wrachtrup, and C. v. Borczyskowski, Scanning confocal optical microscopy and magnetic resonance on single defect centers, *Science* **276**, 2012 (1997).
- [16] M. Hollenbach, Y. Berencen, U. Kentsch, M. Helm, and G. V. Astakhov, Engineering telecom single-photon emitters in silicon for scalable quantum photonics, *Opt. Express* **28**, 26111 (2020).
- [17] H. Kraus, V. A. Soltamov, D. Riedel, S. Vāth, F. Fuchs, A. Sperlich, P. G. Baranov, V. Dyakonov, and G. V. Astakhov, Room-temperature quantum microwave emitters based on spin defects in silicon carbide, *Nat. Phys.* **10**, 157 (2014).
- [18] L. Gordon, J. R. Weber, J. B. Varley, A. Janotti, D. D. Awschalom, and C. G. Van de Walle, Quantum computing with defects, *MRS Bulletin* **38**, 802 (2013).
- [19] J. R. Weber, W. F. Koehl, J. B. Varley, A. Janotti, B. B. Buckley, C. G. Van de Walle, and D. D. Awschalom, Defects in SiC for quantum computing, *J. Appl. Phys.* **109**, 102417 (2011).
- [20] W. F. Koehl, B. B. Buckley, F. J. Heremans, G. Calusine, and D. D. Awschalom, Room temperature coherent control of defect spin qubits in silicon carbide, *Nature* **479**, 84 (2011).
- [21] H. J. von Bardeleben, J. L. Cantin, A. Csóré, A. Gali, E. Rauls, and U. Gerstmann, NV centers in  ${}^3\text{C}$ ,  ${}^4\text{H}$ , and  ${}^6\text{H}$  silicon carbide: A variable platform for solid-state qubits and nanosensors, *Phys. Rev. B* **94**, 121202(R) (2016).
- [22] S. Castelletto, B. C. Johnson, V. Ivády, N. Stavrias, T. Umeda, A. Gali, and T. Ohshima, A silicon carbide room-temperature single-photon source, *Nat. Mater.* **13**, 151 (2014).
- [23] R. Nagy, M. Niethammer, M. Widmann, Y. C. Chen, P. Udvarhelyi, C. Bonato, J. U. Hassan, R. Karhu, I. G. Ivanov, N. T. Son, J. R. Maze, T. Ohshima, O. O. Soykal,

- A. Gali, S. Y. Lee, F. Kaiser, and J. Wrachtrup, High-fidelity spin and optical control of single silicon-vacancy centres in silicon carbide, *Nat. Commun.* **10**, 1954 (2019).
- [24] C. J. Cochrane, J. Blacksberg, M. A. Anders, and P. M. Lenahan, Vectorized magnetometer for space applications using electrical readout of atomic scale defects in silicon carbide, *Sci. Rep.* **6**, 37077 (2016).
- [25] T. Kimoto and A. Cooper, *Fundamentals of Silicon Carbide Technology: Growth, Characterization, Devices, and Applications*, John Wiley & Sons Singapore Pte. Ltd, (2014).
- [26] V. A. Izhevskiy, L. A. Genova, J. C. Bressiani, and A. H. A. Bressiani, Review article: silicon carbide. Structure, properties and processing, *Cerâmica* **46**, 4 (2000).
- [27] L. L. Snead, T. Nozawa, Y. Kato, T.-S. Byun, S. Kondo, and D. A. Petti, Handbook of SiC properties for fuel performance modeling, *J. Nucl. Mater.* **371**, 329 (2007).
- [28] J. J. Berzelius, Untersuchungen über die flussspathsäure und deren merkwürdigsten Verbindungen *Ann. Phys. Chem. Lpz.* **1**, 169 (1824).
- [29] M. Bhatnagar and B. J. Baliga, Comparison of 6H-SiC, 3C-SiC, and Si for Power Devices, *IEEE Trans. Electron Devices* **40**, 645 (1993).
- [30] R. M. Potter, J. M. Blank, and A. Addamiano, Silicon Carbide Light - Emitting Diodes, *J. Appl. Phys.* **40**, 2253 (1969).
- [31] IOFFE database semiconductors on NSM: <http://www.ioffe.ru/SVA/NSM/Semicond>.
- [32] G. Chikvaidze, N. Mironova-Ulmane, A. Plaude, and O. Sergeev, Investigation of Silicon Carbide Polytypes by Raman Spectroscopy, *Latv. J. Phys. Tech. Sci.* **51**, 51 (2014).
- [33] O. Kordina, C. Hallin, A. Ellison, A. S. Bakin, I. G. Ivanov, A. Henry, R. Yakimova, M. Touminen, A. Vehanen, and E. Janzén, High temperature chemical vapor deposition of SiC, *Appl. Phys. Lett.* **69**, 1456 (1996).
- [34] E. G. Acheson, Production of artificial crystalline carbonaceous materials, carborundum. English Patent 17911 (1892).



- [35] Y. M. Tairov and V. F. Tsvetkov, General principles of growing large-size single crystals of various silicon carbide polytypes, *J. Cryst. Growth* **52**, 146 (1981).
- [36] D. Elwell and H. J. Scheel, *Crystal growth from high-temperature solutions*, Academic Press, (1975).
- [37] P. J. Wellmann, Review of SiC crystal growth technology, *Semicond. Sci. Technol.* **33**, 103001 (2018).
- [38] G. Wolfowicz, C. P. Anderson, B. Diler, O. G. Poluektov, F. J. Heremans, and D. D. Awschalom, Vadium spin qubits as telecom quantum emitters in silicon carbide.pdf, *Sci. Adv.* **6**, eaaz1192 (2020).
- [39] V. Ivady, J. Davidsson, N. Deegan, A. L. Falk, P. V. Klimov, S. J. Whiteley, S. O. Hruszkewycz, M. V. Holt, F. J. Heremans, N. T. Son, D. D. Awschalom, I. A. Abrikosov, and A. Gali, Stabilization of point-defect spin qubits by quantum wells, *Nat. Commun.* **10**, 5607 (2019).
- [40] F. Fuchs, B. Stender, M. Trupke, D. Simin, J. Pflaum, V. Dyakonov, and G. V. Astakhov, Engineering near-infrared single-photon emitters with optically active spins in ultrapure silicon carbide, *Nat. Commun.* **6**, 7578 (2015).
- [41] P. Udvarhelyi, R. Nagy, F. Kaiser, S.-Y. Lee, J. Wrachtrup, and A. Gali, Spectrally Stable Defect Qubits with no Inversion Symmetry for Robust Spin-To-Photon Interface, *Phys. Rev. Appl.* **11**, 044022 (2019).
- [42] E. Sörman, N. Son, W. Chen, O. Kordina, C. Hallin, and E. Janzén, Silicon vacancy related defect in 4H and 6H SiC, *Phys. Rev. B* **61**, 2613 (2000).
- [43] H. Kraus, V. A. Soltamov, F. Fuchs, D. Simin, A. Sperlich, P. G. Baranov, G. V. Astakhov, and V. Dyakonov, Magnetic field and temperature sensing with atomic-scale spin defects in silicon carbide, *Sci. Rep.* **4**, 5303 (2014).
- [44] M. Wagner, B. Magnusson, W. M. Chen, E. Janzén, E. Sörman, C. Hallin, and J. L. Lindström, Electronic structure of the neutral silicon vacancy in 4H and 6H SiC, *Phys. Rev. B* **62**, 16555 (2000).
- [45] D. J. Christle, A. L. Falk, P. Andrich, P. V. Klimov, J. U. Hassan, N. T. Son, E. Janzen, T. Ohshima, and D. D. Awschalom, Isolated electron spins in silicon carbide with millisecond coherence times, *Nat. Mater.* **14**, 160 (2015).

- [46] G. Balasubramanian, I. Y. Chan, R. Kolesov, M. Al-Hmoud, J. Tisler, C. Shin, C. Kim, A. Wojcik, P. R. Hemmer, A. Krueger, T. Hanke, A. Leitenstorfer, R. Bratschitsch, F. Jelezko, and J. Wrachtrup, Nanoscale imaging magnetometry with diamond spins under ambient conditions, *Nature* **455**, 648 (2008).
- [47] A. L. Falk, B. B. Buckley, G. Calusine, W. F. Koehl, V. V. Dobrovitski, A. Politi, C. A. Zorman, P. X. Feng, and D. D. Awschalom, Polytype control of spin qubits in silicon carbide, *Nat. Commun.* **4**, 1819 (2013).
- [48] Y. C. Chen, P. S. Salter, M. Niethammer, M. Widmann, F. Kaiser, R. Nagy, N. Morioka, C. Babin, J. Erlekampf, P. Berwian, M. J. Booth, and J. Wrachtrup, Laser Writing of Scalable Single Color Centers in Silicon Carbide, *Nano. Lett.* **19**, 2377 (2019).
- [49] P. G. Baranov, V. A. Soltamov, A. A. Soltamova, G. V. Astakhov, and V. D. Dyakonov, Point Defects in SiC as a Promising Basis for Single-Defect, Single-Photon Spectroscopy with Room Temperature Controllable Quantum States, *Materials Science Forum* **740-742**, 425 (2013).
- [50] C. Kasper, D. Klenkert, Z. Shang, D. Simin, A. Gottscholl, A. Sperlich, H. Kraus, C. Schneider, S. Zhou, M. Trupke, W. Kada, T. Ohshima, V. Dyakonov, and G. V. Astakhov, Influence of Irradiation on Defect Spin Coherence in Silicon Carbide, *Phys. Rev. Appl.* **13**, 044054 (2020).
- [51] J. Wang, X. Zhang, Y. Zhou, K. Li, Z. Wang, P. Peddibhotla, F. Liu, S. Bauerdick, A. Rudzinski, Z. Liu, and W. Gao, Scalable Fabrication of Single Silicon Vacancy Defect Arrays in Silicon Carbide Using Focused Ion Beam, *ACS Photonics* **4**, 1054 (2017).
- [52] H. J. v. Bardeleben, J. L. Cantin, L. Henry, and M. F. Barthe, Vacancy defects in p-type 6H-SiC created by low-energy electron irradiation, *Phys. Rev. B* **62**, 10841 (2000).
- [53] H. Kraus, D. Simin, C. Kasper, Y. Suda, S. Kawabata, W. Kada, T. Honda, Y. Hijikata, T. Ohshima, V. Dyakonov, and G. V. Astakhov, Three-Dimensional Proton Beam Writing of Optically Active Coherent Vacancy Spins in Silicon Carbide, *Nano. Lett.* **17**, 2865 (2017).

- [54] J. Wang, Y. Zhou, X. Zhang, F. Liu, Y. Li, K. Li, Z. Liu, G. Wang, and W. Gao, Efficient Generation of an Array of Single Silicon-Vacancy Defects in Silicon Carbide, *Phys. Rev Appl* **7**, 064021 (2017).
- [55] R. Averback and T. D. d. l. Rubia, Displacement Damage in Irradiated Metals and Semiconductors, *Solid State Phys.* **51**, 281 (1997).
- [56] H. L. Heinisch, L. R. Greenwood, W. J. Weber, and R. E. Williford, Displacement damage in silicon carbide irradiated in fission reactors, *J. Nucl. Mater.* **327**, 175 (2004).
- [57] J.-F. Wang, Q. Li, F.-F. Yan, H. Liu, G.-P. Guo, W.-P. Zhang, X. Zhou, L.-P. Guo, Z.-H. Lin, J.-M. Cui, X.-Y. Xu, J.-S. Xu, C.-F. Li, and G.-C. Guo, On-Demand Generation of Single Silicon Vacancy Defects in Silicon Carbide, *ACS Photonics* **6**, 1736 (2019).
- [58] J. F. Ziegler, M. D. Ziegler, and J. P. Biersack, SRIM – The stopping and range of ions in matter (2010), *Nucl. Instrum. Methods Phys. Res. B* **268**, 1818 (2010).
- [59] N. Iwamoto, A. Azarov, T. Ohshima, A. M. M. Moe, and B. G. Svensson, High temperature annealing effects on deep-level defects in a high purity semi-insulating 4H-SiC substrate, *J. Appl. Phys.* **118**, 045705 (2015).
- [60] Q. Li, J.-F. Wang, F.-F. Yan, J.-Y. Zhou, H.-F. Wang, H. Liu, L.-P. Guo, X. Zhou, A. Gali, Z.-H. Liu, Z.-Q. Wang, K. Sun, G.-P. Guo, J.-S. Tang, J.-S. Xu, C.-F. Li, and G.-C. Guo, Room temperature coherent manipulation of single-spin qubits in silicon carbide with high readout contrast, arXiv:2005.07876v1.
- [61] F. Seitz, An interpretation of crystal luminescence, *Trans. Faraday Soc.* **35**, 74 (1939).
- [62] A. N. Alias, Y. Yaacob, Z. M. Zabidi, S. H. N. Alshuridin, and N. A. Aini, General description of configurational coordinate model and kinetic of luminescence, *J. Fundam. Appl. Sci.* **9**, 568 (2018).
- [63] M. Lax, The Franck - Condon Principle and Its Application to Crystals, *J. Chem. Phys.* **20**, 1752 (1952).
- [64] M. A. Omary and H. H. Patterson, Luminescence Theory, in *Encyclopedia of spectroscopy and spectrometry*, edited by J. C. Lindon, G. E. Tranter, and D. W. Koppenaal Elsevier, Academic Press, (2010).

- [65] D. Simin, H. Kraus, A. Sperlich, T. Ohshima, G. V. Astakhov, and V. Dyakonov, Locking of electron spin coherence above 20 ms in natural silicon carbide, *Phys. Rev. B* **95**, 161201(R) (2017).
- [66] A. Alkauskas, B. B. Buckley, D. D. Awschalom, and C. G. Van de Walle, First-principles theory of the luminescence lineshape for the triplet transition in diamond NV centres, *New J. Phys.* **16**, 073026 (2014).
- [67] P. Udvarhelyi, G. Thiering, N. Morioka, C. Babin, F. Kaiser, D. Lukin, T. Ohshima, J. Ul-Hassan, N. T. Son, J. Vučković, J. Wrachtrup, and A. Gali, Vibronic States and Their Effect on the Temperature and Strain Dependence of Silicon-Vacancy Qubits in 4H-SiC, *Phys. Rev. Appl.* **13**, 054017 (2020).
- [68] H. Kraus, Optically detected magnetic resonance on organic and inorganic carbon-based semiconductors, Ph.D. Thesis, Julius-Maximilians Universität Würzburg (2014).
- [69] Manuscript of Model SR830 DSP Lock-In Amplifier, supported by SRS Stanford Research Systems, Revision 2.5 (10/2011).
- [70] P. G. Baranov, A. P. Bundakova, A. A. Soltamova, S. B. Orlinskii, I. V. Borovykh, R. Zondervan, R. Verberk, and J. Schmidt, Silicon vacancy in SiC as a promising quantum system for single-defect and single-photon spectroscopy, *Phys. Rev. B* **83**, 125203 (2011).
- [71] D. Riedel, F. Fuchs, H. Kraus, S. Vath, A. Sperlich, V. Dyakonov, A. A. Soltamova, P. G. Baranov, V. A. Ilyin, and G. V. Astakhov, Resonant addressing and manipulation of silicon vacancy qubits in silicon carbide, *Phys. Rev. Lett.* **109**, 226402 (2012).
- [72] V. A. Soltamov, A. A. Soltamova, P. G. Baranov, and Proskuryakov, II, Room temperature coherent spin alignment of silicon vacancies in 4H- and 6H-SiC, *Phys. Rev. Lett.* **108**, 226402 (2012).
- [73] M. Widmann, S. Y. Lee, T. Rendler, N. T. Son, H. Fedder, S. Paik, L. P. Yang, N. Zhao, S. Yang, I. Booker, A. Denisenko, M. Jamali, S. A. Momenzadeh, I. Gerhardt, T. Ohshima, A. Gali, E. Janzen, and J. Wrachtrup, Coherent control of single spins in silicon carbide at room temperature, *Nat. Mater.* **14**, 164 (2015).

- [74] D. Simin, F. Fuchs, H. Kraus, A. Sperlich, P. G. Baranov, G. V. Astakhov, and V. Dyakonov, High-Precision Angle-Resolved Magnetometry with Uniaxial Quantum Centers in Silicon Carbide, *Phys. Rev. Appl.* **4**, 014009 (2015).
- [75] D. Simin, V. A. Soltamov, A. V. Poshakinskiy, A. N. Anisimov, R. A. Babunts, D. O. Tolmachev, E. N. Mokhov, M. Trupke, S. A. Tarasenko, A. Sperlich, P. G. Baranov, V. Dyakonov, and G. V. Astakhov, All-Optical dc Nanotesla Magnetometry Using Silicon Vacancy Fine Structure in Isotopically Purified Silicon Carbide, *Phys. Rev. X* **6**, 031014 (2016).
- [76] M. Niethammer, M. Widmann, S.-Y. Lee, P. Stenberg, O. Kordina, T. Ohshima, N. T. Son, E. Janzén, and J. Wrachtrup, Vector Magnetometry Using Silicon Vacancies in 4H-SiC Under Ambient Conditions, *Phys. Rev. Appl.* **6**, 034001 (2016).
- [77] Ö. O. Soykal and T. L. Reinecke, Quantum metrology with a single spin-3/2 defect in silicon carbide, *Phys. Rev. B* **95**, 081405(R) (2017).
- [78] V. A. Soltamov, C. Kasper, A. V. Poshakinskiy, A. N. Anisimov, E. N. Mokhov, A. Sperlich, S. A. Tarasenko, P. G. Baranov, G. V. Astakhov, and V. Dyakonov, Excitation and coherent control of spin qubit modes in silicon carbide at room temperature, *Nat. Commun.* **10**, 1678 (2019).
- [79] G. Wolfowicz, C. P. Anderson, S. J. Whiteley, and D. D. Awschalom, Heterodyne detection of radio-frequency electric fields using point defects in silicon carbide, *Appl. Phys. Lett.* **115**, 043105 (2019).
- [80] A. N. Anisimov, D. Simin, V. A. Soltamov, S. P. Lebedev, P. G. Baranov, G. V. Astakhov, and V. Dyakonov, Optical thermometry based on level anticrossing in silicon carbide, *Sci. Rep.* **6**, 33301 (2016).
- [81] Y. Zhou, J. Wang, X. Zhang, K. Li, J. Cai, and W. Gao, Self-Protected Thermometry with Infrared Photons and Defect Spins in Silicon Carbide, *Phys. Rev. Appl.* **8**, 044015 (2017).
- [82] L.-P. Yang, C. Burk, M. Widmann, S.-Y. Lee, J. Wrachtrup, and N. Zhao, Electron spin decoherence in silicon carbide nuclear spin bath, *Phys. Rev. B* **90**, 241203(R) (2014).

- [83] S. G. Carter, Ö. O. Soykal, P. Dev, S. E. Economou, and E. R. Glaser, Spin coherence and echo modulation of the silicon vacancy in 4H-SiC at room temperature, *Phys. Rev. B* **92**, 161202(R) (2015).
- [84] H. Seo, A. L. Falk, P. V. Klimov, K. C. Miao, G. Galli, and D. D. Awschalom, Quantum decoherence dynamics of divacancy spins in silicon carbide, *Nat. Commun.* **7**, 12935 (2016).
- [85] J. S. Embley, J. S. Colton, K. G. Miller, M. A. Morris, M. Meehan, S. L. Crossen, B. D. Weaver, E. R. Glaser, and S. G. Carter, Electron spin coherence of silicon vacancies in proton-irradiated 4H-SiC, *Phys. Rev. B* **95**, 045206 (2017).
- [86] M. Fischer, A. Sperlich, H. Kraus, T. Ohshima, G. V. Astakhov, and V. Dyakonov, Highly Efficient Optical Pumping of Spin Defects in Silicon Carbide for Stimulated Microwave Emission, *Phys. Rev. Appl.* **9**, 054006 (2018).
- [87] D. J. Christle, P. V. Klimov, C. F. de las Casas, K. Szász, V. Ivády, V. Jokubavicius, J. Ul Hassan, M. Syväjärvi, W. F. Koehl, T. Ohshima, N. T. Son, E. Janzén, Á. Gali, and D. D. Awschalom, Isolated Spin Qubits in SiC with a High-Fidelity Infrared Spin-to-Photon Interface, *Phys. Rev. X* **7**, 021046 (2017).
- [88] N. Morioka, C. Babin, R. Nagy, I. Gediz, E. Hesselmeier, D. Liu, M. Joliffe, M. Niethammer, D. Dasari, V. Vorobyov, R. Kolesov, R. Stohr, J. Ul-Hassan, N. T. Son, T. Ohshima, P. Udvarhelyi, G. Thiering, A. Gali, J. Wrachtrup, and F. Kaiser, Spin-controlled generation of indistinguishable and distinguishable photons from silicon vacancy centres in silicon carbide, *Nat. Commun.* **11**, 2516 (2020).
- [89] F. Fuchs, V. A. Soltamov, S. Vath, P. G. Baranov, E. N. Mokhov, G. V. Astakhov, and V. Dyakonov, Silicon carbide light-emitting diode as a prospective room temperature source for single photons, *Sci. Rep.* **3**, 1637 (2013).
- [90] A. Lohrmann, N. Iwamoto, Z. Bodrog, S. Castelletto, T. Ohshima, T. J. Karle, A. Gali, S. Praver, J. C. McCallum, and B. C. Johnson, Single-photon emitting diode in silicon carbide, *Nat. Commun.* **6**, 7783 (2015).
- [91] S.-i. Sato, T. Honda, T. Makino, Y. Hijikata, S.-Y. Lee, and T. Ohshima, Room Temperature Electrical Control of Single Photon Sources at 4H-SiC Surface, *ACS Photonics* **5**, 3159 (2018).

- [92] M. Widmann, M. Niethammer, T. Makino, T. Rendler, S. Lasse, T. Ohshima, J. U. Hassan, N. T. Son, S.-Y. Lee, and J. Wrachtrup, Bright single photon sources in lateral silicon carbide light emitting diodes, *Appl. Phys. Lett.* **112**, 231103 (2018).
- [93] P. V. Klimov, A. L. Falk, B. B. Buckley, and D. D. Awschalom, Electrically Driven Spin Resonance in Silicon Carbide Color Centers, *Phys. Rev. Lett.* **112**, 087601 (2014).
- [94] A. L. Falk, P. V. Klimov, B. B. Buckley, V. Ivady, I. A. Abrikosov, G. Calusine, W. F. Koehl, A. Gali, and D. D. Awschalom, Electrically and mechanically tunable electron spins in silicon carbide color centers, *Phys. Rev. Lett.* **112**, 187601 (2014).
- [95] M. Widmann, M. Niethammer, D. Y. Fedyanin, I. A. Khramtsov, T. Rendler, I. D. Booker, J. Ul Hassan, N. Morioka, Y. C. Chen, I. G. Ivanov, N. T. Son, T. Ohshima, M. Bockstedte, A. Gali, C. Bonato, S. Y. Lee, and J. Wrachtrup, Electrical Charge State Manipulation of Single Silicon Vacancies in a Silicon Carbide Quantum Optoelectronic Device, *Nano. Lett.* **19**, 7173 (2019).
- [96] S. J. Whiteley, G. Wolfowicz, C. P. Anderson, A. Bourassa, H. Ma, M. Ye, G. Koolstra, K. J. Satzinger, M. V. Holt, F. J. Heremans, A. N. Cleland, D. I. Schuster, G. Galli, and D. D. Awschalom, Spin–phonon interactions in silicon carbide addressed by Gaussian acoustics, *Nat. Phys.* **15**, 490 (2019).
- [97] A. V. Poshakinskiy and G. V. Astakhov, Optically detected spin-mechanical resonance in silicon carbide membranes, *Phys. Rev. B* **100**, 094104 (2019).
- [98] S. Castelletto, B. C. Johnson, C. Zachreson, D. Beke, I. Balogh, T. Ohshima, I. Aharonovich, and A. Gali, Room Temperature Quantum Emission from Cubic Silicon Carbide Nanoparticles, *ACS Nano* **8**, 7938 (2014).
- [99] A. Muzha, F. Fuchs, N. V. Tarakina, D. Simin, M. Trupke, V. A. Soltamov, E. N. Mokhov, P. G. Baranov, V. Dyakonov, A. Krueger, and G. V. Astakhov, Room-temperature near-infrared silicon carbide nanocrystalline emitters based on optically aligned spin defects, *Appl. Phys. Lett.* **105**, 243112 (2014).
- [100] A. Gali, T. Simon, and J. E. Lowther, Anab initiostudy of local vibration modes of the nitrogen-vacancy center in diamond, *New J. Phys.* **13**, 025016 (2011).

- [101] H. B. Banks, Ö. O. Soykal, R. L. Myers-Ward, D. K. Gaskill, T. L. Reinecke, and S. G. Carter, Resonant Optical Spin Initialization and Readout of Single Silicon Vacancies in 4H-SiC, *Phys. Rev. Appl.* **11**, 024013 (2019).
- [102] Ö. O. Soykal, P. Dev, and S. E. Economou, Silicon vacancy center in 4H-SiC: Electronic structure and spin-photon interfaces, *Phys. Rev. B* **93**, 081207(R) (2016).
- [103] V. Ivády, I. A. Abrikosov, and A. Gali, First principles calculation of spin-related quantities for point defect qubit research, *npj Comput. Mater.* **4**, 76 (2018).
- [104] M. Bockstedte, F. Schütz, T. Garratt, V. Ivády, and A. Gali, Ab initio description of highly correlated states in defects for realizing quantum bits, *npj Quantum Mater.* **3**, 31 (2018).
- [105] V. Ivády, J. Davidsson, N. T. Son, T. Ohshima, I. A. Abrikosov, and A. Gali, Identification of Si-vacancy related room-temperature qubits in 4H silicon carbide, *Phys. Rev. B* **96**, 161114(R) (2017).
- [106] N. T. Son, P. Carlsson, J. ul Hassan, E. Janzen, T. Umeda, J. Isoya, A. Gali, M. Bockstedte, N. Morishita, T. Ohshima, and H. Itoh, Divacancy in 4H-SiC, *Phys. Rev. Lett.* **96**, 055501 (2006).
- [107] J. R. Weber, W. F. Koehl, J. B. Varley, A. Janotti, B. B. Buckley, C. G. Van de Walle, and D. D. Awschalom, Quantum computing with defects, *Proc. Natl. Acad. Sci. U.S.A.* **107**, 8513 (2010).
- [108] W. Dong, M. W. Doherty, and S. E. Economou, Spin polarization through intersystem crossing in the silicon vacancy of silicon carbide, *Phys. Rev. B* **99**, 184102 (2019).
- [109] M. A. Reshchikov, A. A. Kvasov, M. F. Bishop, T. McMullen, A. Usikov, V. Soukhoveev, and V. A. Dmitriev, Tunable and abrupt thermal quenching of photoluminescence in high-resistivity Zn-doped GaN, *Phys. Rev. B* **84**, 075212 (2011).
- [110] C. Kittel, *Introduction to Solid State Physics* Wiley, New York (2004).
- [111] G. Kresse and J. Hafner, Ab initio molecular dynamics for liquid metals, *Phys. Rev. B* **47**, 558 (1993).
- [112] J. P. Perdew, A. Ruzsinszky, G. I. Csonka, O. A. Vydrov, G. E. Scuseria, L. A. Constantin, X. Zhou, and K. Burke, Restoring the density-gradient expansion for exchange in solids and surfaces, *Phys. Rev. Lett.* **100**, 136406 (2008).



- [113] F. Eriksson, E. Fransson, and P. Erhart, The hiphive package for the extraction of high-order force constants by machine learning *Adv. Theory Simul.* **2**, 1800184 (2019).
- [114] A. Togo and I. Tanaka, First principles phonon calculations in materials science, *Scr. Mater.* **108**, 1 (2015).
- [115] A. V. Krukau, O. A. Vydrov, A. F. Izmaylov, and G. E. Scuseria, Influence of the exchange screening parameter on the performance of screened hybrid functionals, *J. Chem. Phys.* **125**, 224106 (2006).
- [116] P. Deák, B. Aradi, T. Frauenheim, E. Janzén, and A. Gali, Accurate defect levels obtained from the HSE06 range-separated hybrid functional, *Phys. Rev. B* **81**, 153203 (2010).
- [117] A. A. Lebedev, Deep level centers in silicon carbide: A review, *Semiconductors* **33**, 107 (1999).
- [118] J. J. Markham, Interaction of Normal Modes with Electron Traps, *Rev. Mod. Phys.* **31**, 956 (1959).
- [119] T. Miyakawa and D. L. Dexter, Phonon Sidebands, Multiphonon Relaxation of Excited States, and Phonon-Assisted Energy Transfer between Ions in Solids, *Phys. Rev. B* **1**, 2961 (1970).
- [120] R. Nagy, M. Widmann, M. Niethammer, D. B. R. Dasari, I. Gerhardt, Ö. O. Soykal, M. Radulaski, T. Ohshima, J. Vučković, N. T. Son, I. G. Ivanov, S. E. Economou, C. Bonato, S.-Y. Lee, and J. Wrachtrup, Quantum Properties of Dichroic Silicon Vacancies in Silicon Carbide, *Phys. Rev. Appl.* **9**, 034022 (2018).
- [121] D. M. Lukin, C. Dory, M. A. Guidry, K. Y. Yang, S. D. Mishra, R. Trivedi, M. Radulaski, S. Sun, D. Vercruyse, G. H. Ahn, and J. Vučković, 4H-silicon-carbide-on-insulator for integrated quantum and nonlinear photonics, *Nat. Photon.* **14**, 330 (2019).
- [122] S. A. Zargaleh, B. Eble, S. Hameau, J. L. Cantin, L. Legrand, M. Bernard, F. Margailan, J. S. Lauret, J. F. Roch, H. J. von Bardeleben, E. Rauls, U. Gerstmann, and F. Treussart, Evidence for near-infrared photoluminescence of nitrogen vacancy centers in 4H-SiC, *Phys. Rev. B* **94**, 060102(R) (2016).

- [123] W. F. Koehl, B. Diler, S. J. Whiteley, A. Bourassa, N. T. Son, E. Janzén, and D. D. Awschalom, Resonant optical spectroscopy and coherent control of Cr<sup>4+</sup> spin ensembles in SiC and GaN, *Phys. Rev. B* **95**, 035207 (2017).
- [124] T. M. Babinec, B. J. Hausmann, M. Khan, Y. Zhang, J. R. Maze, P. R. Hemmer, and M. Loncar, A diamond nanowire single-photon source, *Nat. Nanotechnol* **5**, 195 (2010).
- [125] M. Leifgen, T. Schröder, F. Gädeke, R. Riemann, V. Métillon, E. Neu, C. Hepp, C. Arend, C. Becher, K. Lauritsen, and O. Benson, Evaluation of nitrogen- and silicon-vacancy defect centres as single photon sources in quantum key distribution, *New J. Phys.* **16**, 023021 (2014).
- [126] G. Calusine, A. Politi, and D. D. Awschalom, Silicon carbide photonic crystal cavities with integrated color centers, *Appl. Phys. Lett.* **105**, 011123 (2014).
- [127] J. Y. Lee, X. Lu, and Q. Lin, High-Q silicon carbide photonic-crystal cavities, *Appl. Phys. Lett.* **106**, 041106 (2015).
- [128] P. Kehayias, M. W. Doherty, D. English, R. Fischer, A. Jarmola, K. Jensen, N. Leefer, P. Hemmer, N. B. Manson, and D. Budker, Infrared absorption band and vibronic structure of the nitrogen-vacancy center in diamond, *Phys. Rev. B* **88**, 165202 (2013).
- [129] D. P. L. Aude Craik, P. Kehayias, A. S. Greenspon, X. Zhang, M. J. Turner, J. M. Schloss, E. Bauch, C. A. Hart, E. L. Hu, and R. L. Walsworth, Microwave-Assisted Spectroscopy Technique for Studying Charge State in Nitrogen-Vacancy Ensembles in Diamond, *Phys. Rev. Appl.* **14**, 014009 (2020).
- [130] V. A. Soltamov, B. O. Tolmachev, I. V. Il'in, G. V. Astakhov, V. V. Dyakonov, A. A. Soltamova, and P. G. Baranov, Point Defects in Silicon Carbide as a Promising Basis for Spectroscopy of Single Defects with Controllable Quantum States at Room Temperature, *Phys. Solid State* **57**, 891 (2015).
- [131] D. D. Awschalom, R. Hanson, J. Wrachtrup, and B. B. Zhou, Quantum technologies with optically interfaced solid-state spins, *Nature Photonics* **12**, 516 (2018).

# Acknowledgements

Firstly, I would like to thank Prof. Manfred Helm and Dr. Shengqiang Zhou for giving me this opportunity to learn in Dresden and have four happy years here. Their decision changed my life and made me a better person.

Then, I would like to show the greatest appreciation to my supervisor Dr. Georgy A. Astakhov. As my supervisor and group leader, he tried his best to help me. I am pretty sure that I cannot finish my project without his help. Thank you, Georgy.

I am very grateful to Dr. Yonder Berencén. I appreciate what he taught me in these four years.

Thank Mr. Michael Hollenbach for the help in my work. He is a very good colleague and a friend.

Thank Dr. Slawomir Prucnal and Dr. Rebohle Lars for the help in the PL experiment.

Thank Ms. Ilona Skorupa for the help in the annealing experiment.

Thank Mr. Thomas Schumann for the help in the annealing experiment and the setup.

Thank Dr. Rysard Narkovic for the help in the home-built setup.

Thank Dr. Arkady Krashennikov and Dr. Arsalan P. Hashemi for the help in the theoretical calculation.

Thank all colleagues in IBC for the help in the defects fabrication.

Thank all my colleagues in FWIM and friends in Dresden. Especially, Dr. Ye Yuan, Dr. Chi Xu, Dr. Mao Wang, Dr. Lei Cao, Dr. Changan Wang, Ms. Yufang Xie, Mr. Zichao Li, thanks for your help in my work and in my life.

Thank all my ex-colleagues in Shandong University, particularly Prof. Feng Chen and Prof. Yang Tan.

Finally, I should say thank to my family and to Ms. Zhen Liu. Thanks for your love.

Thank you, Dresden! Thank you, Germany!

## Publication list

1. **Z. Shang**, Y. Berencén, M. Hollenbach, S. Zhou, H. Kraus, T. Ohshima and G.V. Astakhov, Microwave assisted spectroscopy of vacancy related spin centers in hexagonal SiC, *Phys. Rev. Appl*, **15**, 034059 (2021)
2. **Z. Shang**, A. Hashemi, Y. Berencén, H.-P. Komsa, P. Erhart, S. Zhou, M. Helm, A. V. Krashennnikov, and G. V. Astakhov, Local vibrational modes of Si vacancy spin qubits in SiC, *Phys. Rev. B* **101**, 144109 (2020).
3. C. Kasper, D. Klenkert, **Z. Shang**, D. Simin, A. Sperlich, H. Kraus, C. Schneider, S. Zhou, M. Trupke, W. Kada, T. Ohshima, V. Dyakonov, and G. V. Astakhov, Influence of Irradiation on Defect Spin Coherence in Silicon Carbide, *Phys. Rev. Appl* **13**, 044054 (2020).
4. I. D. Brev, **Z. Shang**, A. V. Poshakinskiy, H. Singh, Y. Berencén, M. Hollenbach, S. S. Nagalyuk, E. N. Mokhov, R. A. Babunts, P. G. Baranov, D. Suter, M. Helm, S. A. Tarasenko, G. V. Astakhov, and A. N. Anisimov, Inverted fine structure of a 6H-SiC qubit enabling robust spin-photon interface, arXiv:2107.06989.

# Curriculum Vitae

## Personal data

- Name: Zhen Shang,
- Birthday: 02.07.1990
- Birth place: Shandong, China

## Educational Experience

- 2017/11- now, Ph.D., Institute of Ion Beam Physics and Materials Research, Helmholtz-Zentrum Dresden-Rossendorf & Technische Universität Dresden, Germany.
- 2014/09-2017/06, M.S., School of physics, Shandong University, China.
- 2010/09-2014/06, B.S., School of physics, Shandong University, China

# Erklärung

Hiermit versichere ich, dass ich die vorliegende Arbeit ohne unzulässige Hilfe Dritter und ohne Benutzung anderer als der angegebenen Hilfsmittel angefertigt habe; die aus fremden Quellen direkt oder indirekt übernommenen Gedanken sind als solche kenntlich gemacht. Die Arbeit wurde bisher weder im Inland noch im Ausland in gleicher oder ähnlicher Form einer anderen Prüfungsbehörde vorgelegt.

Diese Dissertation wurde angefertigt im

Helmholtz-Zentrum Dresden-Rossendorf  
Institut für Ionenstrahlphysik und Materialforschung  
Bautzner Landstr. 400  
01328 Dresden

Die wissenschaftliche Betreuung der Arbeit erfolgte durch Prof. Dr. Manfred Helm.

Ich versichere, an keiner Institution, auch nicht im Ausland, jemals den Antrag auf Eröffnung eines Promotionsverfahrens gestellt zu haben.

Ich erkenne die Promotionsordnung der Fakultät Mathematik und Naturwissenschaften der Technischen Universität Dresden an

Zhen Shang

06.07.2021, Dresden